Bubbly Shock Propagation as a Cause of Sheet to Cloud Transition of Partial Cavitation and Stationary Cavitation Bubbles Forming on a Delta Wing Vortex

by
Harish Ganesh

A dissertation submitted in partial fulfillment
of the requirements for the degree of
Doctor of Philosophy
(Mechanical Engineering)
in The University of Michigan
2015

Doctoral Committee:

Professor Steven L. Ceccio (Chair)
Professor David R. Dowling
Assistant Professor Eric Johnsen
Professor Marc Perlin

Dedicated to my parents

Acknowledgements

I would like thank my advisor, Prof. Steve Ceccio for all his guidance and support throughout my graduate studies. The amount of knowledge gained from him in the field of fluid mechanics, work ethic, and people skills is immense. I would also like to thank my committee members, Prof. Marc Perlin for agreeing to be in my committee, Prof. Eric Johnsen and Prof. David Dowling for both being in my committee and for their kindness in encouraging me during my walk-in consulting.

This work would not have been possible without the support of our sponsor, Office of Naval Research. I would like to thank them and the program manager Dr. Ki-Han Kim.

In addition, I would like to thank Dr. Simo Makiharju for all his guidance and help throughout my Ph.D. My colleagues Joel Hartenberger, Dr. Andrew Wiggins, Jimmy Gose, Inho Lee and Seongjin Yoon deserve special mention for all the collaborations and sharing of resources. I would also like to thank Andre Pinheiro, Dr. Bu-Guen Paik and Joost Schot for all the contributions they made right from the inception to the culmination of the delta wing cavitation experiment, and Dr. Natasha Chang for her guidance during tip vortex cavitation experiment.

There were numerous visiting students: Uday Meduri (Tip vortex cavitation), Quentin Laurent & Vianney Flepp (Preliminary wedge studies at MHL), Alex Kerrien & Pierre-Alexandre Dambrine (Flow separation studies), Cedric Le Juene & Alexis Mallegol (Free-streamline solution), Stephanie Saade (Delta wing vortex studies) and Tiezhi Sun (Shock wave post processing) who

collaborated with me at various stages of my dissertation. I would like to thank them all for their support and contribution towards this thesis.

I would like to thank Kent Pruss for his time. There have been numerous occasions when Kent made sure I had what I needed to work over the weekend. I would also like to thank Bill Kirkpatrick, Marv Casey for their assistance in the machine shop. Dave Parsons deserves a special mention for all the expertise he provided during my time at MHL. I would also like to thank Melissa McGeorge and Sallie Kne for their time.

My graduate school experience would not have been complete without friends. In that regard I am thankful to Terry Shyu, Adaleena Mookerjee, Marc Henry de Frahan, Pooya Movahed, Samuel Pellone, Brian Worthman, Shima Hossein Abadi, Brian Elbing, Natasha Chang, Jane Kim, Brandon Patterson, Prasnna Amur Varadharajan, and Kaustubh Nyalkalkar, for entertaining my conversations about various topics. I would also like to thank all my friends, fellow dancers, and board members from Michigan Argentine Tango Club for all the lovely memories and great times.

Finally, I thank my parents for being very supportive of all my decisions throughout my life. I always cherish the freedom that they give me to pursue my goals and aspirations. I would also like to thank my grandparents who played a significant role in moulding my curious nature at early stages of my life.

Table of Contents

List of Figures

List of Tables

Abstract

a) Bubbly Shock Propagation as a Cause of Sheet to Cloud Transition of Partial Cavitation.

Cavitation dynamics on a wedge is studied using time resolved X-ray densitometry to identify different regimes of cavitation dynamics and mechanisms. The study focuses on the mechanisms of transition from partial stable cavities to periodic shedding of vapour clouds. In addition to the experiments, free-streamline solution of the cavity shape is obtained for different cavitation numbers to compare the closeness of observed physics in experiments to simplified assumptions used in analytical models. From the experiments, presence of re-entrant flow and propagating bubbly shock fronts are identified as mechanisms that are responsible for the shedding of vapour clouds for transitory cavities. Bubbly shock induced shedding was found to be the dominant mechanism of shedding for periodic cavities. Upon further investigation of mechanism dynamics by pressure measurements the observed condensation shock dynamics is shown to be broadly consistent with simplified analysis based on one-dimensional conservation laws. Cavity growth rate is identified as the critical parameter responsible for the generation of shock waves, and hence the observed mechanism. The role of adverse pressure gradient in dictating both the re-entrant flow and the cavity growth process, and hence the shock production mechanism is emphasised in the observed dynamics of shedding

b) Stationary Cavitation Bubbles Incepting on a Delta Wing Vortex

Vortex cavitation forming in the leading-edge vortices of a delta wing was examined to determine how the individual cavitation bubbles incepted, grew, interacted with the underlying vortical flow, and produced acoustic tones. The non-cavitating vortical flow over the delta wing was chosen to be similar to those previously reported in the literature. It was found that vortex breakdown was unaffected by the presence of incipient and developed vortex cavitation bubbles in the vortex core. While some cavitation bubbles incepted, grew, and collapsed relatively quickly, others reached an equilibrium position wherein the bubble tip was stationary in the laboratory frame at a particular location along the vortex axis. For a given attack angle, equilibrium location moved upstream with a reduction in free stream cavitation number. It is shown that the existence of these stationary vortex bubbles is possible when there is a balance between the axial growth of the bubble along the vortex axis and the opposite motion of the axial jetting flow in the vortex core, and only a single equilibrium position is possible along the axially evolving vortex for a given free stream cavitation number. These transient and stationary vortex bubbles emit significant cavitation noise upon inception, growth, and collapse. The spectral content of the noise produced was expected to be related to the interaction of the bubble with the surrounding vortical flow in a manner similar to that reported in previous studies, where sustained tones were similar to the underlying vortex frequency. However, in the present study, the dominant frequency and higher harmonics of the tones occur at a higher frequency than that of the underlying vortex. Hence, it is likely that the highly elongated stationary bubbles have higher-order volume oscillations compared to the two-dimensional radial mode of the vortex cores of vortex cavitation bubbles with much smaller diameter-to-length ratios.

CHAPTER 1

Introduction

This thesis concerns two different studies on hydrodynamic cavitation. The first is a study on partial cavitation in a backward facing wedge and the next is a study on cavitation in the leading edge vortices of a delta wing. Both these studies have important applications in the design on marine propellers. Chapters 2-9 will focus on the partial cavitation on a wedge and Chapters 10-13 will focus on the cavitation study on delta wings.

1.1 Bubbly Shock Propagation as a Cause of Sheet to Cloud Transition of Partial Cavitation

Cavitation can occur in separated regions of flow behind objects resulting in partially filled vapour cavities. Once formed, partial cavities are generally stable, but can experience auto oscillations of cavity length resulting in shedding of vapour clouds, termed cloud cavitation, carrying the vapour filled mixture that originally formed the cavity. Cloud cavitation and its onset are detrimental, and is one of the principal agents of cavitation induced surface erosion.

In the present study, cavitation occurring on the separated flow region behind the wedge is studied with the aid of time resolved X-ray densitometry based void fraction flow field measurements synchronized with dynamic pressure transducers. The wedge geometry was chosen because of the resemblance of an internal flow in a channel with a backward

facing wedge to that of flow through turbomachinery blade passages. Using time resolved X-ray densitometry and high speed cinematography, different regimes of cavitation on this wedge are carefully studied. The experimentally observed cavity behavior is also compared with theoretically predicted cavity shapes to estimate the closeness of actual physics to that represented by the models. From the measurements, dominant mechanisms that are responsible for shedding are identified and the role of flow parameters responsible for the existence of the mechanisms is also understood.

1.1.1 Contributions of wedge cavitation study

Time resolved 2-D X-ray densitometry measurements of cavitating flow over a wedge has not been reported before. The present study also used a simple analytical model to estimate the relative importance of physical processes, such as vapor production, cavity growth rate, in different regimes of cavitation by comparison with experiments. One of the most important contributions of the present study is the identification of a propagating discontinuity, similar to a bubbly shock wave as a key mechanism of shedding, in addition to the presence of a re-entrant flow. A wedge geometry with its relative simplicity can be used a bench mark for CFD code validations. In that regard, the data from the present study can be used for improving CFD algorithms.

1.1.2 Wedge cavitation study roadmap

Chapter 2 introduces the problem with an overview of the underlying physics and prior studies in the topic. Chapter 3 describes the experimental setup, flow conditions and the geometry chosen. Chapter 4 deals with the mathematical formulation used to predict the cavity shape on the wedge. Chapter 5 discusses the general experimental cavity behaviour with relation to inception,

transition and shedding and compares the observations with the predicted analytical solution. Cavity dynamics are presented in Chapter 6. Two mechanisms of shedding, re-entrant flow and condensation shocks, observed in the experiments are presented in Chapter 7. Chapter 8 explores the conditions needed for the existence of condensation shock waves and compares the observations from the present study to the necessary conditions. Chapter 8 also presents an analysis that illustrates the reason for the occurrence of condensation shocks, relationship between the shocking, shedding and geometry. Chapter 9 presents the conclusions of this part of the study.

1.2 Stationary Cavitation Bubbles Incepting on a Delta Wing Vortex

Vortex cavitation is usually the first observed type of cavitation in marine propellers and other lifting surfaces. Vortex cavitation is also a primary source of performance breakdown of ship propellers and vortex cavitation noise is of concern for stealth vehicles like submarines. Vortex cavitation on tip vortices shed from lifting surfaces has been studied extensively, from the perspective of cavitation inception, bubble dynamics, and acoustics.

The relationship between the single phase vortex properties and the observed bubble size is yet to be completely understood, from the context of what sets the dimensions of the bubble. The role of the nuclei content and the inception location also plays an important role in the acoustics of the vortex cavitation. Thus, there are many questions about the interaction of the vortex and the bubble; mainly, the scaling of the observed bubble dynamics and acoustics to the vortex properties. A delta wing vortex with rapidly varying vortex properties and experiencing vortex breakdown, unlike a rolled up tip vortex, provides unique conditions to study vortex cavitation. A delta wing vortex provides conditions that can be used to study the role of specific vortex

properties on bubble dynamics and acoustics.

1.2.1 Contributions of delta wing study

Interaction of vortex cavitation bubbles with a delta wing vortex has not been reported before. Delta wing leading edge vortex with its rapidly varying vortex properties provides unique conditions for studying bubble vortex interaction, cavitation bubble dynamics, and bubble acoustics. In the present study, presence of different types of bubbles and their relations to underlying delta wing vortcial flow are presented. The relationship between observed bubble dynamics, acoustics, and vertical flow properties are also presented. This work is published in Physics of Fluids. For further information please refer to,

Ganesh, H., Schot, J, & Ceccio, S. L, "Stationary cavitation bubbles in delta wing vortices ," Physics of Fluids., 16, 4, 2411-2418 (2014).

1.2.2 Delta wing study road map

Chapter 10 provides a background on vortex cavitation and delta wing vortical flow. Chapter 11 deals with the experimental setup. Chapter 12 presents the observed cavitation events and bubble acoustics are presented in Chapter 13. The conclusions of this topic are presented in Chapter 14.

CHAPTER 2

Sheet and Cloud Cavitation

Hydrodynamic cavitation is a phenomenon characterised by phase change from liquid to vapour at nearly constant temperatures in low pressure regions of a flow field. Partial cavitation occurs when the low pressure regions produced by separated shear flows are filled with vapour, forming a cavity. Flow scenarios exhibiting partial cavitation are separated shear layer on the suction side of lifting surfaces at high attack angles, blades of turbo machinery, inducers of cryogenic rocket motors, Venturi of a diesel fuel injector, *etc*. Figure 2.1 shows different types of cavities that can form on a NACA009 hydrofoil. Once formed, partial cavities are generally stable, but can experience auto oscillations of cavity volume when the cavity length exceeds a particular geometry specific value. These auto oscillations of length are also characterised by the shedding of vapour clouds, termed as cloud cavitation, carrying the vapour filled mixture that originally formed the cavity. The cavity volume oscillations can be intermittent or periodic, and have an adverse effect on the performance of devices such as propellers, diesel injectors, lifting surfaces, *etc*.

2.1 Regimes of Partial Cavitation

Partial cavities forming on certain geometries have a specific behaviour exhibiting different types of cavitation depending upon the prevalent conditions. One of the parameters that dictates

this behaviour is the free stream cavitation number, with the other being geometric parameters that produce the underlying pressure field. One such geometric parameter is the attack angle, and partial cavities forming on hydrofoils are strongly dependent on the attack angle for a given free stream pressure. Figure 2.2 shows different types of cavitation on a plano-circular hydrofoil at different attack angles, α and cavitation number σ_v.

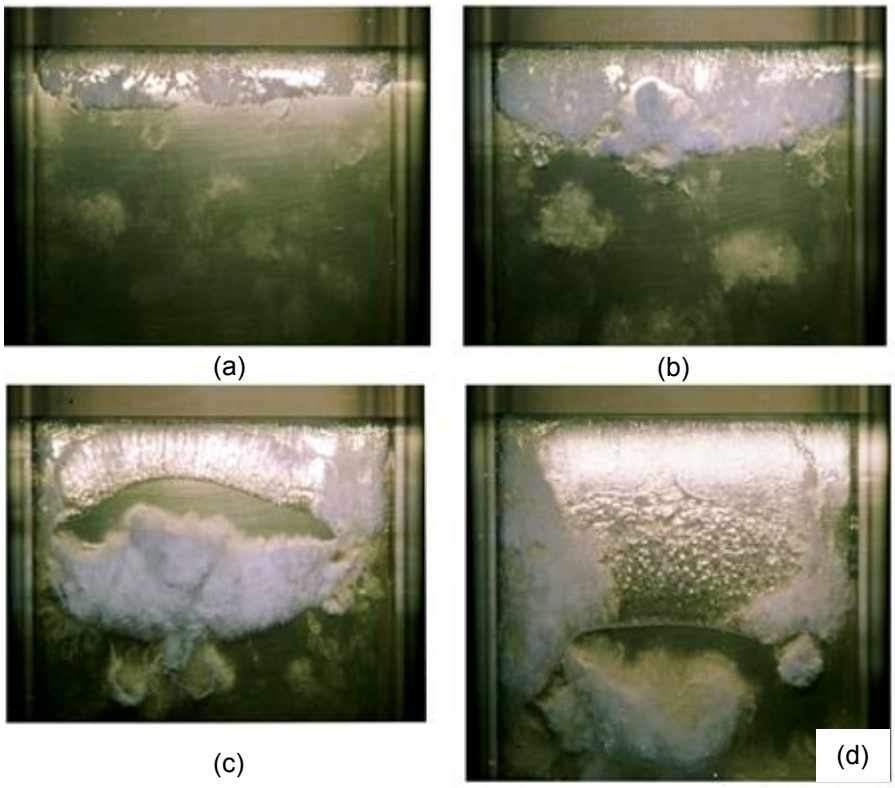

Figure 2.1: Different types of cavitation on an elliptic hydrofoil (a) Partial stable cavity, (b-d) shedding cavities of different lengths. (Source: Laberteux and Ceccio, 2001a)

From Figure 2.2 it can be seen that at certain conditions the cavity is both smaller in length in comparison with the chord, and stable. Starting with such a cavity, reduction in cavitation number for a given attack angle produces different types of cavities, with some exhibiting

periodic shedding of vapour clouds.

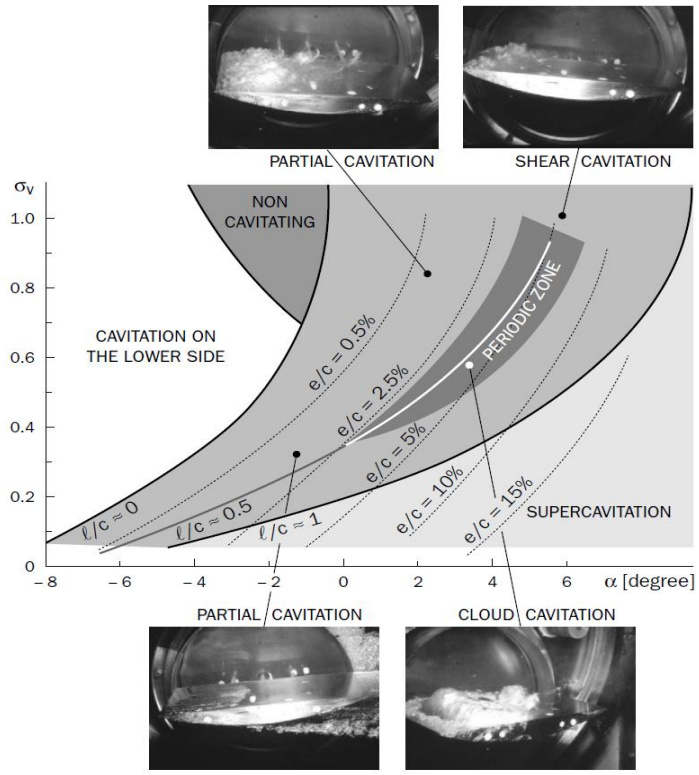

Figure 2.2: Cavitation patterns on a plano circular hydrofoil at free stream speed of 10 m/s. 'l' denotes the cavity length, 'c' denotes the chord length of 200 mm, and 'e' denotes the maximum cavity thickness. (Source: Fundamentals of Cavitation, Springer, 2001)

With a further reduction of cavitation number, the cavity length grows to be larger than the chord length producing a "super cavity". The occurrence of periodic shedding of vapour clouds, and its mechanism has been studied extensively. Flow features or attributes that cause the shedding, and their relations to governing equations of motion has been well explored. Considerable effort has gone in understanding the mechanism of periodic shedding in particular, and most of the studies attribute the presence of a re-entrant liquid flow responsible for the periodic shedding. Relevant studies are reviewed in the upcoming sections.

2.2 Re-entrant Flow in Partial Cavities

One of the earliest studies on the observation and dynamics of cloud cavitation was done by Knapp (1955). The study identified different phases of the unsteady dynamics, and the presence of a liquid re-entrant flow. Since then, many studies have been performed to verify the existence, development, the role of liquid re-entrant flow on cavitation dynamics. A re-entrant liquid flow constitutes a liquid jet flow into the cavity, originating from the cavity closure region. The presence of a stagnation point aft of the cavity closure region facilitates the presence of this liquid re-entrant flow. A schematic of the re-entrant flow is shown in Figure 2.3.

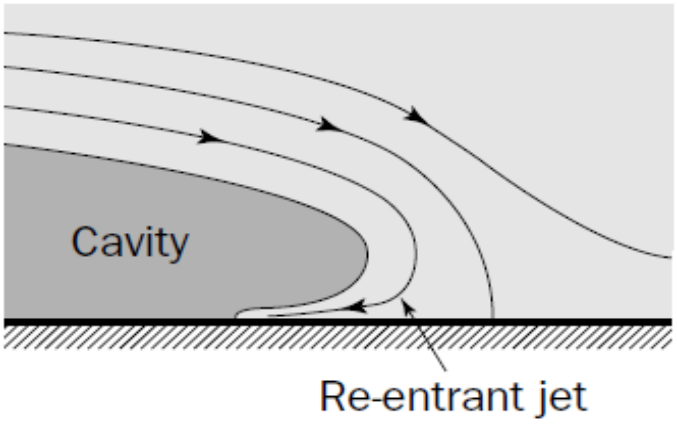

Figure 2.3: Schematic of flow in the vicinity of cavity closure illustrating re-entrant flow (Source: Fundamentals of Cavitation, Springer, 2001).

Furness and Hutton (1975), using a potential flow based numerical method, computed the structure of the re-entrant flow on a convergent-divergent nozzle until it intersected the cavity interface. They found the results to be in reasonable comparison with experiments. Lush and Skipp (1986) also attributed the occurrence of periodic shedding to re-entrant jets. Visualisation of re-entrant jets on cavitating flows has also been reported Le *et al.* (1993) using dye injection

(plano-convex hydrofoil) and De Lange (1996) using a transparent 2-D hydrofoil model. The presence of the re-entrant jet, and its role involved in the shedding of 2-D hydrofoil was verified in a study by Kawanami (1997). By placing an obstacle in the path of the re-entrant jet generated on a hydrofoil, they found that auto oscillations vanished, suggesting its prominent role.

Partial cavitation studies on objects with span wise geometric variations, such as hydrofoils with sweep have also been studied Crimi (1970), Bark (1985, 1986), Ihara *et al.* (1989), and De Lange (1996). Unlike a 2-D cavity which has the cavity closure line perpendicular to the flow direction, the closure line for 3-D cavities can be oriented in a direction that is geometry dependent. This would result in the re-entrant jet having a different orientation, and different dynamics. Laberteaux and Ceccio (2001b) found that 3-D geometry can sustain stable cavities with re-entrant flow. They found that re-entrant flow was directed away from the cavity, making it stable.

However, this does not mean that 3-D geometries cannot experience periodic shedding. Foeth *et al*. (2008) made an informative study of partial cavitation dynamics on a twisted foil. They found that periodic shedding was indeed observed, and that re-entrant jet had a component along the span wise direction, pinching off vapour clouds. These studies on different geometries suggest that the existence of a re-entrant is not sufficient for periodic shedding of clouds.

2.3 Re-entrant Flow Development

The conditions necessary for the development of a re-entrant jet, and subsequent periodic shedding has been explored in detail for canonical 2-D geometries. Calleanare *et al.* (2001), in a seminal study, explored cavitation dynamics on 2-D geometry. They mapped different regimes of flow with no shedding, periodic re-entrant jet observation with no shedding, and re-entrant jet

induced periodic shedding. They found the importance of the role of the adverse pressure on the development of the re-entrant that resulted in periodic shedding. Gopalan and Katz (2000) in their study on cavitation in a nozzle found that re-entrant jet developed when the cavity closure was in the region of adverse pressure. Laberteux and Ceccio (2001a) also found that partial cavitation on wedges did not experience re-entrant flow hence no shedding, but rather a turbulent frothy wake. They suggested the importance of the flow in the closure of the cavity and its role in dictating the phase transfer and the development of the re-entrant jet. Le *et al.* (1993) measured the pressure distribution in a partial cavity on a plano-convex foil, at different attack angle and cavitation number combinations, for constant cavity lengths. They found that the pressure distribution for cavities with re-entrant flow and shedding was different from non-shedding open cavities, with the maximum pressure values having much lower values.

2.4 Cloud Shedding Dynamics

Thus there have been many studies that have reported the existence of a re-entrant jet and its relation to periodic shedding. Since shedding is a periodic process, the frequency of shedding is related to underlying cavitating flow field and the separated flow field in an adverse pressure gradient. For a given cavity length, the advection time scale and vapor generation processes involved need to be suitable to cause periodic shedding. The non-dimensional number that characterizes flow periodicity is the Strouhal number *St,* as defined in Equation 2.1, where L_c is the cavity length, F is the frequency of shedding, U a characteristic velocity.

$$St = \frac{FL_c}{U} \tag{2.1}$$

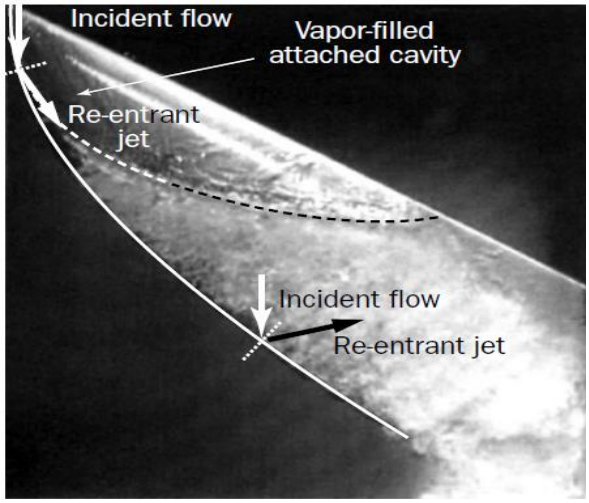

Figure 2.4: Cavitation on a three-dimensional hydrofoil with 30 degree sweep and attack angle of 2 degrees for a flow velocity of 10.1 m/s and a cavitation number of 0.7 (Source: Fundamentals of Cavitation, Springer, 2001))

In most of studies, for the cases of periodic shedding, *St* is found to be in the range of 0.25-0.35.

2.5 Flow Field Measurement Studies

Diagnosis of the cavitating flow field has also been done to understand the relationship of the measurements to the observed dynamics. Kubato *et al*. (1989) performed comprehensive unsteady measurements of the velocity field of a cavitating flow over a hydrofoil using conditionally sampled LDV. They found the convection velocity of the cloud to be much lower than the free stream speed. Reisman and Brennen (1998) measured the pressure signals during the shedding cycle, and correlated them with the observed dynamics of the vapour cloud. They suggested the presence of shock waves as cloud collapse mechanism, which causes rapid change in the void fraction distribution. Kawanami *et al*. (2002) used laser holography to study the structure of a cloud shed from a hydrofoil, and estimated the bubble size distribution. Measurements of the re-entrant flow underneath the cavity using electrical impedance probes was done by Pham *et al.* (1998), and George *et al.* (2000). Callenaene *et al*.(2000) measured the

thickness of the re-entrant jet using acoustic probes, and found shedding to be dependent on the jet thickness, with thicker re-entrant jets resulting in shedding. Foeth *et al.* (2006) used time resolved particle image velocimetry, and flow visualization techniques to estimate the interfacial velocity of a cavitation on a twisted hydrofoil. They found that the velocity at the interface of the cavity was very close to that estimated using a simple streamline model.

2.6 Void Fraction Flow Fields of Partial Cavities

Measurements of the void fraction distribution on a Venturi type geometry was performed by Stutz and Reboud (1997a and 1997b). Using optical probes, they measured conditionally averaged void fraction and the liquid phase flow velocity of cloud shedding. They also observed the presence of reversed liquid flow, and reported a maximum measured void fraction of 0.21. On a different geometry (1997b), they performed detailed flow measurements using LDV to characterise the outer liquid flow, and optical probes to measure the void fraction distribution and liquid phase velocity in an attached sheet cavity. They found the presence of a re-entrant flow that results in a stable cavity and used simple mass balance relations to estimate the vapour flow co-efficient. They reported maximum void fraction of 0.8 near in fore part of the cavity.

Stutz and Legoupil (2003) used non-ionizing radiation to non-intrusively measure void fraction in a geometry similar to Stutz (1997 a). The setup consisted of a row of 24 detectors that can acquire void fraction profiles along a line at a rate of 1000 samples per second. The measurements were compared with optical probes, and it was found that the maximum void fraction for the case of periodic shedding was about 0.25. Delgosha *et al.* (2007) used the same diagnostic setup to measure void fraction profiles on a plano convex foil. They reported a maximum averaged void fraction values of close to 0.6 with instantaneous values exceeding

0.85.

2.7 Speed of Sound in Low Void Fraction Flows

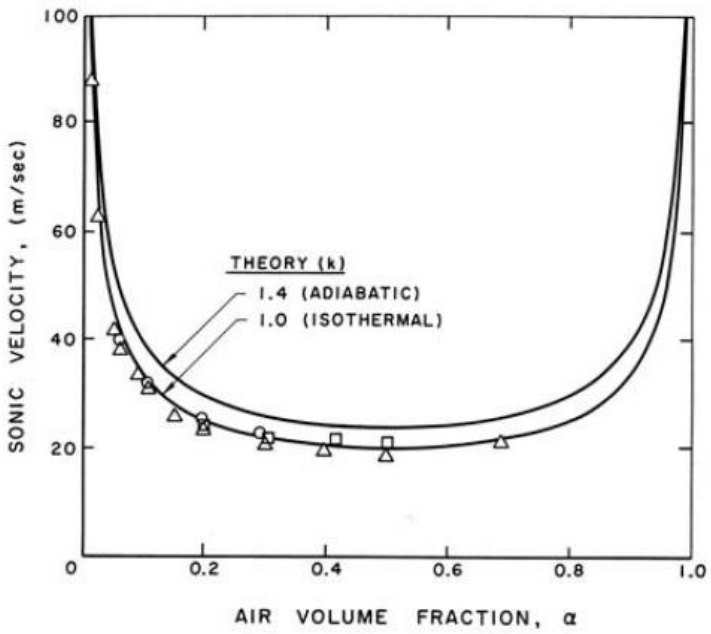

Figure 2.5: The sonic velocity in a bubbly air/water mixture at atmospheric pressure for ratio of specific heats k = 1.0 and 1.4. Experimental data presented is from Karplus (1958) and Gouse and Brown (1964) for frequencies of 1 kHz (○), 0.5 kHz (□), and extrapolated to zero frequency(Δ).(Source: Fundamentals of Multiphase flow, Brennan)

Measured values of void fraction by Stutz and Legoupil (2003) and Delgosha *et al.* (2007) suggest that the cavity is not very dense under certain conditions. This means that the local speed of sound in such scenarios can be very small, resulting in high local Mach numbers. Low values of speed of sound impose another time scale in the flow physics that could have an effect on the dynamics of the cavity. A discussion of variation of speed of sound with void fraction can be found it Brennan (2003). Figure 2.5 shows the variation of speed of sound with void fraction, α .

Low values of speed of sound result in smaller propagation speed of disturbances than in liquids.

This could potentially lead to the presence of shock waves that exist to achieve relevant flow conditions needed at the end of the cavity. However, so far, there have been no reports on the existence of any propagating discontinuity such as bubbly shock waves as mechanism of cloud shedding. This could be partly due to the unavailability of entire field measurements that can facilitate the identification of propagating discontinuities in void fraction flow fields.

2.8 Present Study

Understanding of the mechanism of transition from sheet to cloud cavitation requires estimation of length and time scales of different processes that contribute to shedding. Information regarding the relationship between vapour generation rates and other time scales of the flow can provide deeper insights into the mechanism of shedding. Makijarju *et al.* (2013) recently developed a X-ray densitometry system that measure void fraction flow fields of gas liquid flows. The X-ray system is capable of performing time resolved two dimensional void fraction flow fields of gas liquid flows. Even though such a device gives a line averaged measurement of void fraction flow filed, the scope of such a measurement device for cloud cavitation studies is immense, since all the measurements using the setup mentioned in Stutz and Legoupil (2003) and Delgosha *et al.*(2007) has been along a line. The present study will systematically use the above mentioned system to study different regimes of cavitation on wedge geometry. The reason for choosing the wedge geometry is summarised below:

1. The flow resembles the flow through turbo-machinery blade passages.
2. The wedge has a well separated flow from the apex with minimal dependence on the incoming flow boundary layer properties.
3. Availability of measurements on similar geometries for comparisons and interpretation of

obtained results.

4. Simplicity of the geometry for numerical simulation.

The study aims to achieve the following goals:

1. Use time resolved X-ray densitometry and flow properties measurement to study cavitating flow over a backward facing step for a range of cavitation numbers.
2. Compare the general behaviour of the observations from experiments to simplified theoretical models based on free-streamline theory to estimate the importance of different flow physics at different regimes.
3. Identify different regimes of cavitation and the mechanisms that are involved in the transition from sheet to cloud cavitation.
4. Understand the relationship of the mechanism to underlying flow parameters such as cavitation number and inlet speed.

2.9 Roadmap

The first part of the thesis will be laid out in the following manner. The experimental setup is introduced in Chapter 3. The properties of the flow in the test section without the wedge, the velocity profile at the inlet and the entrance of the secondary contraction with and without the wedge is presented in Chapter 3. Chapter 4 deals with the free-streamline formulation of analytical solution of cavitating flow over the wedge. The general trend of experimentally observed cavitation dynamics, variation of cavity length with inlet cavitation number, is presented and compared with free-streamline results in Chapter 5. Chapter 6 contains the cavitation dynamics that was observed for the wedge at different speeds and cavitation numbers. Chapter 7 presents the two identified mechanisms of re-entrant flow and propagating

condensation shock waves and the identification of condensation shock waves as the dominant mechanisms. Chapter 8 focuses on the condensation shock mechanism and verifies if the observations from the experiments are consistent with the flow physics based on governing equations. The identification of cavity growth as the crucial process that determines the shock propagation is also presented in Chapter 8. The conclusions of the partial cavitation part of the study are presented in Chapter 9.

CHAPTER 3

Experimental Setup

3.1 Flow Loop

Experiments were carried out at the University of Michigan 9" Water Tunnel. The tunnel has a 6:1 round contraction leading into a test section with a diameter of 22 cm (9 inches). The test section then transitions to a square cross section that is 21 cm by 21 cm with chamfered corners. The flow velocity and the static pressure in the tunnel test section can be varied from 0 to 18 m/s and from near vacuum to 100 kPa gauge pressure. A de-aeration system enables the control of the dissolved air content. In the present experiments, the test section was further reduced in area to a conduit that had a 7.6 cm by 7.6 cm cross-section. This was done to reduce the baseline X-ray attenuation produced by the non-cavitating flow as discussed later in this Chapter. Figure 3.1 shows a section view schematic diagram of the wedge within the test section.

3.2 Wedge Geometry

The geometry chosen in the study was designed to have a separated region of flow conducive to sustain partial cavitation. This was achieved by using a wedge, with a contraction angle of 22.1 degrees. After reaching a height of 2.54 cm, the contraction abruptly changed to a diffuser,

thereby causing the flow to separate at the wedge apex. The presence of a diffuser angle of 8.1 degrees created an adverse pressure gradient in the separated region of the flow.

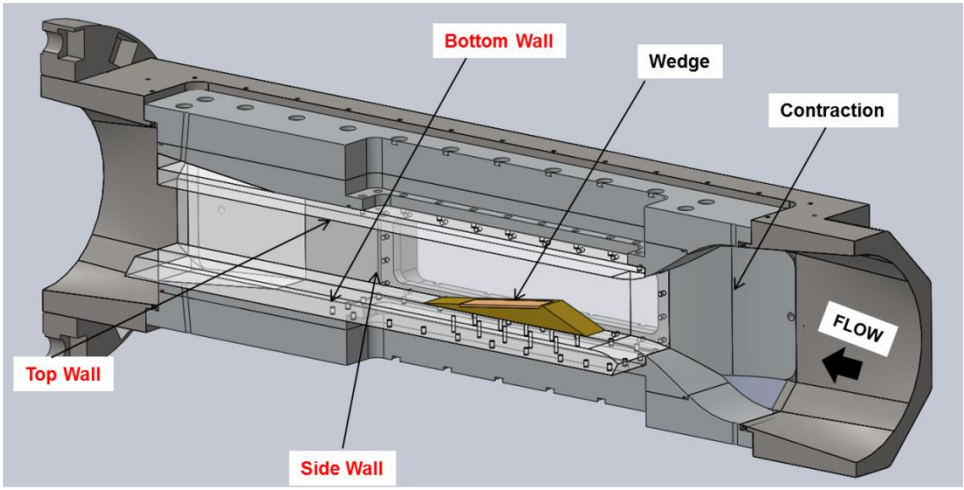

Figure 3.1: Schematic section view of the wedge in the reduced test section.

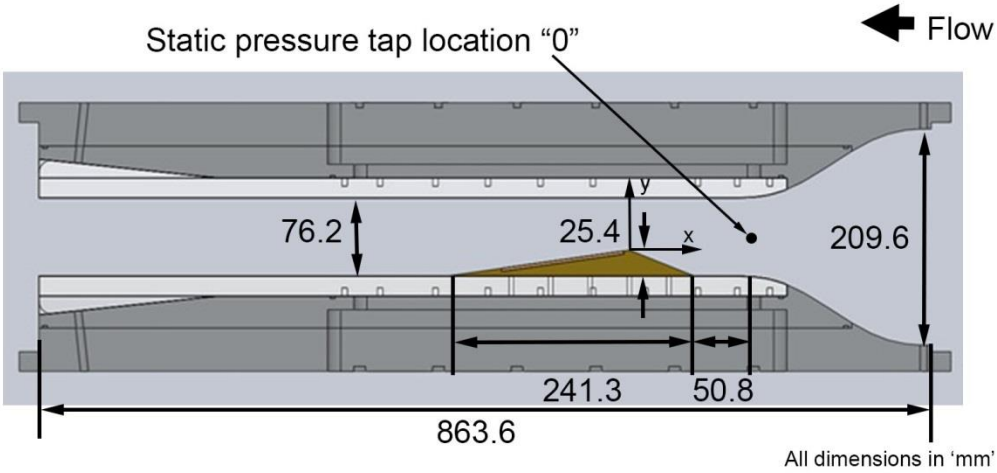

Figure 3.2: Sketch of the wedge and definition of the "0" location in the reduced test section.

The wedge was mounted in the reduced test section between the straight sidewalls of the tunnel, 76.2 mm in span, and optical access to the wedge was facilitated by acrylic test-section windows.

The wedge sides were fitted with o-rings on both the sides to ensure that no flow from the side interfered with the flow over the wedge. The leading edge of wedge was located at a distance of 50.8 mm from the end of the secondary contraction. Two wedge models were used to accomplish different goals of the study. One model was later fitted one flush mounted unsteady pressure transducer to measure the dynamic surface pressure variations. This model is described in Chapter 5. Another wedge model was specifically fabricated with surface pressure taps to measure averaged cavity pressure and apex pressure. This model also had slots for two unsteady pressure transducers. The description of the model can be found in Chapter 7. All the wedge models were marked with lines with an interval of 1 cm in both stream wise and span wise directions downstream of the wedge apex.

3.3 Inflow Conditions

The static pressure at the entrance to the secondary test section, designated as "0", in Figure 4.2, is measured using an Omega PX20-030A5V absolute pressure transducer. The pressure difference between the test section inlet and upstream of the primary contraction was measured using an Omega PX409030DWU10V differential pressure transducer. Based on the measurement of the differential pressure, and the area ratios, the velocity at the entrance flow speed into the reduced test section was calculated. The velocity at the inlet of the secondary test section was fixed at U_0 = 6, 8, and 10 ± 0.15 m/s, and the pressure upstream of the wedge at the inlet, p_0, was varied between 35 and 150 kPa. The freestream cavitation number, σ_0, is defined as

$$\sigma_0 = \frac{(p_0 - p_v)}{\frac{1}{2}\rho U_0^2} \tag{3.1}$$

where p_v is the vapour pressure of water, and ρ is water density. The dissolved oxygen content was maintained at approximately 50%.

3.4 Surface Pressure Measurements

Static pressure at different locations on the wedge was also measured to aid the understanding of the observed flow physics. The pressure from these taps was measured using a PX20-05A5V transducer. In addition to static pressure measurement, unsteady pressure on the wedge surface was also measured using flush mounted surface pressure probes. PCB 138M101 transducer and ICP Sensor 480CO2 signal conditioner was embedded in the wedge model to facilitate the unsteady pressure measurements. The unsteady pressure signals were sampled at a frequency of 250 kHz using a NI PCI-MIO-16E-4 card triggered using the common time base between X-ray measurement system and the data acquisition system.

3.5 High Speed Cinematography

The cavitating flow around the wedge was imaged with a Phantom v730 high-speed video camera. A 90 mm focal length lens was used to record a viewing area of 15.5 by 4.5 cm, and the flow was illuminated using Arrilux lamps. The frame rate of the video recordings was 4000 frames per second (fps), with a 35 microsecond exposure time, and the camera was triggered manually. Two high speed video cameras were used to simultaneously record the cavitation events from the top and side views. The cameras were synchronized using the Phantom Cine Control software and were triggered using a TTL signal generated by a Stanford DG-535 delay generator. The top and side views were filmed only for the flow speed of 8 m/s. The top view camera was mounted from the test section top, and was fitted with a multiple focal length lens of range 35-55 mm. The view area and unit dimensions in the top and the side views were not the

same. The top view videos were processed to scale up to the side view videos using Matlab.

3.6 X-ray Densitometry

A cinematographic X-ray densitometry system was used to measure the spatial distribution of void fraction for the cavitating flow around the wedge. A complete description of the system is provided by Mäkiharju (2012), and Mäkiharju *et al.* (2013). A brief description is provided here. The X-ray densitometry system had a source capable of 433 mA at 150 kV, and the imaging system is comprised of an image intensifier coupled with a high-speed camera (Vision Research Phantom V9.0). Note that the fraction of photons of any one specific photon energy that is not attenuated is related to the mass attenuation coefficients, densities and thicknesses of all the materials present along the path of the beam. Based on the Beer-Lambert law, for a domain with *N* distinct materials we can write

$$\frac{I}{I_0} = e^{-\sum_{n=1}^{N} \frac{x_n \mu_n}{\rho_n}} = \prod_{n=1}^{N} e^{-x_n \mu_n / \rho_n} \tag{3.2}$$

where I_0 is the original intensity of the photon beam, I is the intensity of the photons transmitted, $\frac{\mu_n}{\rho_n}$ is the mass attenuation coefficient, ρ_n is the density, x_n is the mass thickness ($x_n = \rho_n h_n$), and h_n is the length of traversed beam path through material *n*. The attenuation coefficient is a known property of photon energy and any material in the domain, and is related to the material density and its atomic properties. Therefore for a single material, $N = 1$, a measure of the change in intensity can be converted into a measure of the average density of the material along the beam path. In the case of two-phase gas-liquid flows, we can obtain a *quantitative* measure of the void fraction, α, which is given by

$$\alpha = \ln\left(\frac{I_m}{I_w}\right) / \ln\left(\frac{I_a}{I_w}\right) \tag{3.3}$$

This equation provides the void fraction along any given beam path through a test section as a function of the intensities, *I*, of photon fluxes having passed through a test section filled with a mixture, all water, or all air at any one given photon energy. The accuracy of the void fraction measurement has been validated against those obtained by use

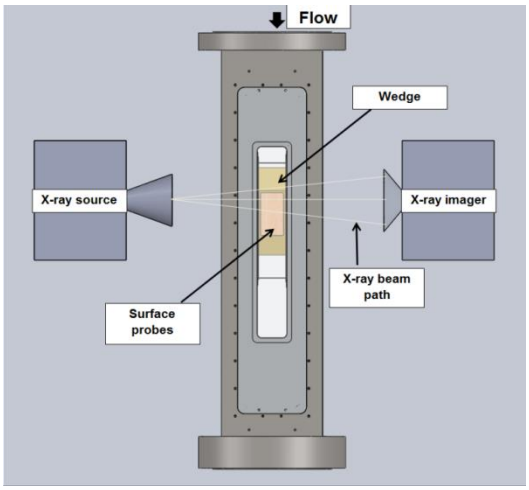

Figure 3.3: X-ray densitometry system schematic

of water phantoms representative of the observed void fractions. An estimate for the maximum void fraction was attained by using water phantoms, and this calibration sets the maximum gray-scale value for the camera. The RMS uncertainty of absolute void fraction for any pixel in a single (non-time averaged) frame is approximately 2%. A more comprehensive discussion on the method's uncertainty and the potential sources for error was provided by Mäkiharju *et al.* (2013). A schematic of X-ray setup is shown in Figure 3.3.

3.7 Inflow Measurements of Empty Test Section

The nature of the flow into the reduced section was characterised using Laser Doppler Velocimetry (LDV) and pitot probes. A Measurement Science Enterprise, (MSE) portable LDV system with a custom made traverse was used for the flow characterisation. The type of the flow into the reduced test section without the wedge was characterised using LDV. Figure 3.4 shows the location of points where the LDV measurements of the flow field were done. Figures 3.5 and 3.6 show the velocity profile in the test section without the wedge in transverse and span wise direction respectively. From the spanwise profile it is evident that the flow in the test section is turbulent. Near wall velocity profiles in the transverse and spanwise direction at the same locations are shown in Figure 3.7 and 3.8 respectively. It can be seen that thickness of the wall boundary layer is around 4 mm in the transverse direction. This is different from the boundary layer thickness measured in the spanwise direction.

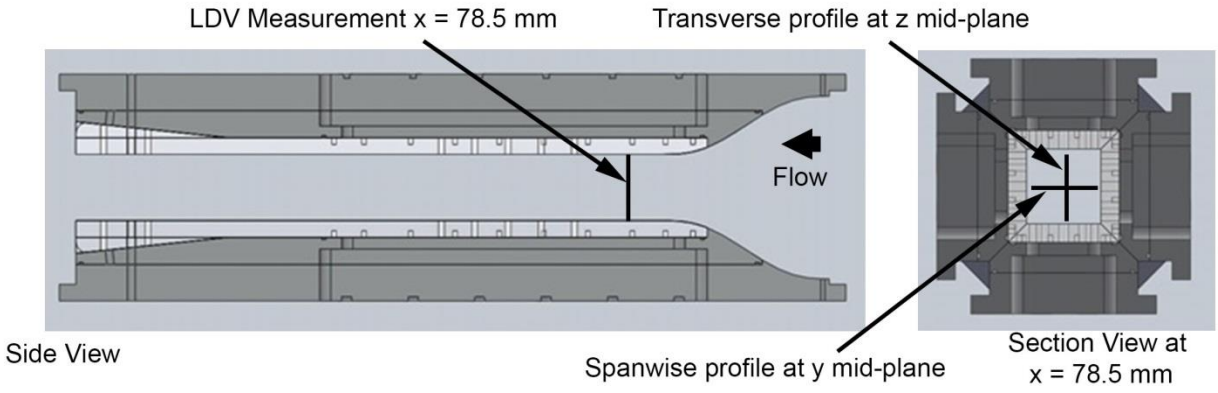

Figure: 3.4: LDV measurement locations of test section flow without wedge

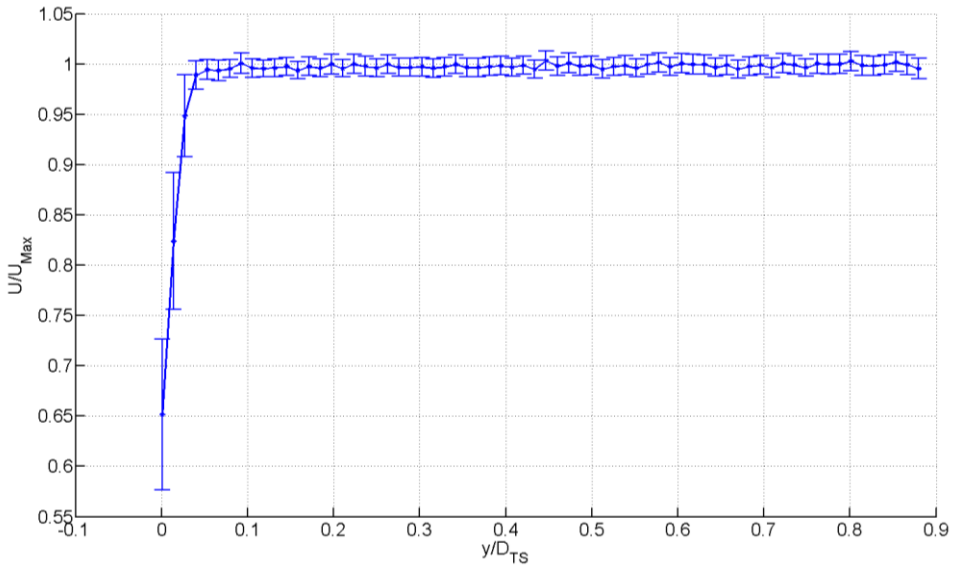

Figure 3.5: Span wise velocity profile from LDV measurements at locations in Figure 3.4. The inlet velocity was $U_{Max} = U_0 = 7.95$ m/s.

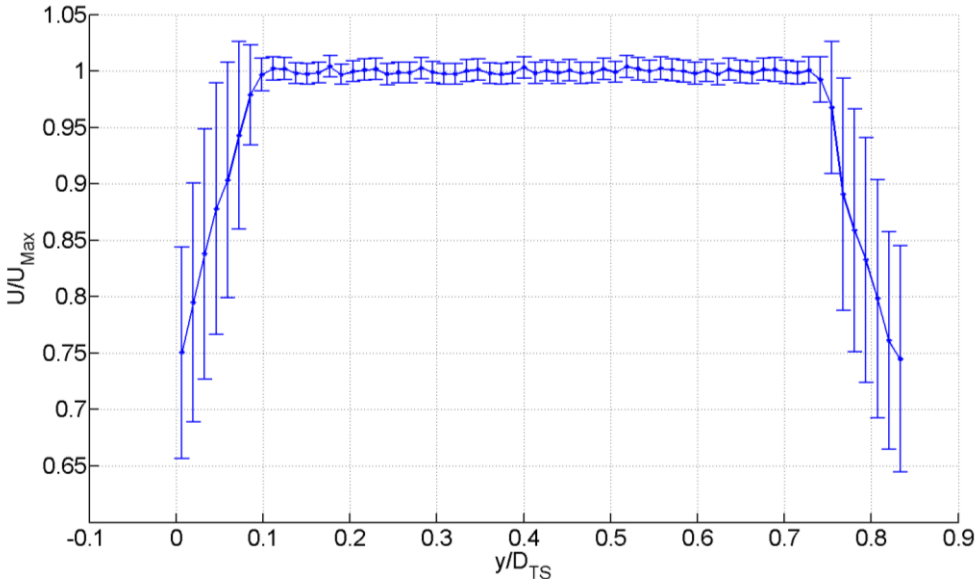

Figure 3.6: Spanwise velocity profile from LDV measurements at locations in Figure 3.4. The inlet velocity was $U_{Max} = U_0 = 7.95$ *m/s.*

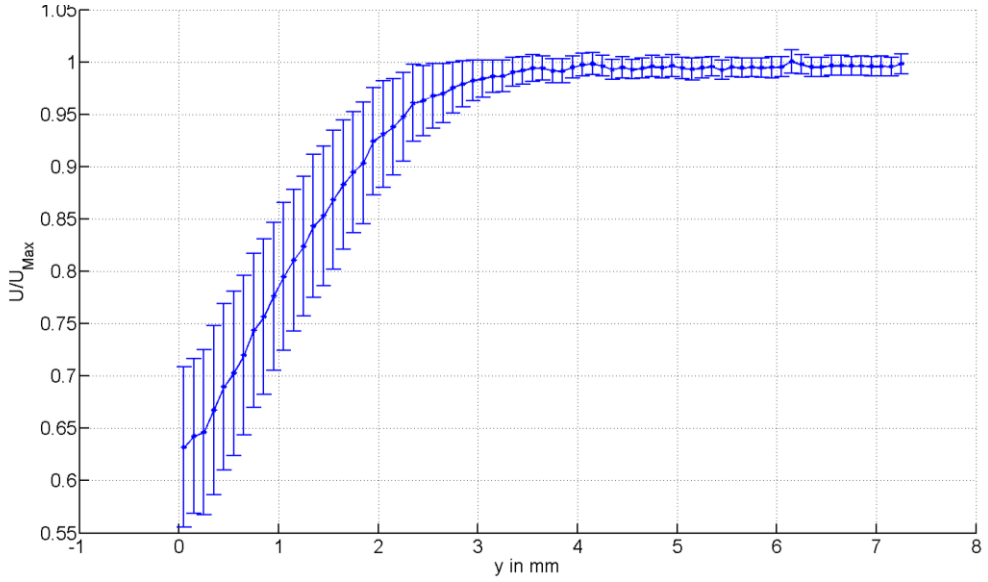

Figure 3.7: Near wall transverse velocity profile from LDV measurements at locations in Figure 3.4. The inlet velocity was $U_{Max} = U_0 = 7.95$ *m/s.*

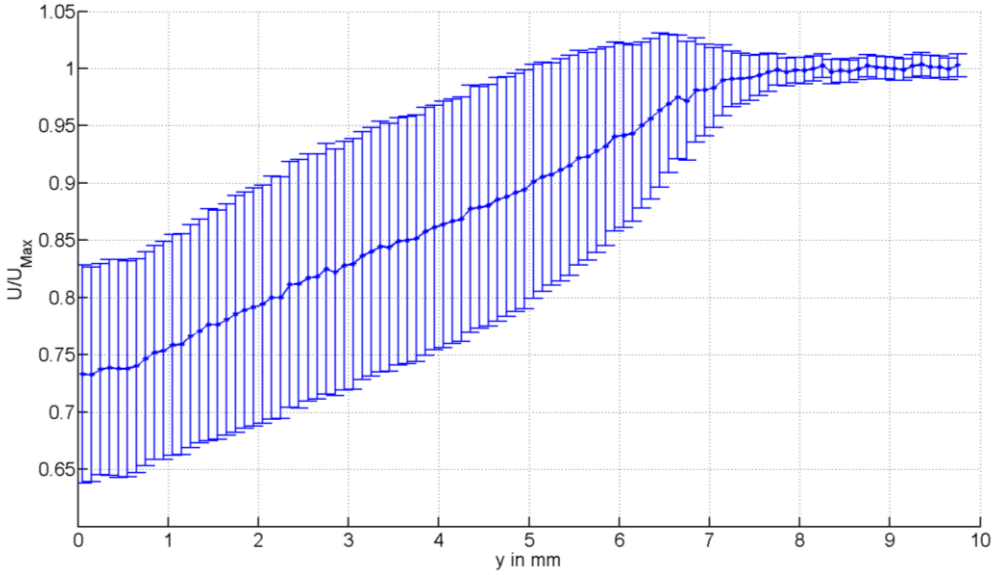

Figure 3.8: Near wall span wise velocity profile from LDV measurements at locations in Figure 3.4. The inlet velocity was $U_{Max} = U_0 = 7.95$ *m/s.*

3.8 Inflow Measurements with Wedge

The characteristics of the flow field with the wedge were also studied to understand the nature of the incoming flow on to the wedge. This was accomplished at two locations: 1) at the entry of the secondary contraction, and 2) 78.5 mm upstream of the wedge apex, as shown in Figure 3.9.

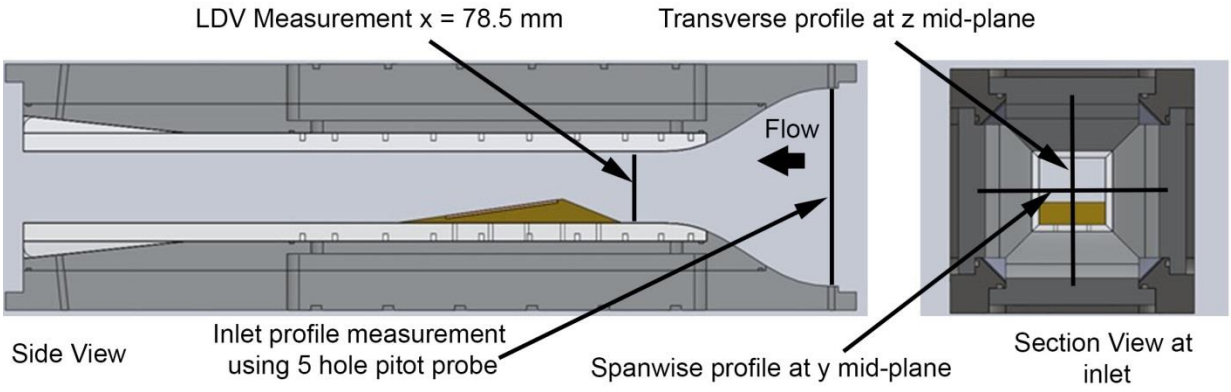

Figure: 3.9: LDV measurement locations of test section flow with wedge and locations with 5 hole pitot probe inflow measurements

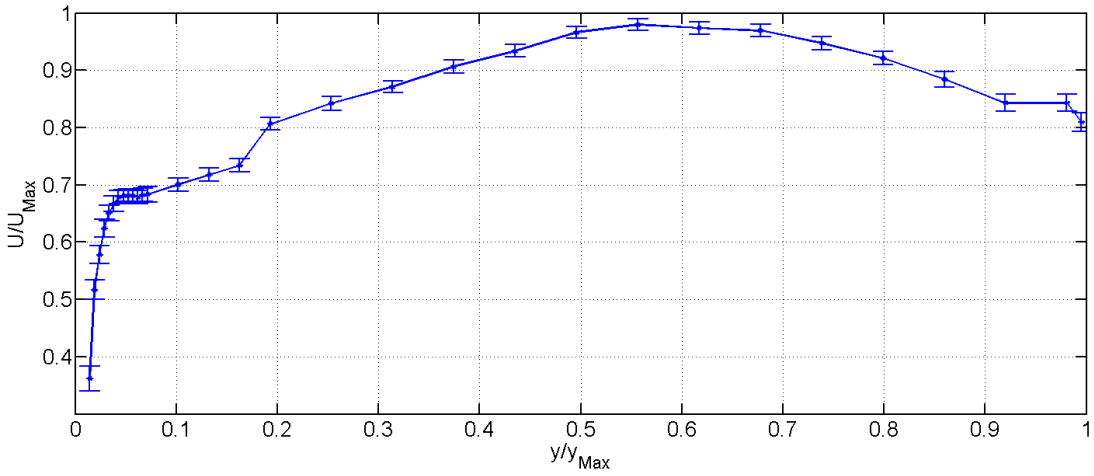

Figure: 3.10: Transverse 5 hole pitot probe measurement velocity profile at inlet of test section flow with wedge and locations with 5 hole pitot probe inflow measurements $U_{Max} = 1.85$ *m/s*

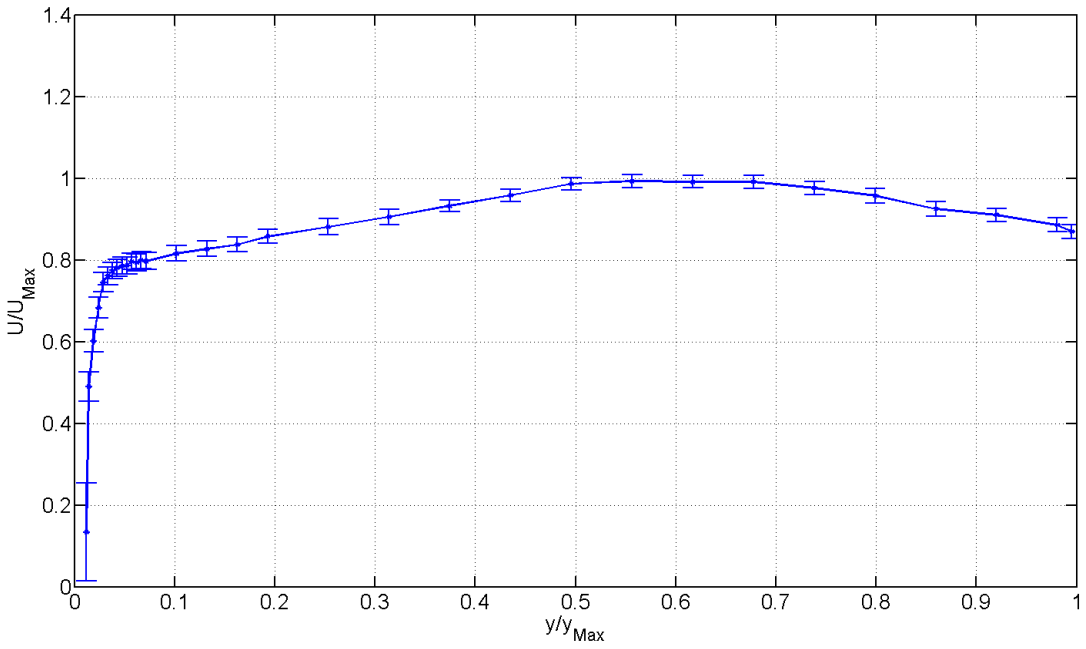

Figure: 3.11: Span wise 5 hole pitot probe measurement velocity profile at inlet of test section flow with wedge and locations with 5 hole pitot probe inflow measurements U_{Max} *= 1.85 m/s*

The velocity profiles were measured using 5 hole pitot probe at the entrance of the secondary contraction. The different pressure between the total and static pressure were measured using inverted manometer with water and air column. The measured velocity profiles in the transverse and span wise directions are shown in Figures 3.10 and 3.11 respectively. The presence of a hump in the transverse velocity profile is clearly visible. This could be due to the presence of the wedge or the flow acceleration at the entry of the secondary contraction.

3.9 Near Wedge Velocity Profile

The turbulent velocity profile upstream of the wedge was also measured using LDV. Figure 3.12 shows the velocity profile in the transverse direction. The near wall profile shown in Figure 3.13 suggests that turbulent boundary layer thickness upstream of the wedge is about 2 mm.

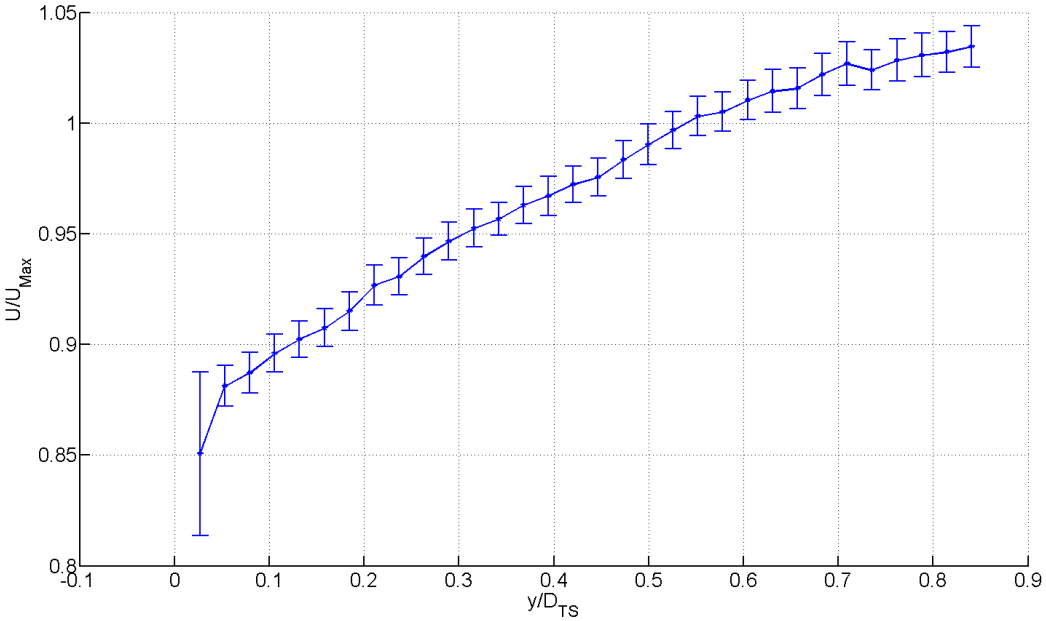

Figure: 3.12: LDV measurements of velocity profile in transverse direction at location X=79mm from wedge apex in the span wise mid plane U_{Max} *=1.85 m/s*

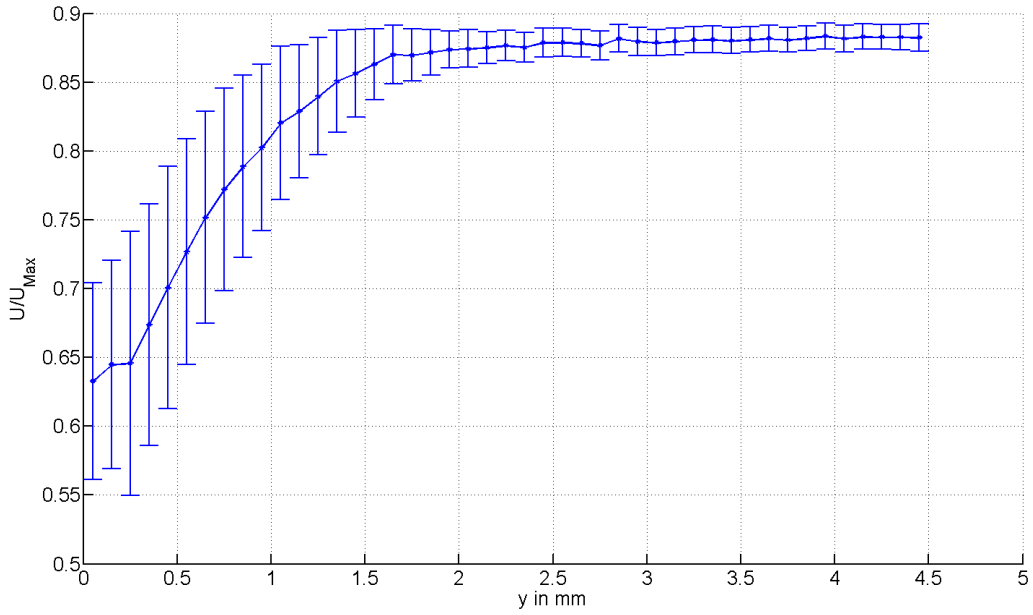

Figure: 3.13: Near wall LDV measurements of velocity profile in transverse direction at location X=79mm from wedge apex in the span wise mid plane U_{Max} *= 1.85 m/s*

.

CHAPTER 4

Analytical Prediction of Cavity Shape

Partial cavitation in separated flows occurs in regions of low pressure aft of the separation point. Since the pressure in the cavity is close to vapour pressure and is close to being constant, the shape of the cavity that is attained for a given geometry depends upon the kinematic flow conditions that can sustain a constant pressure region. The use of complex variables to solve for streamlines for fluid flow over objects with specific conditions on a bounding streamline has been existent for quite some time (Kirchoff (1869)). The use of one such method to predict a cavity shape for the present geometry would be useful in the interpretation of the observed results. The details of the method and the results will be discussed in this chapter.

Indeed, such methods make several simplified assumptions about the nature of the flow, such as irrotational, incompressible without phase change. A solution of cavitating flow over such a wedge would be valid within the limits of the assumptions, but satisfying the equations of motions. Nevertheless, knowledge about the nature of a flow over the wedge that satisfies mass and momentum conservations in addition to having a constant pressure boundary at a cavity interface can be useful for the following reasons:

1. It provides a basis to compare experimentally observed cavity profiles to look for regimes of cavitation within which the observed flow resembles the analytical flow. This is useful

because it suggests the importance of simple conservation relations with a constant pressure cavity in certain regimes of cavitation, over other physics of vapour production, convection time scales which are prominent in other regimes.

2. The analytical solution provides a cavity shape with the assumption of constant pressure within the cavity. In reality, the pressure in the cavity and its closeness to being a constant is not known. Geometric comparison of experimentally observed profiles with analytical profiles can also provide information about nature of the pressure distribution in the cavity and its closeness to being at constant pressure.
3. In the case of shedding cavities, comparison with analytical shapes also provides information about the instances when the simplified assumption based on equations of motion sustaining a constant pressure region fails to hold good. Comparison of instantaneous void fraction fields obtained using X-ray densitometry measurements with the analytical profiles for shedding cavities show the extent to which a growing cavity confirms to the shape predicted using simplified assumptions. This can provide insights into the interpretation of the flow field in the context of periodic shedding.

With this background, the present chapter will discuss the methodology used to predict the cavity shapes, the results obtained using the analysis and broad trends observed in the flow.

4.1 Basic Theory

Fluid flow over objects can be represented in a mathematical formulation using partial differential equations. Depending upon the flow scenario, such as the absence or presence of compressibility, rotation, viscosity, the equations of motion can be formulated and solved either analytically or numerically for the resulting flow field. For the case of 2-D incompressible,

homogeneous, irrotational flow, without the effect of viscosity, the stream function and velocity potential that satisfies the following relations completely describe the flow.

$$\nabla \cdot \vec{U} = 0 \tag{4.1}$$

where $\vec{U}$ is the velocity vector with the components. In a Cartesian frame of reference, *u* and *v* represent velocity components along the X-Y directions. For an inviscid, irrotational, incompressible flow, the velocity components can be expressed in terms of the stream function $\psi(x, y)$ and velocity potentials $\phi(x, y)$, using the following relations,

$$u = -\frac{\partial \psi(x, y)}{\partial y} = \frac{\partial \phi(x, y)}{\partial x} \tag{4.2}$$

$$v = \frac{\partial \psi(x, y)}{\partial x} = \frac{\partial \phi(x, y)}{\partial y} \tag{4.3}$$

From Equations (4.2) and (4.3), it can be inferred that the functions $\psi(x, y)$ and $\phi(x, y)$ satisfy the Cauchy-Riemann relations. Since these functions represent fluid flow which is both incompressible and irrotational, they are both smooth and well defined at all points in the flow domain. Thus they qualify to be real and imaginary parts of an analytic function which can represent fluid flow in the physical complex plane *z*. This is the premise of using complex variables to solve for incompressible, irrotational fluid flow problems over objects. Details of the type of the method and its applications can be found in classic theoretical texts such as, Prandtl & Tietjens (2011), Milne- Thompson (2011), and Glauert (1983).

4.2 Free-Streamline

After solving for velocity potential function, the resulting pressure field can be determined using

the relation

$$p(x, y) = P_T - \frac{1}{2}\rho V^2 \tag{4.4}$$

Along a given streamline the pressure is uniquely determined as a continuous function in the flow domain. There are instances of flow scenarios that have regions in the flow field marked by a bounding streamline, called the "*Free-streamline*", across which pressure can change drastically. Examples include jets, wakes, cavities, etc. One of the earliest attempts to exploit the complex variable approach to solve for flow fields involving free stream lines across which the pressure changes was done by Kirchoff (1869). Hence, the method and the kind of flows that have such pressure characteristics are termed as Kirchoff's flow. A good review of the method can be found in Brennen (1994).

Indeed, the solution of such free stream line flows does not come without the specification of certain information about the free stream line. The use of a frame work based on the governing equations ensures that such a free stream is in mechanical equilibrium with the underlying flow. However, information regarding the location of the separation point, in case of wake flows, and the type of the flow scenario at the outlet, such as open wake, re-entrant jet, *etc*, has to be specified for the problem to be well posed. Thus, there is an element of "modelling" involved while using this method to predict the flow field. The final solution represents a flow field that satisfies the conditions represented by the "model" in conjunction with mass and momentum conservation.

4.3 Present Study

With the aforementioned background, the method can now be applied to the present study. The

Free-streamline model of the two-dimensional cavity flow adopted in the present is based on that of Wu *et al.* (1971). The present approach is very close to that of Laberteaux & Ceccio (2001a).

Figure 4.1 represents the flow over the wedge in the physical plane Z. The *Free-streamline* separates at the apex of the wedge represented by the point *D*, to form a closed cavity shape with a re-entrant jet. Thus the re-entrant jet "model" is used to predict a cavity shape that can sustain a reversed flow at cavity closure. The methodology of the solution will become evident by examining the same flow in the f-plane defined by ϕ on the real axis and ψ on the imaginary axis, where

$$f(x+iy) = \phi(x,y) + i\psi(x,y) \tag{4.5}$$

and, $\phi(x,y)$ and $\psi(x,y)$ are, respectively, the velocity potential and the stream function. So for the above setup the stream line and velocity potential turn out to be, Figure 4.2.

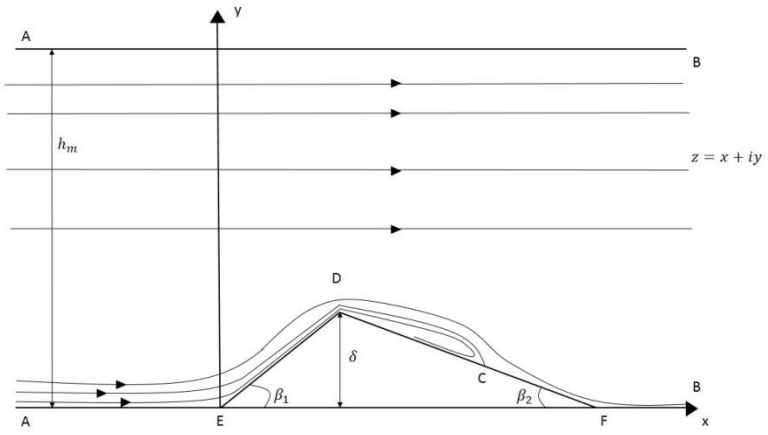

Figure 4.1: Potential cavity flow in the physical z-plane

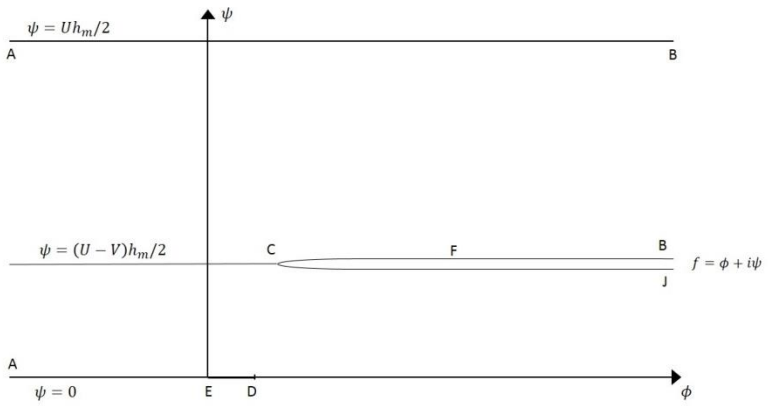

Figure 4.2: Potential cavity flow in the complex potential f-plane

ED represents the wetted surface of the wedge from leading edge to apex. It should be noted that the effect of the rear portion of wedge after the apex is in the specification of suitable boundary conditions at the vicinity of the cavity closure. Here h_m represents twice the height of tunnel, with points *A-A* and *B-B* being singular points at upstream and downstream infinities respectively. The inflow and outflow velocities are represented as *U* and *V*. Since the model used is a re-entrant jet model, the re-entrant fluid flows into a Riemann surface associated with the branch point *C*. Here the complex velocity is defined by

$$w = \frac{df}{dz} = u - iv = |w|e^{i\theta} \tag{4.6}$$

And the hodograph variable ω is defined by,

$$\omega = \log\left(\frac{q_c}{w}\right) = \tau + i\theta \tag{4.7}$$

From the flow diagram we can infer that the flow changes direction at three points: *E, C,* and *F*. The complex velocity ceases to be analytic at these points. Thus the solution to the problem

involves finding a suitable function of ω that satisfies the flow angles represented at the appropriate regions mentioned in Figure 4.1 and 4.2. To accomplish this, the *f*-plane is transformed into another parametric plane, (ζ -plane), such that the boundary points fall along the real axis of the τ -plane. This amounts to finding a complex velocity function $\omega(\zeta)$ that satisfies the boundary conditions along the real axis, hence solving a "Riemann-Hilbert Problem". Schwarz-Christoffel transformation used to map the *f*-plane into the τ -plane is given by

$$\frac{df}{d\zeta} = \frac{A\zeta\left(\zeta^2 - c^2\right)}{\left(\zeta^2 - a^2\right)\left(\zeta^2 - b^2\right)} \tag{4.8}$$

This formula makes possible to have f continued analytically into the entire ζ -plane, which is represented in Figure 4.3.

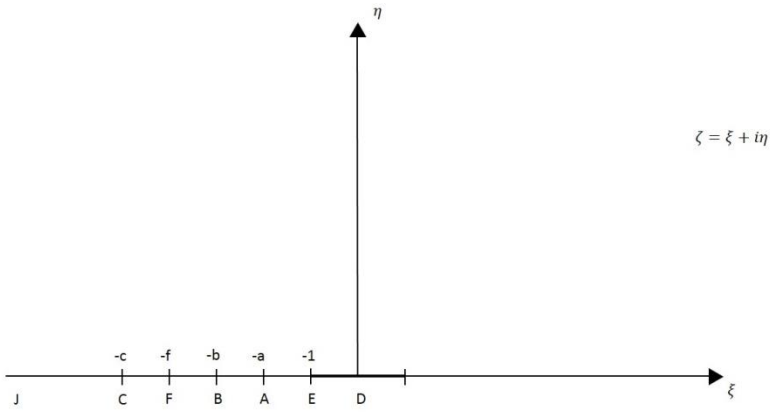

Figure 4.3: Potential cavity flow in the parametric ζ-plane

Using equation (4.8) and because of the singular behaviour of f, at ζ *a, b* and ∞, it follows that

$$f(\zeta = a) = \pi i \frac{p(a)}{q'(a)} = \pi i \frac{A(c^2 - a^2)}{(\zeta^2 - a^2)(\zeta^2 - b^2)}$$

And in the f-plane at ζ = a, which represents the value of the stream function on the top wall at the inlet,

$$f(\zeta = a) = i \frac{1}{2} U h_m$$

And therefore we finally obtain

$$U h_m = \pi A \frac{(c^2 - a^2)}{(b^2 - a^2)} \text{ at } \xi = a \text{ and } Z = A \tag{4.9}$$

Similarly,

$$V h_m = \pi A \frac{(c^2 - b^2)}{(b^2 - a^2)} \text{ at } \xi = b \text{ and } Z = B \tag{4.10}$$

Substituting for a constant A, we find the ratio between the equations (4.8) and (4.9):

$$\frac{U}{V} = \frac{(c^2 - a^2)}{(c^2 - b^2)} \tag{4.11}$$

Boundary conditions for the hodograph variable ω are determined as

$$\begin{cases} \theta^+(\xi) = \theta(\xi, 0+) = -\pi - \beta_2 \quad (-\infty < \xi < -c) \\ \theta^+(\xi) = \theta(\xi, 0+) = -\beta_2 \quad (-c < \xi < -f) \\ \theta^+(\xi) = \theta(\xi, 0+) = 0 \quad (-\infty < \xi < -c) \\ \theta^+(\xi) = \theta(\xi, 0+) = \beta_1 \quad (-1 < \xi < 0) \end{cases} \tag{4.12}$$

Here the superscript + refers to the positive side of the imaginary axis. The solution to this the Riemann-Hilbert problem for the hodograph variable is got by using the Poisson integral,

$$\omega(\zeta)=\frac{1}{\pi}\int_{-\infty}^{+\infty}\frac{\theta^{+}(\xi)}{\xi-\zeta}d\xi \tag{4.13}$$

Using the symmetry of the problem, it follows that:

$$\omega(\zeta)=T_1+T_2+T_3+T_4$$

$$T_1=\frac{\pi+\beta_2}{\pi}.\ln\left(\frac{c-\zeta}{c+\zeta}\right)$$

$$T_2=\frac{-\beta_2}{\pi}.\ln\left(\frac{f+\zeta}{c+\zeta}\right)$$

$$T_3=\frac{\beta_1}{\pi}.\ln\left(\frac{\zeta-1}{\zeta+1}\right)$$

$$T_4=-\frac{\beta_2}{\pi}.\ln\left(\frac{c-\zeta}{f-\zeta}\right)$$

The complex velocity then becomes

$$w(\zeta)=e^{-\omega(\zeta)}=\left(\frac{c+\zeta}{c-\zeta}\right)\left(\frac{f+\zeta}{f-\zeta}\right)^{\alpha}\left(\frac{\zeta+1}{\zeta-1}\right)^{\gamma} \tag{4.14}$$

with $\alpha=\frac{\beta_2}{\pi}$ and $\gamma=\frac{\beta_1}{\pi}$. It can be inferred that at point A and B, respectively, for ζ approaching $-a$ and $-b$, respectively, and for w approaching U and V, we find

$$U = \left(\frac{c-a}{c+a}\right)\left(\frac{f-a}{f+a}\right)^{\alpha}\left(\frac{a-1}{a+1}\right)^{\gamma} \tag{4.15}$$

$$V = \left(\frac{c-b}{c+b}\right)\left(\frac{f-b}{f+b}\right)^{\alpha}\left(\frac{b-1}{b+1}\right)^{\gamma} \tag{4.16}$$

By making the ratio between the equations (4.15) and (4.16) and substituting by the equation (4.10), we find the expressions of c and k, given by

$$c = \frac{kb-a}{1-k}$$

$$k = \left(\frac{(f-a)(f+b)}{(f+a)(f-b)}\right)^{\alpha/2}\left(\frac{(a-1)(b+1)}{(a+1)(b-1)}\right)^{\gamma/2}$$

The solution in the z-plane is given by:

$$z(\zeta, a, b) = \int_{-1}^{\zeta} \frac{1}{w}\frac{df}{d\zeta}d\zeta \tag{4.17}$$

By substituting the constant A in the equation (4.9), we finally obtain the following equation

$$z(\zeta, a, b, f) = \frac{(b^2-a^2)}{(c^2-a^2)}\frac{Uh_m}{\pi}\int_{-1}^{\zeta}\left(\frac{f-\zeta}{f+\zeta}\right)^{\alpha}\left(\frac{\zeta-1}{\zeta+1}\right)^{\gamma}\frac{-\zeta(\zeta-c)^2}{(\zeta^2-a^2)(\zeta^2-b^2)}d\zeta \tag{4.18}$$

Point D corresponds to the point $\zeta = 0$ and we have also, $\mathrm{Im}(z(\zeta=0)) = l_m/2$ where l_m is twice the height of the apex of the wedge in the physical *z*-plane. Thus if we substitute λ, the blockage ratio of the wedge, it follows that:

$$\lambda(\zeta, a, b, f) = \mathrm{Im}\left(\frac{(b^2 - a^2)}{(c^2 - a^2)} \frac{U h_m}{\pi} \int_{-1}^{0} \left(\frac{f - \zeta}{f + \zeta} \right)^{\alpha} \left(\frac{\zeta - 1}{\zeta + 1} \right)^{\gamma} \frac{-\zeta(\zeta - c)^2}{(\zeta^2 - a^2)(\zeta^2 - b^2)} d\zeta \right) \tag{4.19}$$

4.4 Method of Solution

There are four constants *a, b, c*, and *f* which uniquely determine the flow field. Since *c* can be written as a function of *a, b,* and *f,* there are only 3 unknowns that needs to be determined for a given condition. The three conditions imposed are,

1. The geometrical parameters of the tunnel give a condition. The equation (4.19) is used to calculate the value of, $\lambda = \frac{l_m}{h_m}$, for a given value of *a, b,* and *f*. Based on the values of l_m and h_m, the value of obtained from Equation (4.19) should be 0.33.

2. Free stream cavitation is used to set the value of U, which is given by, $U = \frac{1}{\sqrt{1+\sigma}}$ .This provides another relationship between the parameters, *a, b,* and *f*.

3. Another constraint is the length of the wedge which is determined by the co-ordinate of the point F. It is got by solving Equation (4.18) from -1 to *-f*. It should be noted that *–a*, and *–b* are singular points, if one choses a path along a real axis. In this case the principal value of the integral is used to estimate the co-ordinate of the point F.

   $X_F = \frac{\lambda}{\tan(\beta_1)}$,with, $X_F = \frac{EH}{h_m}$

4. The above equations are solved with the constraints that on the values of *a, b, f* and *c* such as $1 < a < b < f < c$

To determine the co-ordinates of the stagnation point, (4.18) is integrated from $-f$ to $-c$. It should be noted that since f is a branch point for the integrand in Equation (4.18), an appropriate branch is chosen such that C is in the first quadrant of the z-plane. The cavity profile is got by integrating Equation (4.18) along the imaginary axis from 0 to ∞. Both the cavity profile and the stagnation point are shown in the Figure 4.4 below. The re-entrant jet thickness (L_j) is obtained using the expression,

$$L_j = (U - V) \tag{4.20}$$

4.5 Solutions

The table below shows the combination of the values of parameters and their corresponding cavitation numbers. The profiles for the given cavitation numbers are shown in Figure 4.5

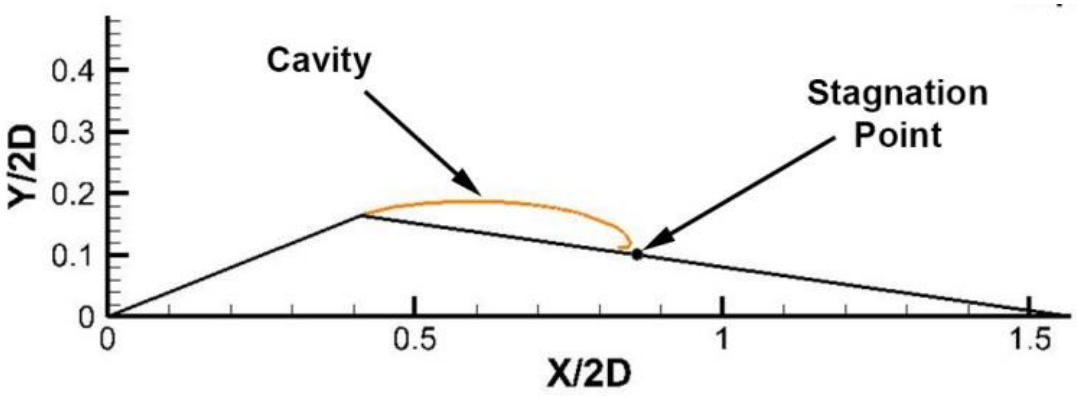

Figure 4.4: Analytical cavity shape at σ = 2.24

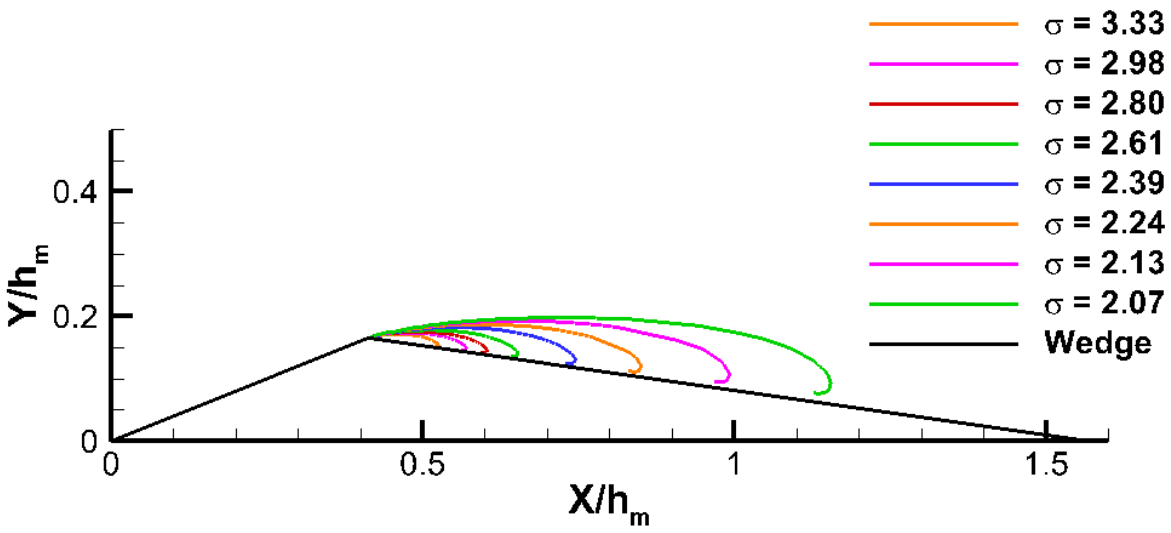

Figure 4.5: Analytical cavity shapes as function of free stream cavitation number

4.6 General Features of Solution

Figure 4.6 shows different cavity shapes obtained for different cavitation numbers. Table 4.1 shows the variation of *U, V* and the length of the re-entrant jet thickness. In order to understand the physical significance of this observation, we need to look at the definition of the parameters.

$$p_\infty + \frac{1}{2}\rho U^2 = p_c + \frac{1}{2}\rho q_c^2 = p_s \tag{4.21}$$

where, p_c is the cavity pressure, q_c is the velocity at the interface and p_s is the stagnation pressure of the flow. Based on Equation 4.21, we get back the expression for cavitation number by setting a constant value of $q_c = 1$.

$$\sigma = \frac{(p_\infty - p_c)}{\frac{1}{2}\rho U^2} = \frac{1}{U^2} - 1 \tag{4.22}$$

a	b	f	c	U	V	σ	L_j
1.011	1.59	1.59	17.06	0.4416	0.4393	4.13	0.00229
1.012	1.68	1.68	18.40	0.4523	0.4499	3.89	0.00241
1.013	1.82	1.82	19	0.4611	0.4582	3.70	0.00293
1.014	1.97	1.97	20.29	0.4708	0.4676	3.51	0.00327
1.015	2.17	2.17	21.77	0.4807	0.4769	3.33	0.00374
1.017	2.81	2.81	26.16	0.5013	0.4963	2.98	0.00504
1.018	3.4	3.40	29.84	0.5129	0.5068	2.80	0.00607
1.019	4.48	4.48	36.49	0.5263	0.5188	2.61	0.00752
1.02	7.44	7.45	53.19	0.5435	0.5331	2.39	0.01044
1.0205	13.2	13.26	82.91	0.5557	0.5417	2.24	0.01400
1.0208	28.6	29.04	153.35	0.5651	0.5455	2.13	0.01963
1.021	70	73.96	320.63	0.5708	0.5436	2.07	0.02720
1.0213	70.3	74.29	323.45	0.5718	0.5448	2.06	0.02700

Table 4.1: Free-streamline solution parameters for different cavitation numbers

For cavitation numbers from Equation 4.22 to be positive, $U<1$. Comparing the value of U with q_c, it is evident that the flow accelerates to achieve this value of q_c at the interface there by experiencing the pressure in the cavity. A decrease in the free-stream cavitation number σ is achieved by increasing the value of U. Based on Equation 4.21, this means that the free-stream pressure drops with an increase in the value U, since the cavity properties remain constant. This means that the value of the pressure difference given by Equation 4.4 along the bounding streamline is lower with an increase in U (by the virtue of reduced free stream pressure), permitting the number of points along the streamline that can satisfy cavity pressure condition to

increase, increasing the cavity area.

The absence of viscosity and hence flow separation in the model makes it possible to have cavities of very small size that is in equilibrium with the flow. Thus, the inception cavitation number of the model represents the value of free stream pressure for which cavity pressure can be felt in only a small region. However, in reality, the separated flow at the wedge apex has region of vapour pressure that is much larger than the region represented by the analytical solution. The assignment of inception cavitation number from the analytical study that matches the experiment depends on the definition based on the matching of shapes rather than the occurrence of the cavitation.

From Figure 4.5 and Table 4.1 it can be inferred that the thickness of the re-entrant jet increases with a decrease in cavitation number. Looking closely at Figure 4.5 it can be seen that the radius of curvature at cavity closure also increases suggesting lower pressure drop due to the turning process. Thus the thickness of the liquid flow that exists at the aft of cavity based on the kinematic boundary conditions obtains a value such that pressure drop by curvature is in equilibrium with the flow. This precludes the existence of re-entrant flow as thick as the cavity itself because to attain such thickness the liquid close to vapour boundary would have to turn 180 degrees at very low radius of curvature (zero) thereby experience very low pressure (closer or lesser than cavity pressure). This is an important observation to the kept in mind.

4.7 Chapter Summary

1. The free-stream line solution of cavitating flow over the wedge can provide information about the closeness of simplified flow physics with actual experimental observation at different regimes of cavitation.

2. Free-streamline theory based solution of cavity shapes for the geometry used in the present study was formulated and solved using re-entrant flow model.
3. Cavity lengths, thickness and thickness of re-entrant jet increase with increase in cavitation number. This trend is consistent with expectations of variation of cavity length with cavitation number for partial cavities as observed in Stutz and Reboud (1997). The comparisons with experiments will be made in the next chapter.

CHAPTER 5

General Cavitation Behavior and Comparisons with Free-Streamline Solutions

In reality, partial cavitation in separated flows can range from stable open cavities to periodically shedding cavities. Unlike the cavitation behaviour presented in the previous chapter using free-streamline theory, different types of cavitation can be observed on the geometry depending upon the cavitation number. The general behaviour of cavitation on the geometry is essential to identifying different types of cavities and the manner in which they differ from each other. This is achieved by studying different types of cavities by systematically varying the inlet cavitation number and flow speeds.

In addition to the identification of different cavity types, comparison of the observed trends in variation of cavity length and thickness with cavitation number, the free-stream line solution can provide important information regarding the match between the actual physics to that modelled using simplified assumptions. Comparisons of the individual cavity profiles can also provide information about the closeness of a constant pressure boundary with kinematic boundary conditions obtained using free-streamline theory to experimentally observed profiles.

This chapter begins with experimentally observed behaviour of the cavity with free-stream cavitation number. Cavity lengths and thicknesses observed in the experiments are reported and compared with the free-streamline solution. The comparison of the experimentally observed

cavity shapes with those predicted using free-streamline theory is also presented in this chapter

5.1 General Cavitation Behaviour: Inception, Transition, and Shedding

Flow in the separated region downstream of the wedge provides conditions for sustained cavitation. The type of cavitation observed depended upon the inlet pressure in the test section. At high pressures and hence cavitation number, the region exhibited minimal to no cavitation. Cavitation inception was first observed for a free-stream cavitation number of σ_0=3.9. Inception was characterized by sparse streaks of cavitating span wise vortices attached to the wedge apex. With further reduction in cavitation number the cavity grew in length with higher density of vapour filled regions within the cavitating region. The cavity remained stable, growing in length until cavitation number of σ_0=2.1.

At cavitation numbers σ_0 less than 2.1, the cavities began to exhibit unstable tendencies. Vapour clouds were shed occasionally, sometimes pinching-off from the leading edge. At a cavitation number of σ_0=1.9, the cavity exhibited periodic shedding of vapour clouds. The geometric behaviour of the cavity, mainly the change in length and thickness, and the regions of cavitation number where they exhibited periodic shedding are discussed in the upcoming sections.

5.2 Cavity Length Variation With Cavitation Number

Variation of the length of the partial cavity with free stream cavitation is well studied. Theoretical studies predict an asymptotic behaviour of cavity length increasing with a decrease in free stream cavitation number. Experimental observations have also seen such behaviour, with also the presence of periodic shedding of vapour clouds at lower cavitation number. Cavity length predicted from the analytical solution described in the previous Chapter is compared with

the experimental observations from high speed videos and X-ray measurements.

5.2.1 Length and thickness from Free-streamline solution

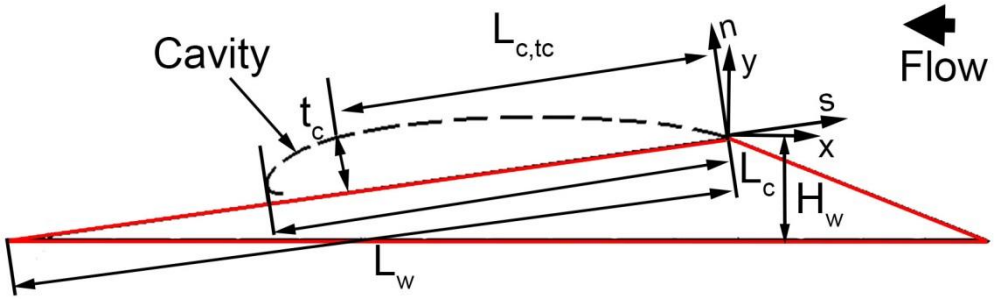

Figure 5.1: Analytical cavity shape properties

Two types of lengths from the analytical profile were calculated. One was the maximum length, and the other the length corresponding to maximum thickness. Both the lengths were measured along the surface of the wedge in the *'s'* direction, and thickness normal to the surface of the wedge in the *'n'* direction. Figure 5.1 illustrates the lengths and thickness measured from the analytical shapes. The figure also shows the definition of the two co-ordinate systems (*x*-*y* and *s*-*n*) that will be used in discussions throughout the study.

5.2.2 Cavity length from High-speed videos

High speed videos of different types of cavitation were also used to measure the observed cavity length and thickness. In this case, the length and thickness of the cavity was assigned by visual inspection. Figure 5.2 illustrates the measurement of cavity length from high-speed videos. It should be noted that for cavities that exhibit periodic shedding of vapour clouds, average of the

maximum length of the cavity for a given cycle was used.

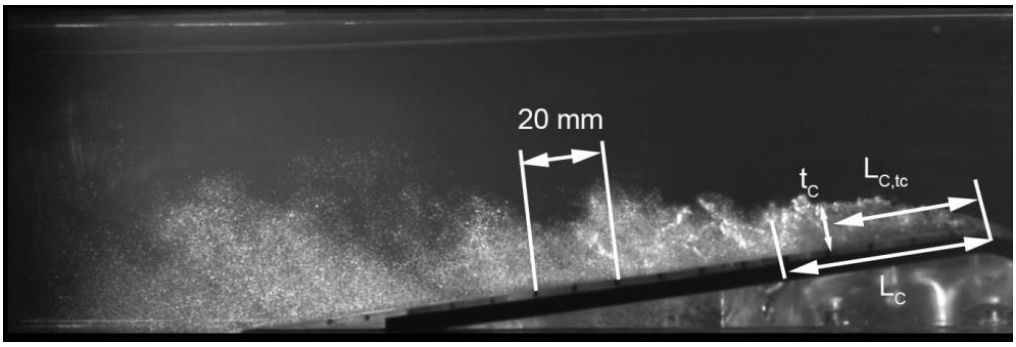

Figure 5.2: Cavity length and thickness measurements from high-speed videos

5.2.3 Cavity length from X-ray measurements

Void fraction measurements using time resolved X-ray densitometry measurements were also used to determine cavity length and thickness. As mentioned in Chapter 3, the use of X-ray radiation for cavitation studies works on the principle of radiation absorption by the cavitating flow. Thus time resolved X-ray videos register the variation of the attenuation along a line of sight as a function of time. To estimate the value of the cavity length from the X-ray videos all the void fraction flow fields were averaged to produce the averaged void fraction filed $\langle\alpha\rangle$ The definitions of the void fraction statistical quantities are shown in Equations 5.1 and 5.2. Figure 5.3 illustrates the measurement of cavity lengths from X-ray measurements.

$$\langle\alpha\rangle = \frac{\sum_{1}^{\#Frames} \alpha}{\#Frames} \tag{5.1}$$

$$\alpha' = \sqrt{\frac{\sum_{1}^{\#Frames} (\alpha - \langle\alpha\rangle)^2}{\#Frames}} \tag{5.2}$$

For stable cavities, iso-lines corresponding to $\langle\alpha\rangle$= 0.05 void fraction in time averaged void fraction flow field measurements was used to designate cavity length. This value was chosen such that the lengths from X-ray and visual observations are not very different, but consistent within different cases of cavitation. Maximum cavity thickness was obtained measuring the distance between the locations of maximum thickness from the wedge surface. Length corresponding to the maximum thickness location was also measured. For periodically shedding cavities, the maximum cavity length for a given cycle was used as the cavity length.

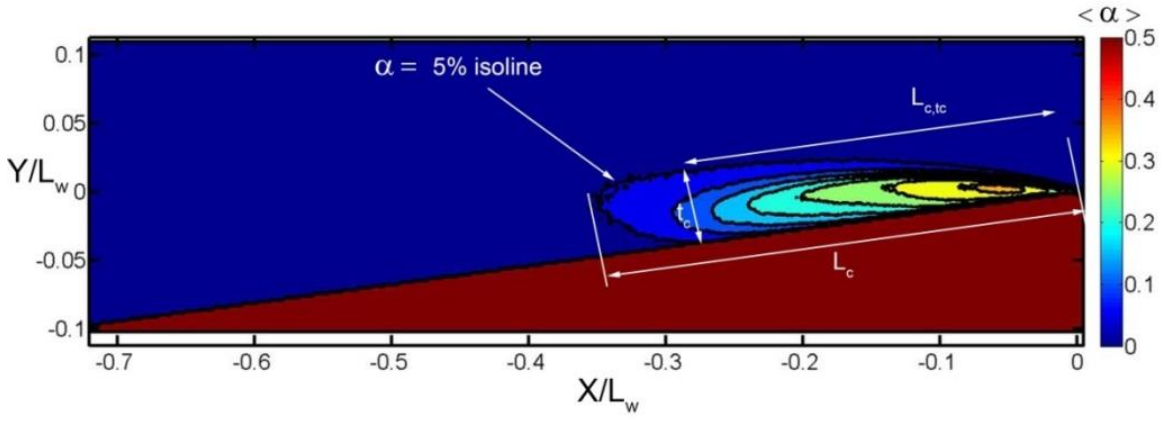

Figure 5.3: Cavity length and thickness measurements from X-ray densitometry

The variation of cavity length and thickness from different measurements with cavitation number are shown in Figures 5.4 and 5.5, respectively. The measured values are also compared with analytically obtained length corresponding to actual cavity length (L_c) and length corresponding to maximum thickness ($L_{c,tc}$) and thickness (t) using Free-streamline solutions.

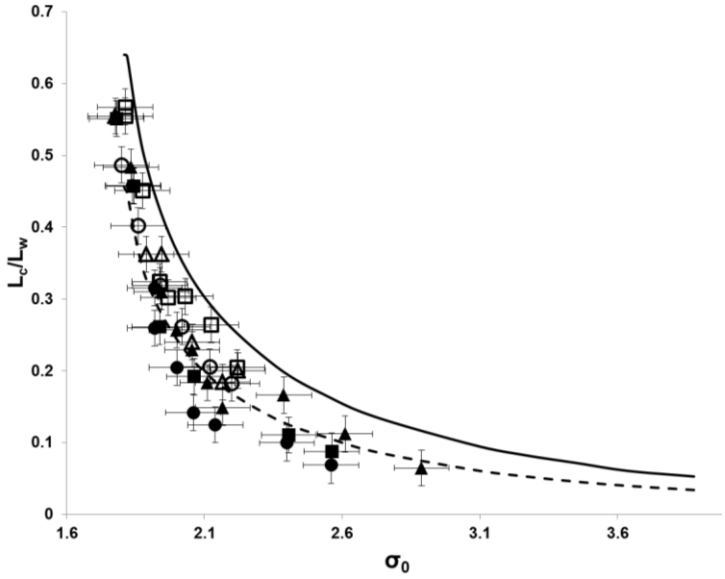

Figure 5.4: Cavity length with σ_0. Experimental cavity length measurements using high-speed video (Δ- 6 m/s, □- 8 m/s, ○- 10 m/s) and X-ray densitometry (▲- 6 m/s, ■- 8 m/s, ●- 10 m/s) compared with analytical cavity lengths. Solid lines represent cavity length L_C and dashed lines represent cavity length at maximum thickness, $L_{C,tc}$

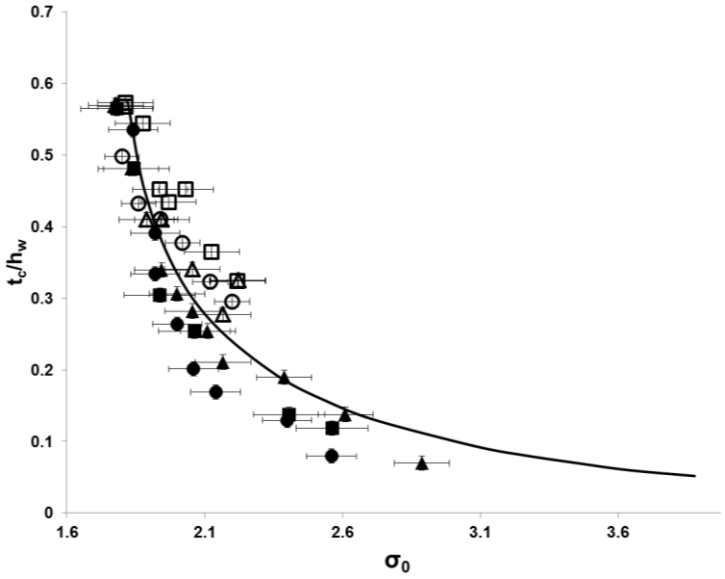

Figure 5.5: Cavity thickness with σ_0. Experimental cavity length measurements using high-speed video (Δ- 6 m/s, □- 8 m/s, ○- 10 m/s) and X-ray densitometry (▲- 6 m/s, ■- 8 m/s, ●- 10 m/s) compared with analytical cavity lengths in solid line.

The prominent features of Figures 5.4 and 5.5 are discussed below.

1. The analytical solutions predicted a higher free stream cavitation number for inception. The analytical inception cavitation number was matched with the actual inception cavitation number σ_0=3.9. To achieve this, the analytical cavitation number were subtracted a value of 0.23. As mentioned in Chapter 4, inception in analytical solution can occur at much higher cavitation numbers than experiments.
2. Experimentally observed cavity lengths matched the cavity length corresponding to maximum thickness of analytically predicted profiles on the whole, but better for stable and transitory cavities. This trend is similar to that observed by Laberteaux and Ceccio (2001a) for stable open cavities. The break-up of the cavity beyond the length of maximum thickness due to an increase in pressure gradients is a possible reason for the observed behaviour because for stable cavities the increase in pressure gradients can hamper the growth of the cavity corresponding to a constant pressure boundary.
3. The actual cavity length obtained from the analytical solution is higher than the experimentally observed cavity length for stable cavities. This is not the case for shedding cavities where the maximum length observed during a given cycle was close to the analytically predicted cavity length for the same cavitation number. However, it should be noted that due to machine precision, solutions for lower values of cavitation number could not be obtained. Nevertheless, the tendency of the observed cavity length to be closer to the maximum cavity length suggests that cavity growth processes are playing an important role when compared to stable cavities. This will be further explored in the upcoming sections.
4. The experimentally observed variation of cavity thickness with cavitation number

matches well with analytically predicted trend.

5.3 Profile Shapes

From Figures 5.4 and 5.5 it is evident that the experimental and the analytical variation of cavity lengths follow the same trend. It should be noted that in a free-stream line solution the cavity pressure is constant, and equal to the value of vapour pressure. However, in reality, the separated flow behind a wedge apex with a divergence angle is not expected to provide a constant pressure along the cavity length. Comparing analytical profiles with averaged and instantaneous void fraction profiles, in the case of periodic shedding, obtained using X-ray densitometry can provide information about the extent to which inviscid mechanisms and conservation laws are responsible for a given cavity shape. For this purpose, three types of cavities are chosen: 1) a stable cavity, 2) cavity exhibiting intermittent shedding of vapour clouds, 3) Periodic shedding.

5.3.1 Stable Cavity

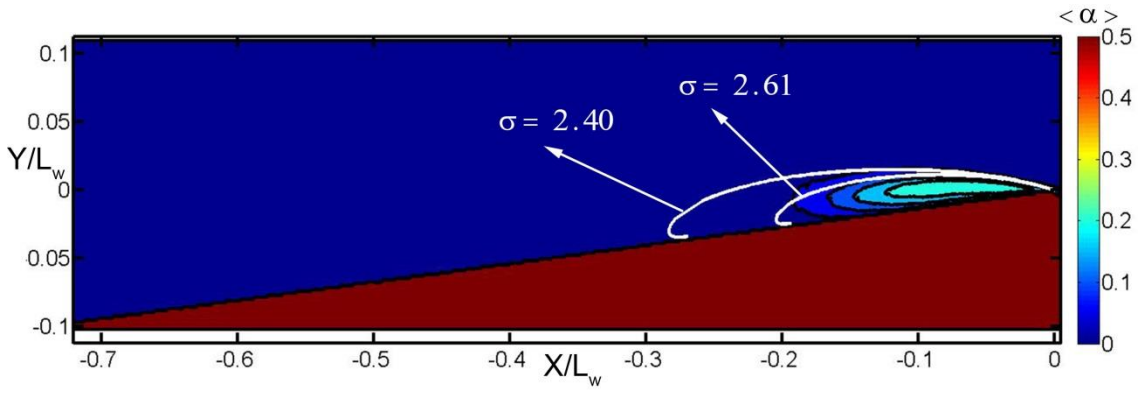

Figure 5.6 Averaged void fraction flow field of a stable cavity at experimental σ_0 =2.18 with superimposed free-streamline profile at σ = 2.40 and σ = 2.61 in solid white line

From Figure 5.6 it can be seen that the free-stream line solution compares with the time-averaged

void fraction profiles using X-ray measurements to a reasonable extent. The obtained cavity shape is compared with two free-streamline solutions that were obtained near the experimental cavitation number. It should be noted here that the choice of cavitation number corresponding to the analytical solution was such that both the thickness and the length matched to a reasonable extent. A match of only the thickness resulted in a longer analytical profile, and a match of length resulted in smaller analytical thickness.

The iso-line represented by $\langle\alpha\rangle$ = 0.05 lies outside the predicted cavity shape for in the middle and aft portion of the cavity for σ *=2.61*, while it was well contained for the cavity shape predicted shape σ *=2.40*. The best match lies somewhere between these two cavitation number. The match with σ *=2.40 is good until the point of maximum thickness, a trend observed in Figure 5.4.*

5.3.2 Transitory Cavity

In the case of transitory cavity, which exhibits intermittent shedding of vapour clouds, the analytical shape is in good agreement with the cavity profile obtained from X-ray measurements. Two analytical shapes corresponding to σ *=2.24 and* σ *=2.13*. The cavity exhibits a slightly blown up 5% iso-line when compared with stable cavity. This is a consequence of averaging a time varying phenomenon. The closeness of the shape until the point of maximum thickness is clearly visible. The difference between analytical cavitation number and the experimental cavitation number begins to reduce as the cavity length approaches the asymptotic portion of the curves shown in Figure 5.4.

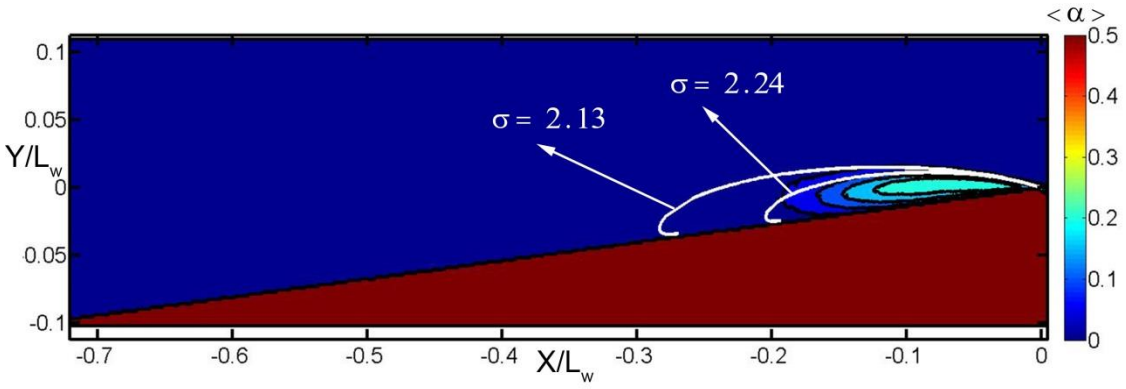

Figure 5.7 Averaged void fraction flow field of a transitory cavity experimental σ_0 *=2.06 with superimposed free-streamline profile at* σ *= 2.13 and* σ *= 2.24 in solid white line*

5.3.3 Periodic shedding Cavity

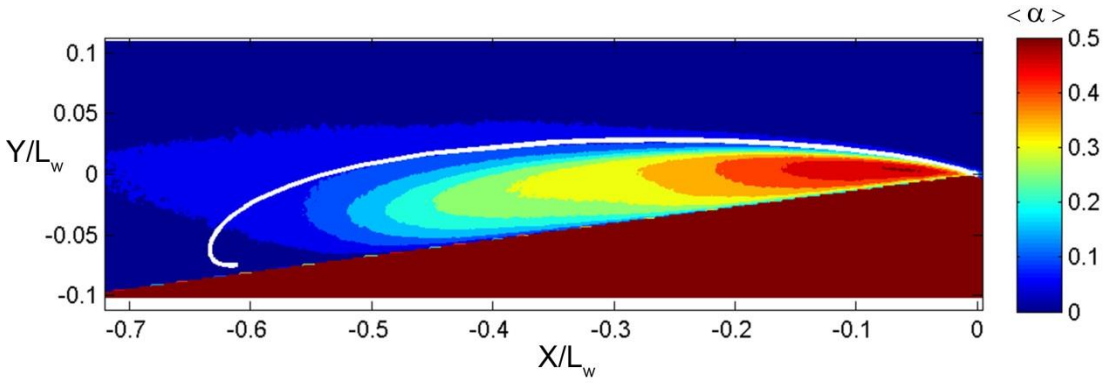

Figure 5.8 Averaged void fraction flow field of a periodic cavity experimental σ_0 *=1.86 with superimposed free-streamline profile at* σ *= 2.06 in solid white line*

A periodic cavity exhibits a bigger blown up 5% iso-line as expected. However, the time averaged thickness is still in good agreement with the free-stream line. It should be noted that the free-streamline solution presented in Figure 5.6 corresponded to the maximum cavity length that could be predicted within reasonable accuracy of converged integral estimates. Thus the same analytical profile was used to compare with periodic shedding at a lower cavitation number as

shown in Figure 5.7. In this case the average length is clearly bigger than that predicted by the analytical method.

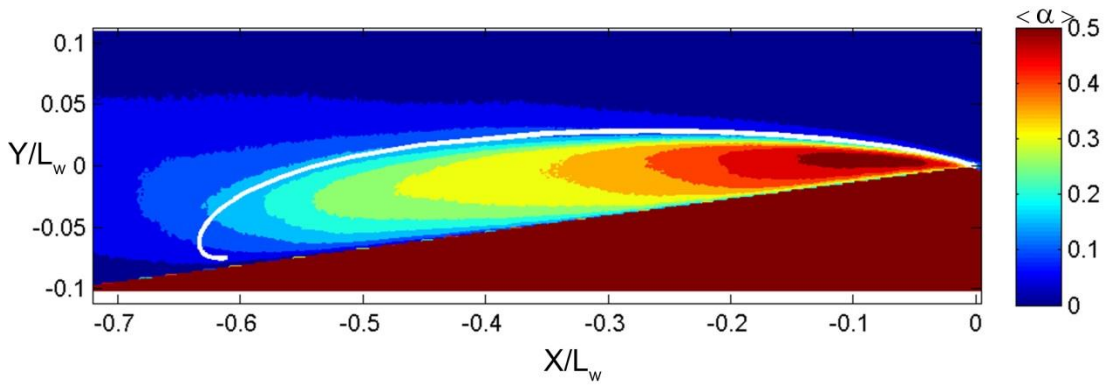

Figure 5.9 Averaged void fraction flow field of a periodic cavity experimental σ_0 *=1.85 with superimposed free-streamline profile at* σ *= 2.06 in solid white line*

As the time averaging of a periodic phenomenon does not truly represent the cavity profile, analytical solutions were compared with instantaneous cavity profiles obtained from X-ray measurements. From these it is evident that on most occasions the maximum cavity length for a given cycle was less than the analytically predicted cavity length. Sometimes, the cavity would grow to match the cavity length, while sometimes it grew to be greater than the cavity length. Figures 5.10 (a) – (c) illustrate this for two cavities exhibiting periodic shedding.

5.3.4 Instantaneous profiles

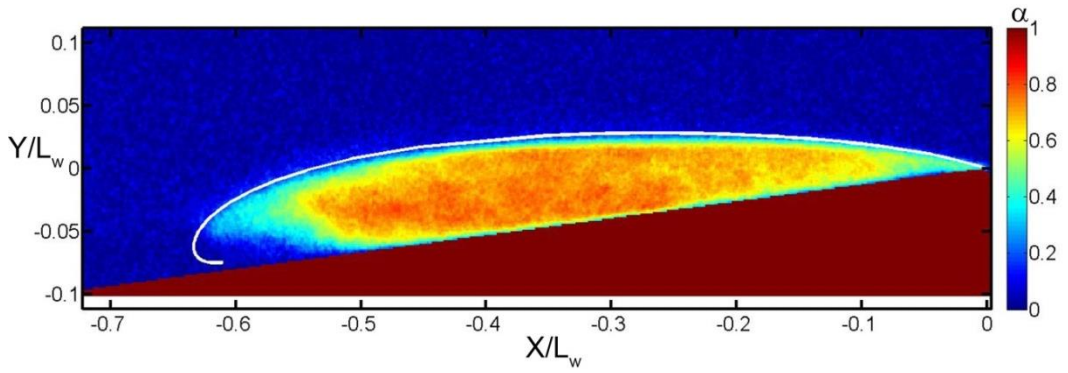

(a)

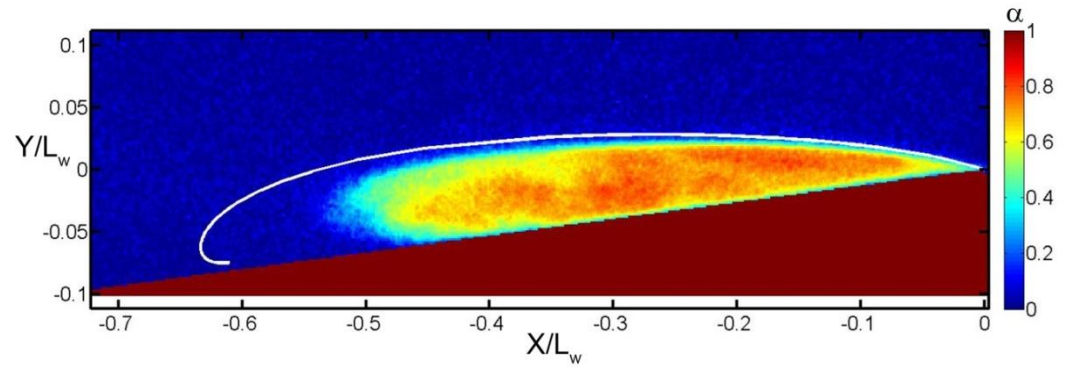

(b)

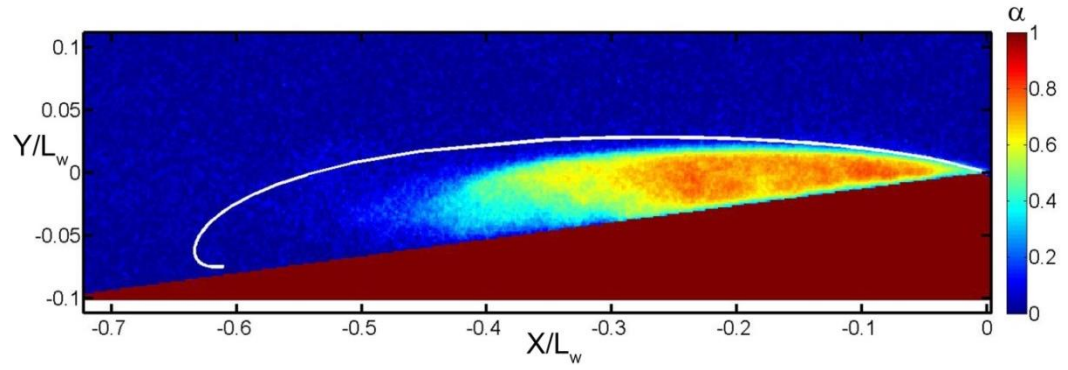

(c)

Figure 5.10 Instantaneous void fraction flow field of a periodic cavity experimental σ_0 =1.85 with superimposed free-streamline profile at σ = 2.06 in solid white line (a) when the maximum cavity length in close to analytical cavity length (b) when the maximum cavity length is ~75% of analytical cavity length (c) when the maximum cavity length is ~50% of analytical cavity length

5.4 Summary of General Trends and Comparisons

1 The variation of cavity length with cavitation number match analytically predicted cavity lengths until to the point of maximum thickness for stable cavities.

2 For intermittent and shedding cavities, maximum length of the cavity for a given cycle matched the maximum cavity length predicted by the free-streamline solution.

3 On the whole, experimentally observed trend matched well with the analytically predicted trends suggesting the importance of mass and momentum conservation on the observed trends.

4 Lengths of instantaneous cavity profiles for shedding cavities resembled the analytically predicted profile to varied degrees. However, the cavity shape and thickness was very close to that predicted by the analytical method. The difference in the matching trend for length and thickness could be due to the cavity growth process which inhibits growth in length by the onset of collapse.

CHAPTER 6

Cavity Dynamics

Based on the observations of the cavity behaviour at different cavitation numbers, it can be inferred that the cavities can be classified into three different types based on the observed cavity dynamics: incipient, transitory, and shedding. Each of these three cavity types have features of flow physics that are responsible for the associated flow dynamics observed. Identification of the differences in the dynamics observed and the corresponding flow features is crucial for understanding the mechanism of transition from stable to shedding cavities.

This chapter deals with the discussion of observed flow features for three cavity types as mentioned below:

1. General features of cavitation dynamics observed using high speed video and X-ray densitometry
2. Experimentally measured void fraction flow fields: Averaged and *R.M.S*
3. Effect of inlet speed on the void fraction flow fields
4. Void fraction distribution at locations along the cavity length for different speeds
5. Periodicity measures for intermittent and shedding cavities based on dynamic pressure measurements and void fraction time history

Based on the observations and discussions, flow features that are prominent in transitory and

shedding cavities will be identified for further study.

6.1 Three Cavity Types

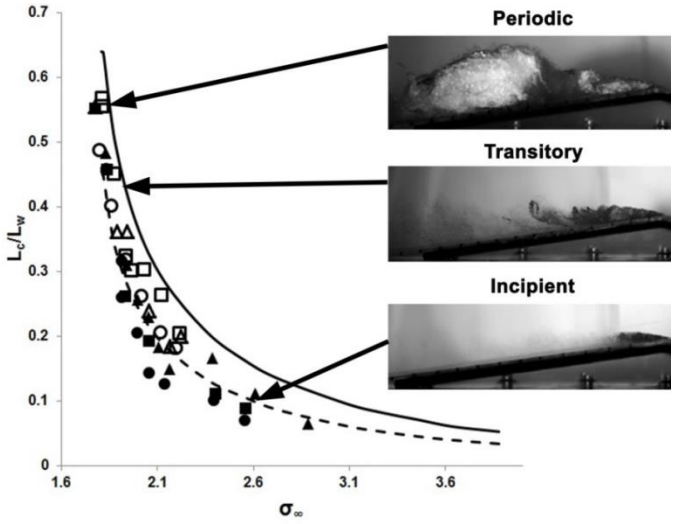

Figure 6.1: Three types of cavity chosen for further studies

Figure 6.1 shows the conditions chosen for further study. For all three cavity types the effect of free stream speed at a given cavitation number was studied. The cavities were first observed with high speed cinematography using two Phantom cameras that recorded the cavity dynamics from top and side views. The cameras were triggered using a TTL pulse generated by a Stanford delay generator. The top and the side view cameras were time synchronised to a common time base using Phantom Cine control software. The videos from top and side views were then combined using image combining algorithms in Matlab. It should be noted that the focal length of the top view camera was 35 mm while that of the side view camera was 105 mm. This mismatch was mainly due to the space constraints in mounting the camera from the top view. The top view videos were then scaled in Matlab to match the side views. Time resolved X-ray densitometry measurements of these three cavities was also conducted. For some cases, the X-ray

measurements were also accompanied by time synchronized surface pressure measurements using a PCB 138M101transducer. The X-ray videos were filmed at a rate of 1000 frames per second for a duration of 0.787 seconds. The images were then averaged to produce the averaged void fraction $\langle\alpha\rangle$, defined in Equation 5.1. The root of the mean of the squared, *R.M.S* of the difference between the calculated mean and the instantaneous void fraction value is also calculated to estimate the fluctuations in void fraction α', as expressed in Equation 5.4.

6.2. Incipient Cavity

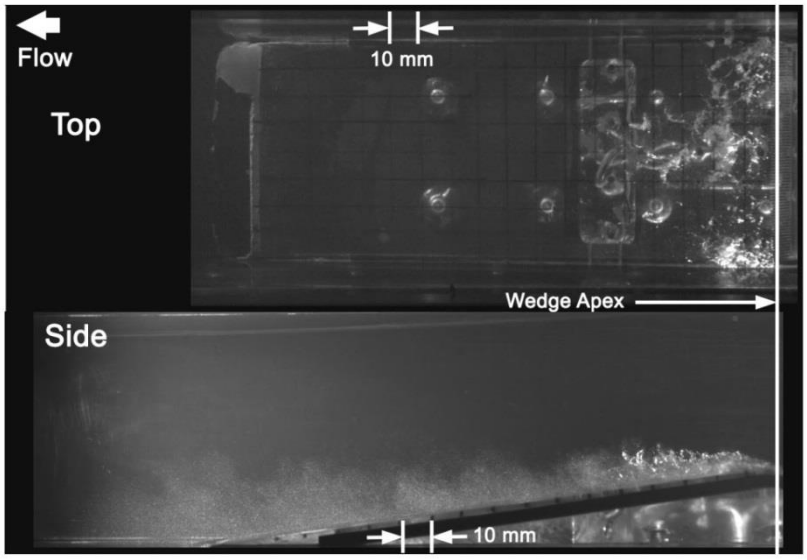

Figure 6.2: Incipient cavity at an inlet cavitation number of σ_0 = 2.46 and flow speed of U_0 = 8 m/s. Top and side views are time synchronised.

Figure 6.2 shows a still picture from a high-speed video of the incipient cavity taken from top and side views. In addition to the high speed video, X-ray densitometry based void fraction measurements of the incipient cavity were also conducted. Averaged and *R.M.S* of the difference from the mean of void fraction flow fields are shown in Figure 6.3 and 6.4. In addition to field

measurements, void fraction profiles in the wall normal direction (*n*) of the wedge at different locations along the wedge length as shown in Figure 6.5 were obtained. Figures 6.6 and 6.7 show the obtained averaged and *R.M.S* of the void fraction flow field.

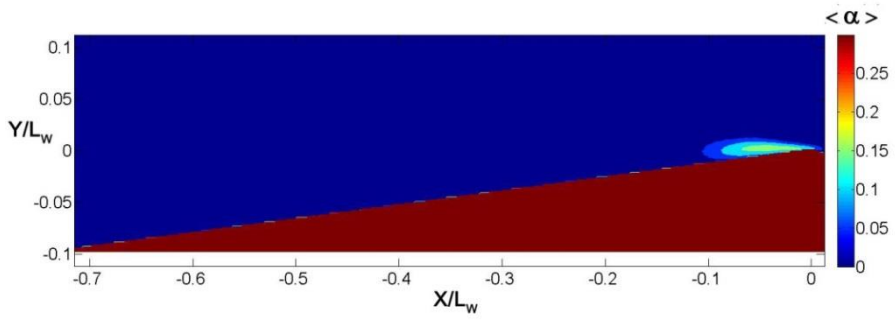

Figure 6.3: Averaged void fraction flow field of an incipient cavity at an inlet cavitation number of σ_0 *= 2.41 and flow speed of* U_0 *= 8 m/s.*

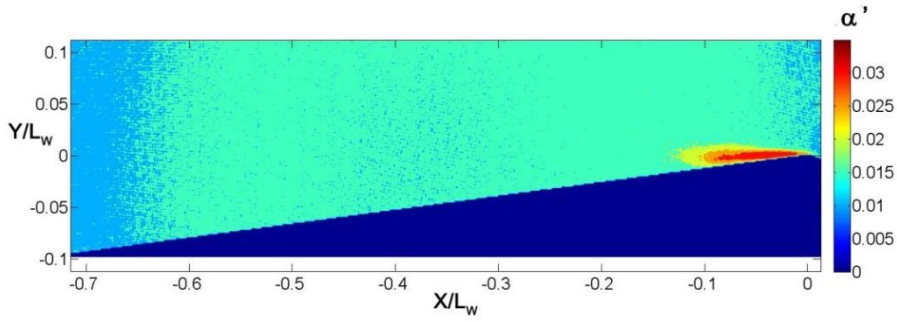

Figure 6.4: R. M. S void fraction flow field of incipient cavity at an inlet cavitation number of σ_0 *= 2.41 and flow speed of* U_0 *= 8 m/s.*

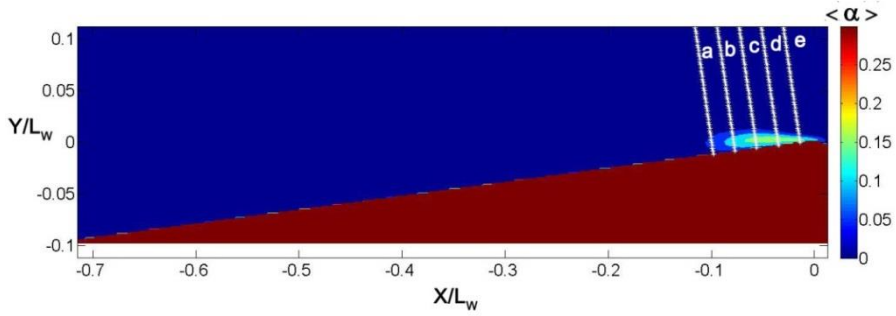

Figure 6.5: Locations of section view of void fraction profiles.

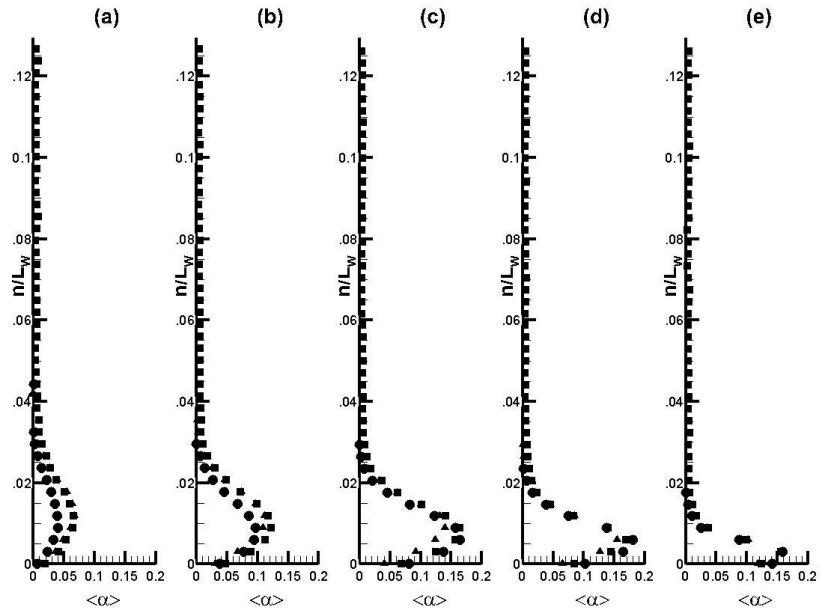

(a)

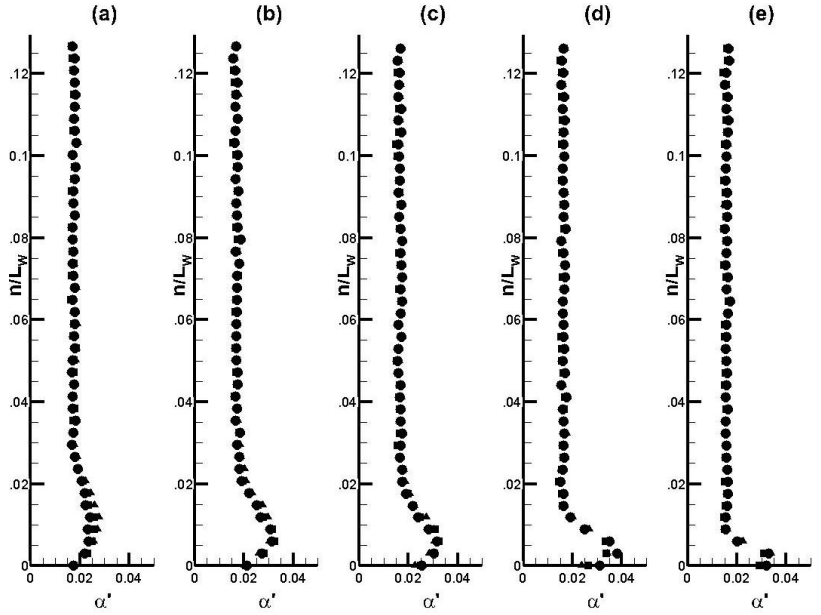

(b)

Figure 6.6: Averaged (a) and R.M.S (b) void fraction profiles for incipient cavities at locations a through e displayed in Figure 6.5. ▲- 6 m/s, ■ – 8 m/s, ●- 10 m/s.at $\sigma_0 = 2.41$

6.3. Transitory Cavity

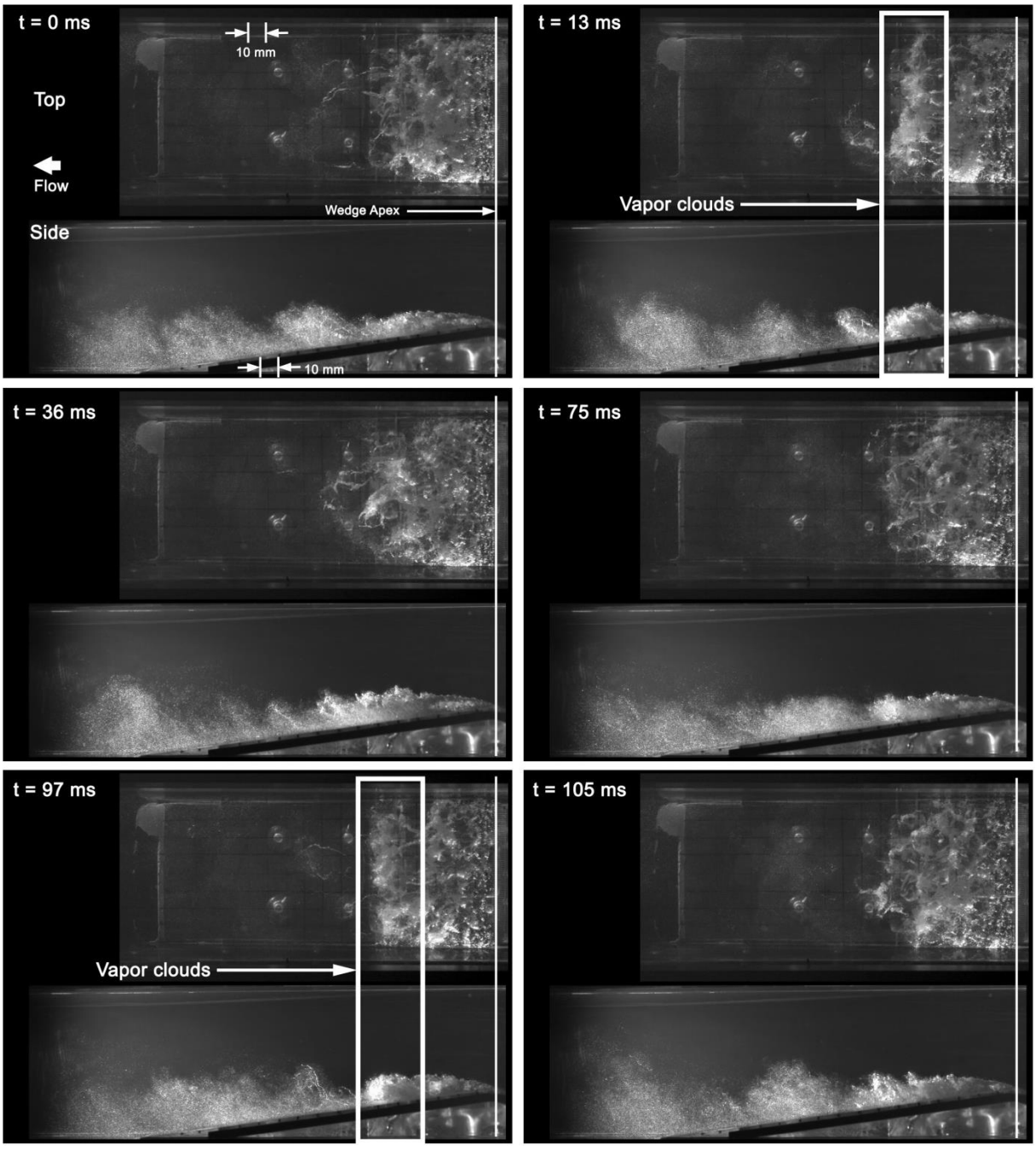

Figure 6.7: Transitory cavity at an inlet cavitation number of $\sigma_0 = 2.06$ *and flow speed of* $U_0 = 8$ *m/s. Top and side views are time synchronised.*

The transitory cavity shown in Figure 6.7 corresponds to a cavitation number of σ_0 = 2.06. With a further reduction in cavitation number, an incipient cavity of stable length began to show oscillations of length on the aft side of the cavity. These cavities also shed intermittent clouds of vapour. This behaviour began at a cavitation number of around 2.08. A time series of a transitory cavity that exhibits occasional shedding of vapour clouds in shown in Figure 6.7. The free-stream speed for this case was 8 m/s.

X-ray densitometry measurements of transitory cavities revealed further details about the flow mechanisms that are not easily visible in high-speed videos. Figure 6.8 shows a time series of instantaneous X-ray void fraction flow fields of a transitory cavity. It can be clearly seen that there is no regular periodicity of shedding. From the time-series two types of mechanisms of cavity shedding can also be seen. One corresponds to a re-circulating vapour cloud that is shed from the aft portion of the cavity. This was also observed in the high-speed video. From the flow field corresponding to *2 ms* and *5 ms* one can infer the presence of flow structure that scoops the aft portion of the cavity to facilitate shedding

Another type of mechanism corresponding to a propagating discontinuity can also be seen in the X-ray time series. This flow structure is different from the re-circulating flow and is similar to the re-entrant jet mentioned in the previous paragraph. The propagating discontinuity in void fraction, representing condensation shocks, travels upstream to cause leading edge pinch-off and shedding. When this mechanism is dominant the cavity growth and collapse can be easily identified when compared with the re-entrant mechanism.

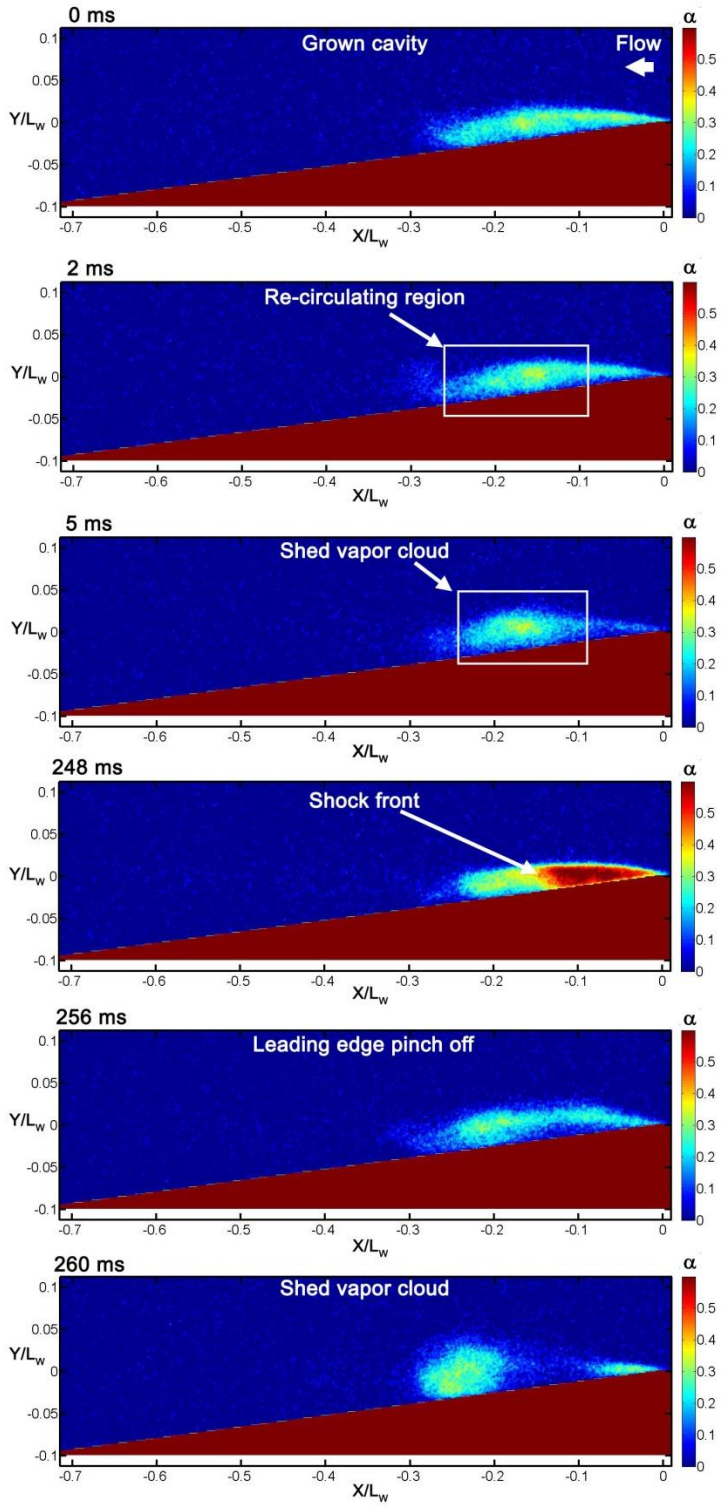

Figure 6.8: Instantaneous void fraction flow field of a transitory cavity at a free-stream cavitation number of $\sigma_0 = 2.06$ and flow speed of $U_0 = 8$ m/s.

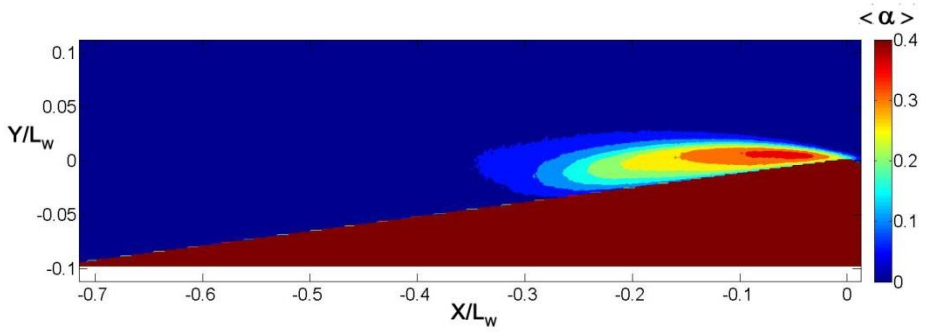

Figure 6.9: Averaged void fraction flow field of a transitory cavity at a free-stream cavitation number of $\sigma_0 = 2.06$ *and flow speed of* $U_0 = 8$ *m/s.*

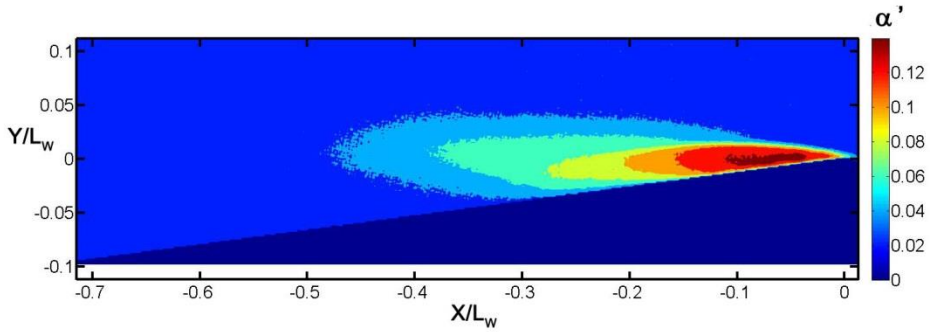

Figure 6.10: R. M. S void fraction flow field of a transitory cavity at a free-stream cavitation number of $\sigma_0 = 2.06$ *and flow speed of* $U_0 = 8$ *m/s.*

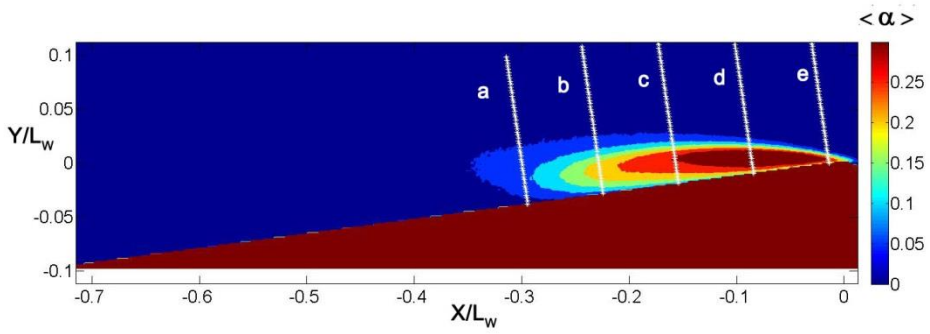

Figure 6.11: Locations of section view of void fraction profiles, a-e for comparison with different flow speeds.

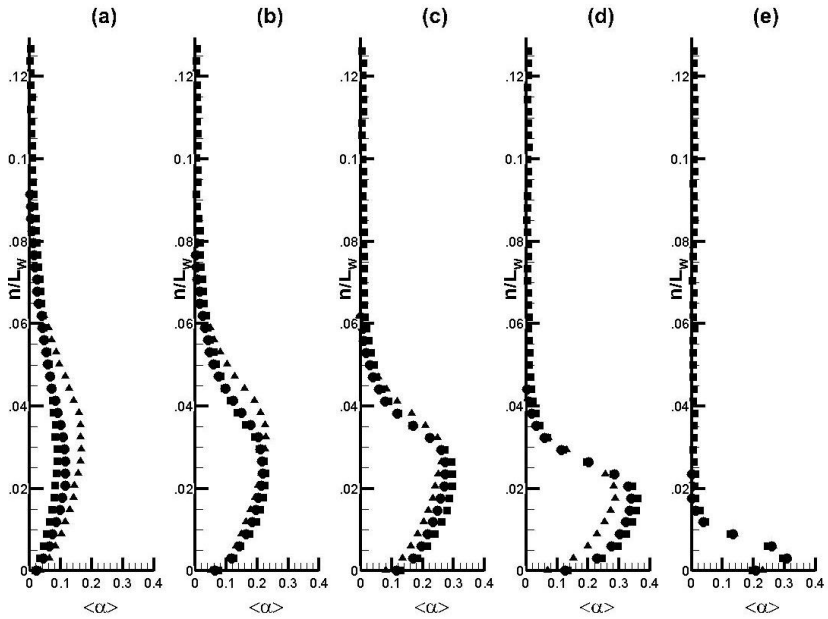

(a)

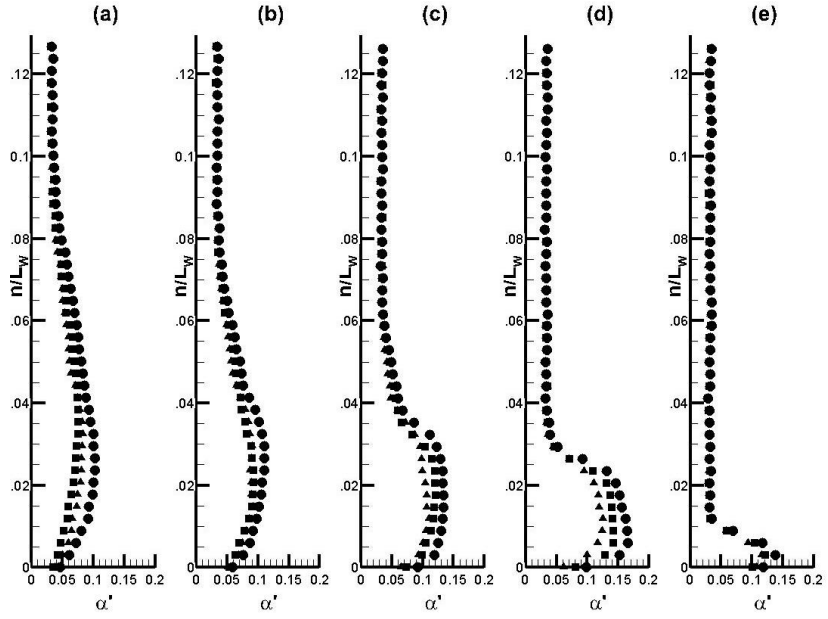

(b)

Figure 6.12: Averaged (a) and R.M.S (b) void fraction profiles for a transitory cavity at locations a through e displayed in Figure 6.10. ▲- 6 m/s, ■ – 8 m/s, ●- 10 m/s. at σ_0 = 2.06

Averaged $<\alpha>$ and *R.M.S* α' of the difference from the mean of void fraction flow fields are shown in Figures 6.9, 6.10 and 6.11. The averaged void fraction contour has spread in the aft portion of the cavity. This is a consequence of averaging including the shed cycles and other cavity break up mechanisms that occur near the cavity closure. The *R.M.S* flow field in Figure 6.9 also has higher values of void fraction fluctuation in the regions outside the actual cavity for the same reason.

In addition to field measurements, void fraction profiles in the wall normal direction at different locations along the wedge length, as shown in Figure 6.11, were obtained. Figure 6.12 (a) and (b) show averaged and *R.M.S* of the void fraction flow field at the locations mentioned in Figure 6.11. It should be noted that for different speeds such as 8 m/s and 10 m/s, the cavity chosen for comparison was slightly larger in length compared with 6 m/s. This explains part of the observed lower value of averaged void fraction for the case of 6 m/s. For the transient cavity, the free stream speed does not exhibit a dominant effect on the average and *R.M.S* profiles.

6.4. Periodic Cavity

Figure 6.13 shows the time series from a high speed video of a periodically shedding cavity at a free stream cavitation number of σ_0 = 1.95. The cavity exhibits well defined growth and collapse cycles. The cavity has a distinct leading edge pinch off and a complete maximum growth phase. Shedding is produced by leading edge pinch off of the cavity and the shed vapour clouds are convected downstream with the cloud collapsing within the camera viewing area. For slightly higher cavitation numbers than σ_0 = 1.95, X-ray measurements reveal that for a periodically shedding cavity, only one of the two mechanisms of vapour shedding, mainly the propagation condensation shock front is observed. The shock front is well defined for most of the cycles for a

given cavitation. For some cycles the shock front is smeared and this could be due to cavity variations in the span wise direction.

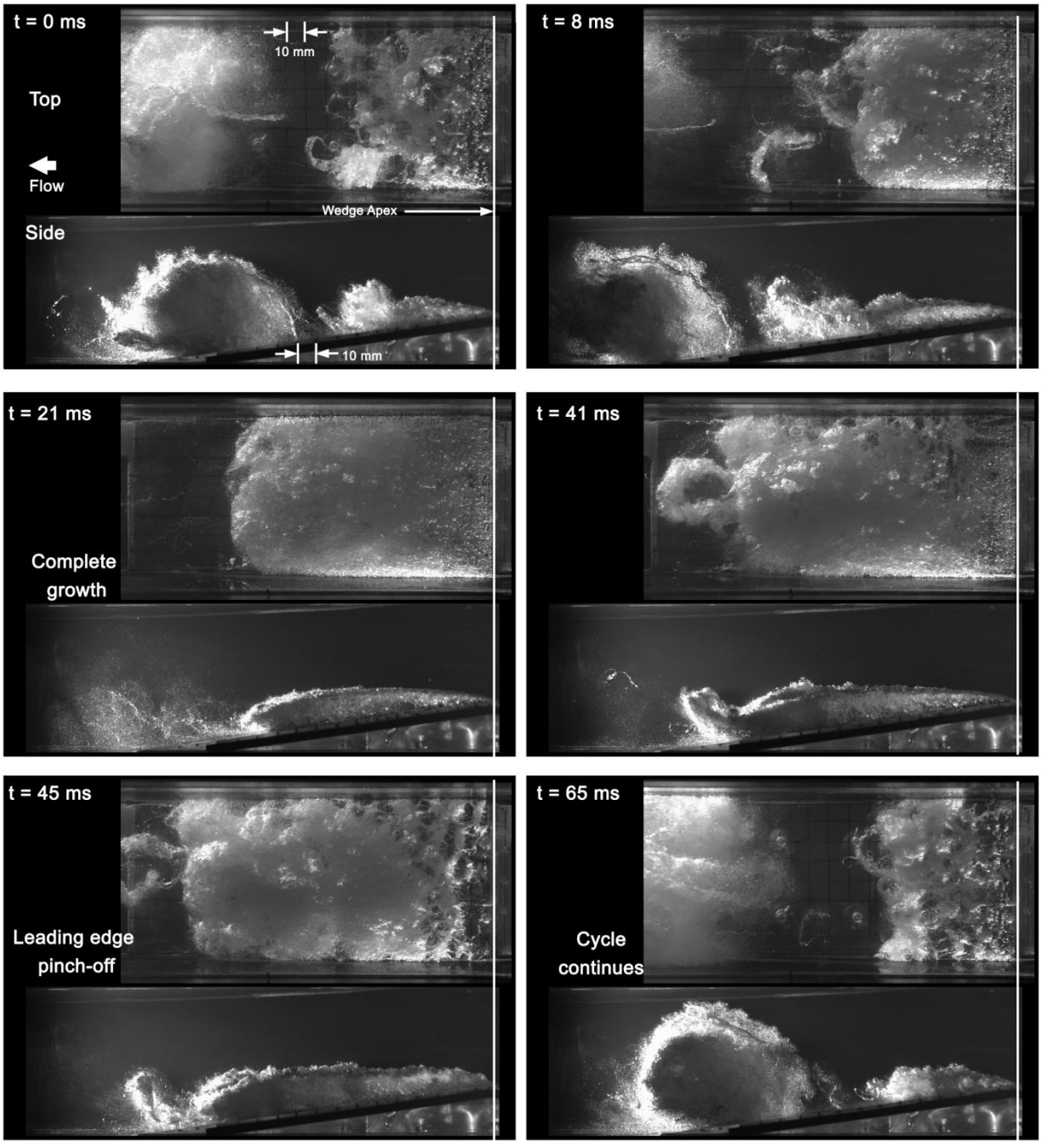

Figure 6.13: Periodically shedding cavity at an inlet cavitation number of σ_0 = 1.95 and flow speed of U_0 = 8 m/s. Top and side views are time synchronised.

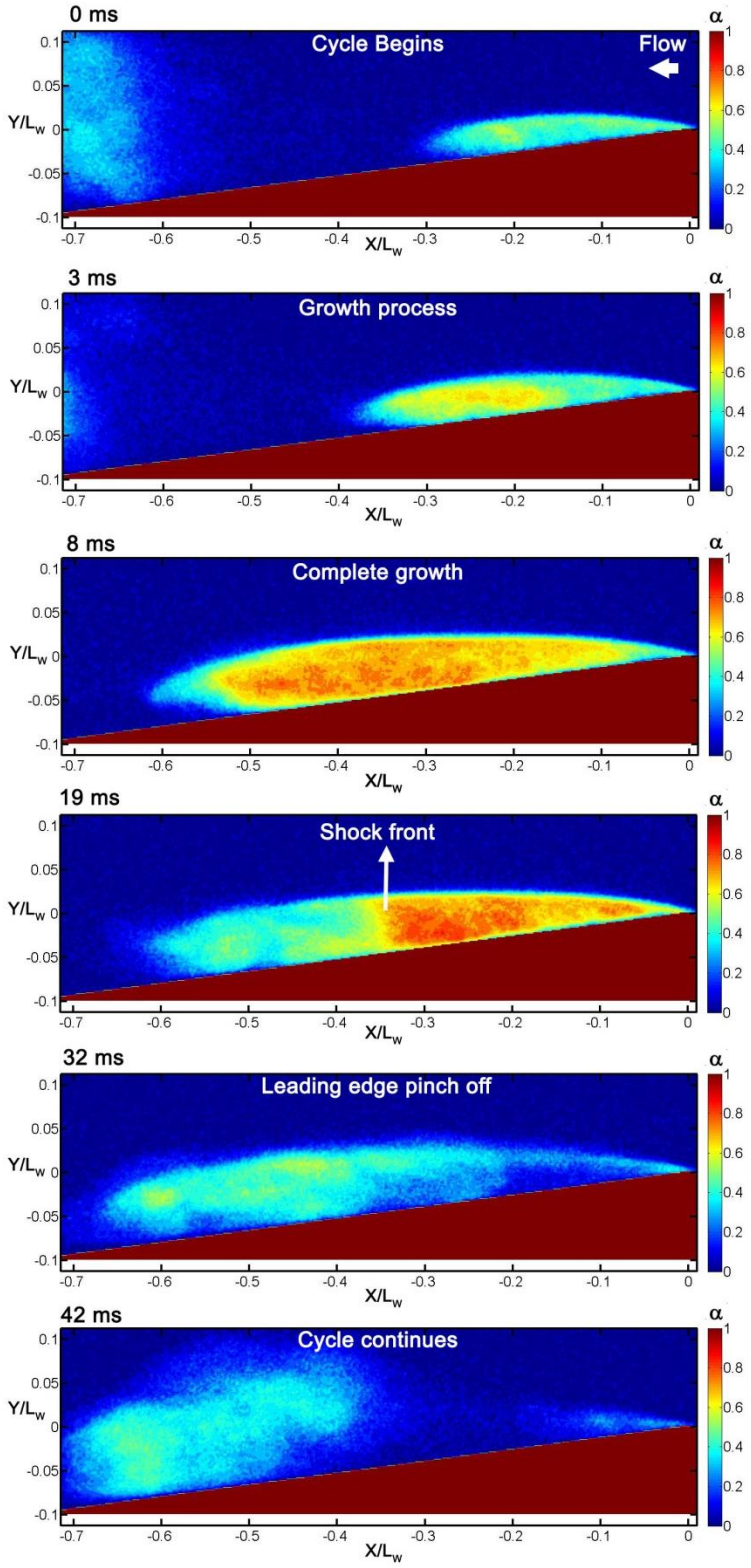

Figure 6.14: Instantaneous void fraction flow field of a periodic cavity at an inlet cavitation number of σ_0 = 1.95 and flow speed of U_0 = 8 m/s

Averaged and *R.M.S* void fraction fields for the periodic cavity are shown in Figure 6.15 and 6.16 respectively. Average and *R.M.S* section profiles are shown in Figure 6.18 (a) and (b) at locations shown in Figure 6.17.

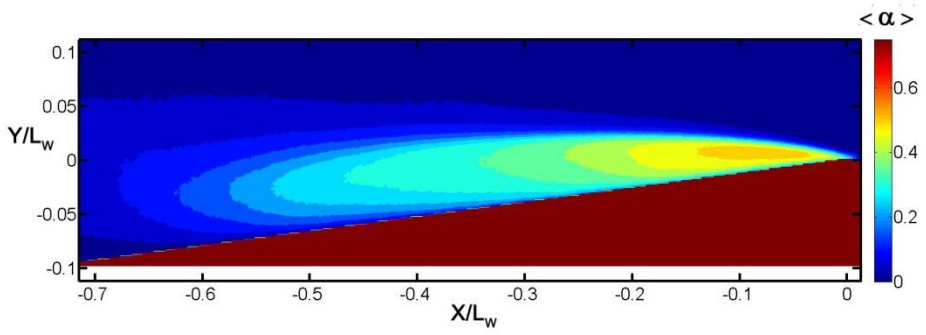

Figure 6.15: Averaged void fraction flow field of a periodic cavity at a free-stream cavitation number of σ_0 = 1.95 and flow speed of U_0 = 8 m/s.

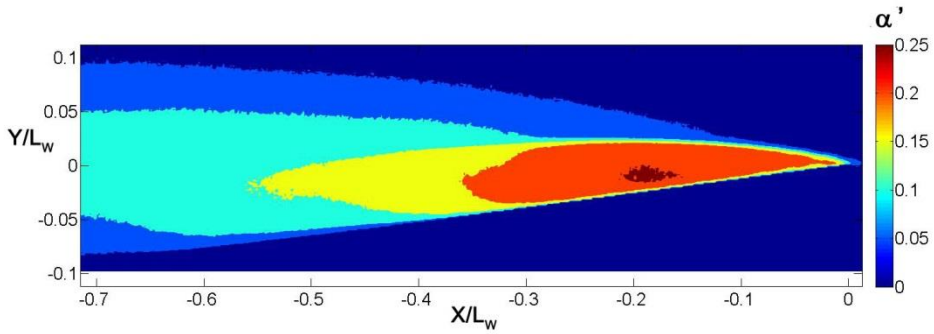

Figure 6.16: R. M. S void fraction flow field of a transitory cavity at a free-stream cavitation number of σ_0 = 1.95 and flow speed of U_0 = 8 m/s.

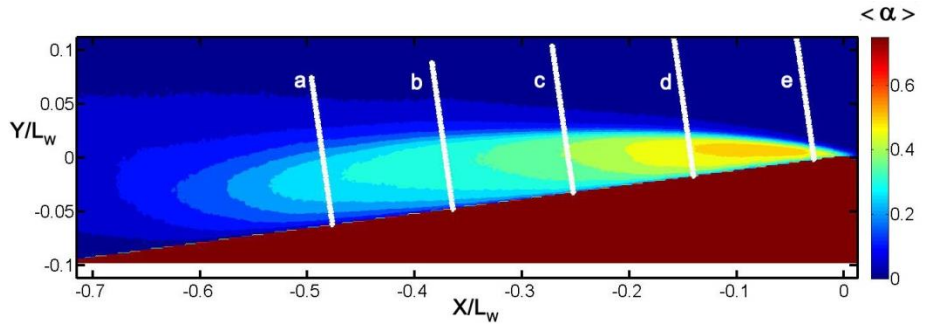

Figure 6.17: Locations of section view of void fraction profiles, a-e for comparison.

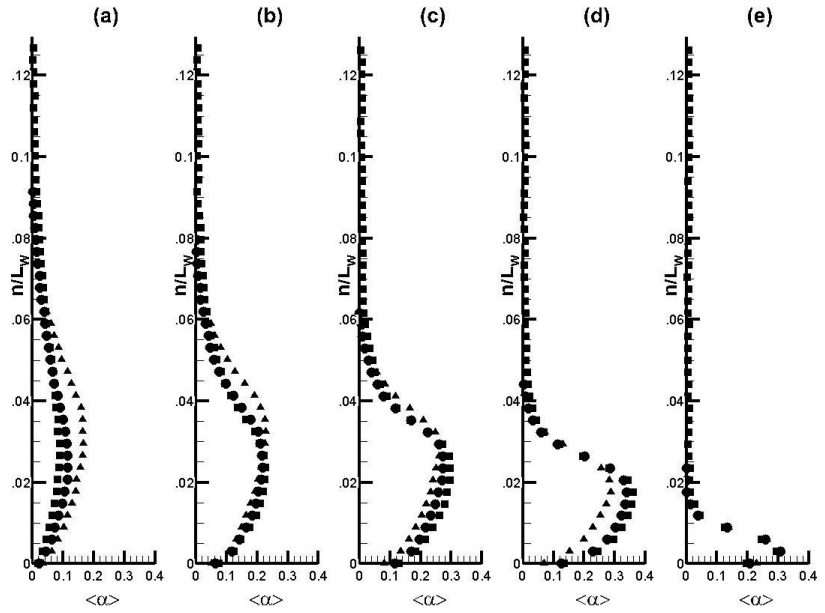

(a)

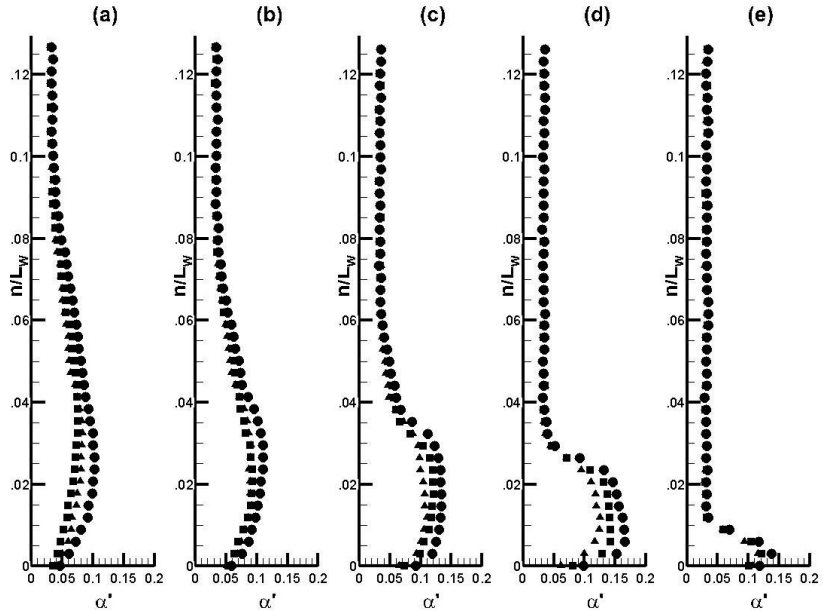

(b)

Figure 6.18: Averaged (a) and R.M.S (b) void fraction profiles for a periodic cavity at locations a through e displayed in Figure 6.10. ▲- 6 m/s, ■ – 8 m/s, ●- 10 m/s. for σ_0 = 1.95

6.5 Maximum Averaged Void Fraction

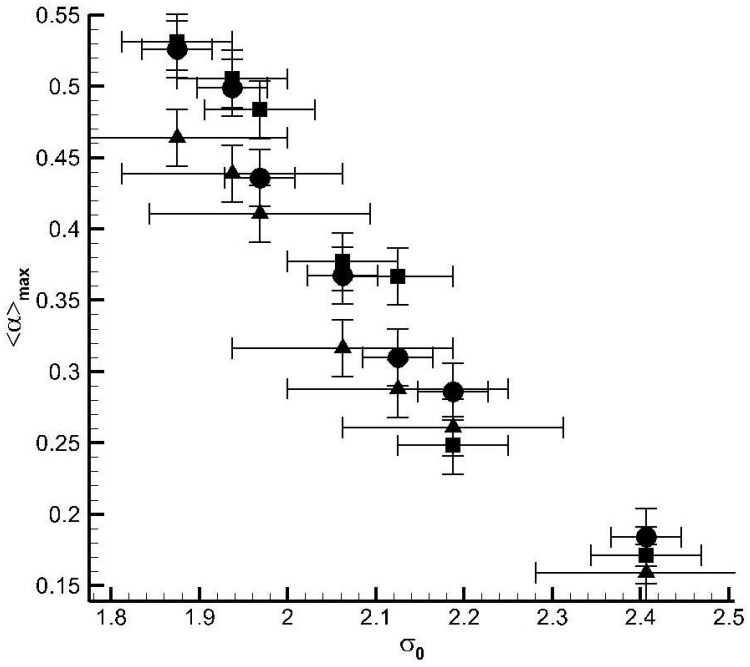

Figure 6.19: Maximum averaged void fraction at different cavitation numbers. ▲*- 6 m/s,* ■ *– 8 m/s,* ●*- 10 m/s*

The effect of free stream speed on the maxium averaged void fraction for a given cavitation number is shown in Figure 6.19. There is not appreciable difference due to variation in flow speed.

6.6 Shedding Frequency and Strouhal Number

Unsteadiness observed in the cavitation was quantized by measuring the time variation flow properties such as void fraction and cavity pressure. The location of void fraction and surface pressure probes are shown in Figure 6.20. Time stamp of void fraction variation at the location mentioned was obtained from the X-ray videos as shown in Figure 6.21 (a). Variation of surface pressure from a high frequency response transducer was recorded using a high sampling rate data

acquisition system and sample signal is shown in Figure 6.21 (b). These measurements enabled us to calculate the flow unsteadiness frequency and hence the Strouhal number.

Characteristic frequency of variation was obtained by taking the Fast Fourier transform (FFT) of void fraction and surface pressure signals. From the FFT frequencies corresponding to maximum Fourier domain amplitude were identified as dominant frequencies. Figure 6.21 (c) and (d) show FFT of a void fraction and pressure signal normalized by the maximum Fourier magnitude respectively. Both FFT signals show the presence of dominant frequencies at around 20 Hz, with smaller peaks or harmonics at 40 Hz and 60 Hz, consistent with the observed physics of vapour production and shedding.

The variation of dominant frequency with cavitation number for different speeds is shown in Figure 6.22. Filled symbols correspond to the frequency obtained from the void fraction signal while the unfilled symbols correspond to the pressure signal. At higher cavitation number, void fraction variation frequency and the pressure variation frequency does not match, suggesting no relation between vapour production and pressure fluctuations. With the reduction in cavitation number, both the void fraction signal and the pressure signal give rise to the same frequency which corresponds to cavity filling and shedding cycle. In this case the flow is in the regime where the changes to pressure within the cavity also drive the vapour production, which is characteristic of periodic shedding. Figure 6.23 shows the variation of Strouhal number with cavitation number. The Strouhal number (St) is defined as,

$$St = \frac{FL_{Cav}}{U_0} \tag{6.1}$$

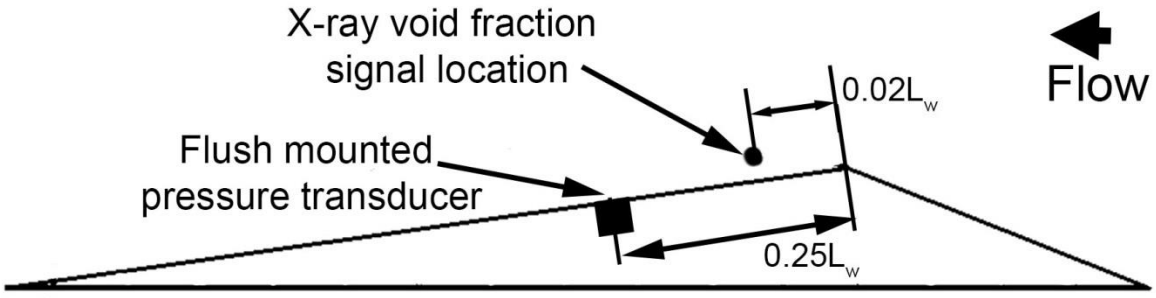

Figure 6.20: Location of flush mounted pressure transducer and void fraction probe for cavity transience study

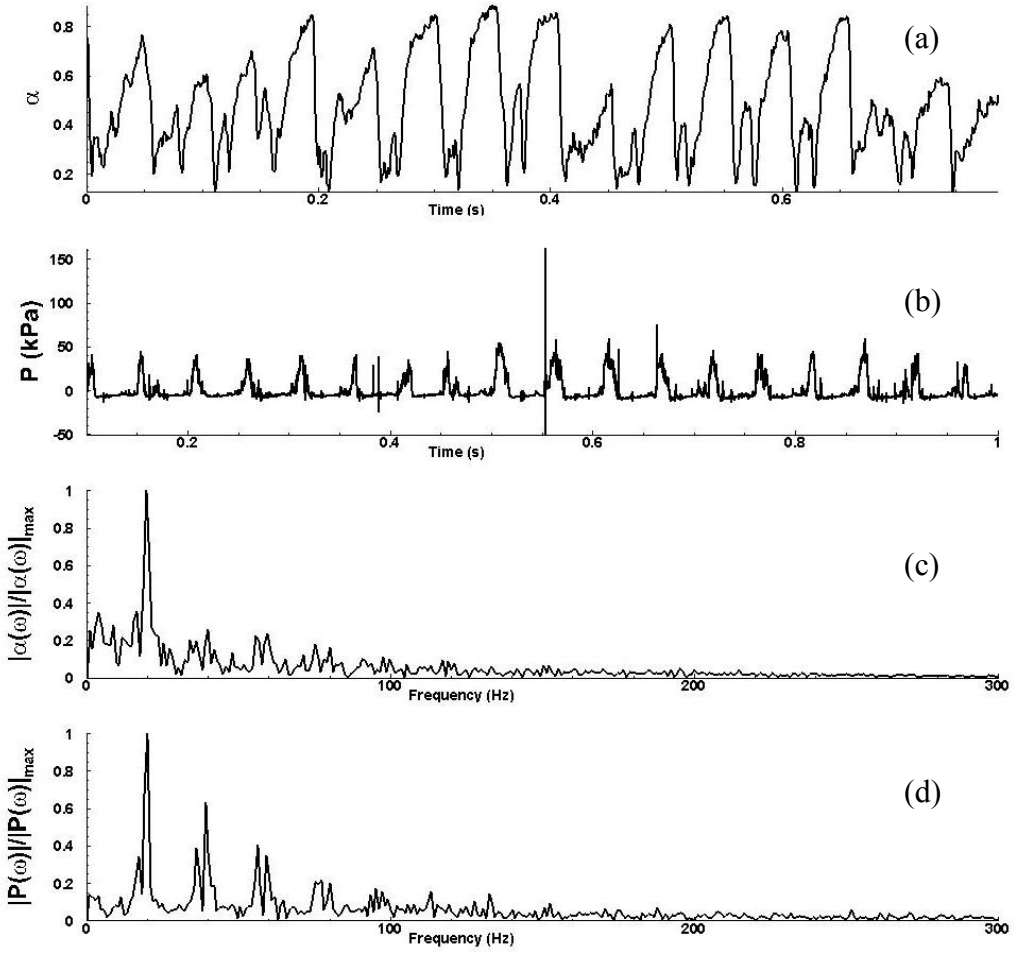

Figure 6.21: (a) typical void fraction probe signal (b) pressure transducer signal (c) FFT of signal in 6.21 (a) normalized by maximum Fourier space magnitude (d) FFT of signal in 6.21 (b) normalized by maximum Fourier space magnitude

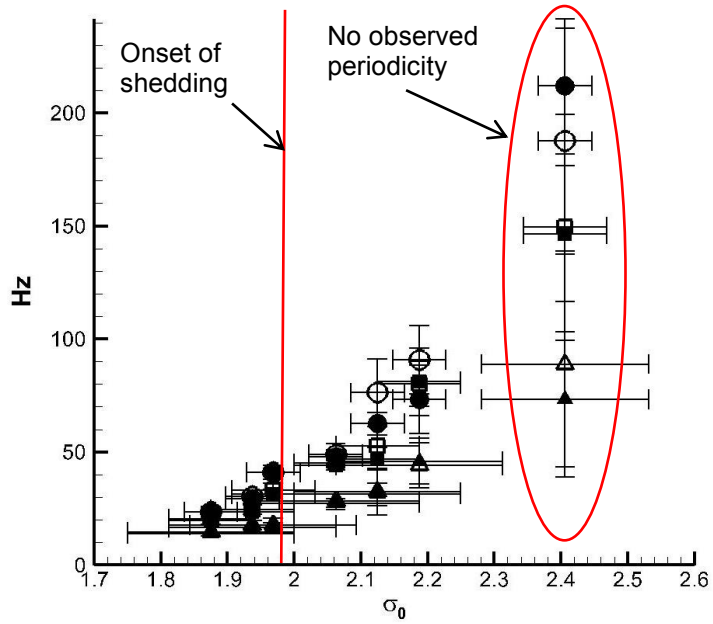

Figure 6.22: Variation of shedding frequency with cavitation number for ▲- 6 m/s, ■ – 8 m/s, ●- 10 m/s (void fraction signal), Δ-6 m/s , □-8 m/s, ○-10 m/s (Pressure signal)

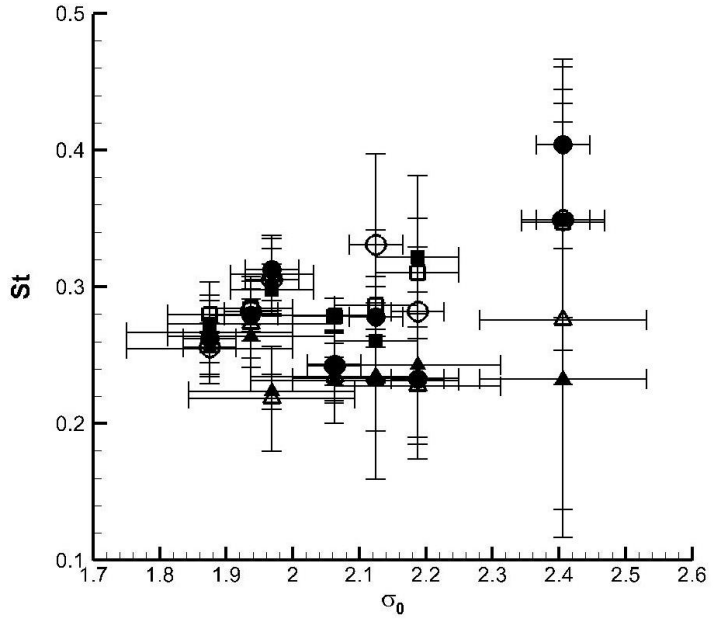

Figure 6.23: Variation of Strouhal number with cavitation number for ▲- 6 m/s, ■ – 8 m/s, ●- 10 m/s (void fraction signal), Δ-6 m/s , □-8 m/s, ○-10 m/s (Pressure signal)

In this case, F represents the frequency of shedding, L_{Cav}, represents the length scale that depends on the cavity geometry. For the case the case non shedding cavities L_{Cav} was taken as the maximum cavity length from averaged images. For periodically shedding cavities, L_{Cav} was the value close to the maximum length the cavity attained in the shedding cycle before eventually collapsing and shedding. Figure 6.23 shows that the Strouhal number remains the around the value of 0.25-0.30 for all shedding cavities irrespective of the cavitation number. This value and trend is consistent with other findings regarding Strouhal number for shedding cavities for similar geometries.

6.7 Chapter Summary

1. Three types of cavities: incipient, transitory, and periodically shedding cavities were chosen for further exploration of cavitation dynamics and associated flow features.
2 Incipient cavities are stable possessing no oscillation in cavity length. With a further reduction in cavitation number, transitory cavitation begins with intermittent shedding. With a further reduction in cavitation number periodic shedding occurs
3 The free stream speed does not seem to have a dominant effect on the averaged void fraction flow fields and shedding dynamics.
4 Based on X-ray densitometry measurements, it was found that for the case of transitory cavity two mechanisms of *re-circulating flow induced shedding and shock wave induced shedding* exist. For the case of periodically shedding cavities, condensation shock wave induced shedding is the most dominant mechanism.
5 Maximum averaged void fraction increases with decrease in cavitation number. Inlet speed does not have dominant effect on the observed values.

6 The frequency analysis based on void fraction and pressure signals reveal the same *St* number confirming the role of pressure change to vapour production.

7 Frequency domain analysis of measured time varying quantities suggests that the dynamics of the present cavity are consistent with those previously reported in literature. The next chapter deals with the two mechanisms of cavity shedding observed so far.

CHAPTER 7

Cavity Shedding Mechanisms

Shedding of vapour clouds occurs when cavities grow beyond a certain length. Sometimes a part of the rear portion of the cavity is shed periodically while leading edge pinch-off of a fully grown cavity has also been observed. It should be noted the reason a stable cavity begins to shed is due to a decrease in cavitation number which triggers an increase in length that cannot be sustained. This suggests the presence of length and time scales of flow processes that become important when a cavity grows beyond a certain length, resulting in shedding. To understand the interplay between the processes, the length and time scales are required to predict the onset of periodic shedding of vapour clouds.

In the previous chapter, mainly for the case of a transitory cavity, two types of mechanism were observed. One was a re-circulating flow at the aft portion of the cavity that caused the pinch off of vapour clouds. This mechanism was intermittent when compared to the prominent mechanism of propagating void fraction discontinuities that resulted in leading edge shedding of vapour clouds. As mentioned in Chapter 2, these cavity flows can have high values of instantaneous void fraction which can result in reduced speed of sound. Since void fraction at any given instant of time depends upon the cavity growth rate, one of the processes that is expected to play an important role in shedding is the vapour production rate. The role of re-entrant flow in causing

periodic shedding has been studied well in the past. There have been many proofs for the existence of the re-entrant flows and their role in causing periodic shedding. However, shock wave induced shedding of vapour clouds has not been reported before. Thus it is imperative that the observed mechanisms be explored in a detailed manner. The present chapter explores the mechanisms in the following manner.

1. The flow field of the present study is compared with two previous studies reported in literature to look for similarities and differences in mechanisms reported before.
2. One study chosen, Stutz and Reboud (1997 a), involves measurement of vapour phase velocity inside a shedding cavity which reported the presence of any reversed flow regions. Void fraction flow fields from the present study will be compared with those reported in Stutz and Reboud (1997 a).
3. The second study chosen for comparison is a qualitative study which proved the importance of re-entrant flow by placing a solid obstacle along its path. This comparison will shed more light into the nature of the mechanisms observed in the present study.
4. Finally the properties of the shock waves responsible for periodic shedding of vapour clouds are analysed.

7.1 Two Observed Mechanisms

As mentioned in previous chapter, a stable incipient cavity begins to exhibit intermittent shedding when the cavitation number is reduced. For the case of a transitory cavity it was observed that the vapour clouds were shed by the break-up of the cavity by the presence of a re-circulating flow. This mechanism is different from a propagating shock wave which reduces the gas content of the cavity drastically before being shed from the leading edge. Figure 7.1 shows

both these mechanism observed in a transitory cavity. In the case of a periodically shedding cavity, the presence of a propagating condensation shockwave into the cavity has been identified as the dominant mechanism. Many studies in the past on the shedding of vapour clouds from hydrofoils and wedges have reported a presence of a re-entrant liquid jet propagating into the cavity as the mechanism of shedding. The results of a few of these studies will be compared to the observations in the present study.

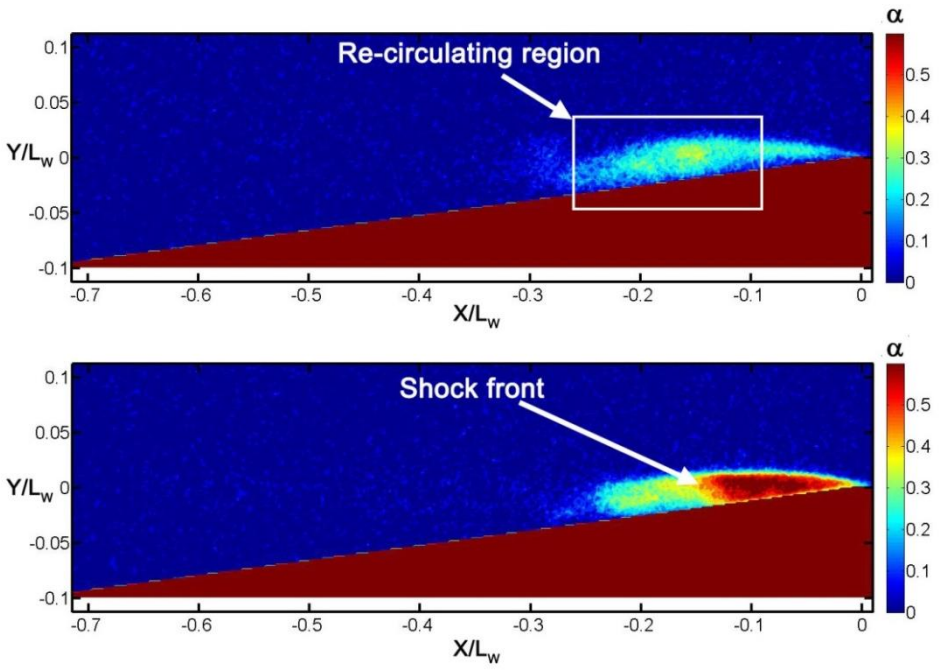

Figure 7.1: Two mechanism of cloud shedding on a wedge

7.2 Comparison With a Reported Study Using an Optical Probe

One of the studies on a similar geometry as the wedge reported the presence of a re-entrant jet by measuring the averaged vapour flow velocity and void fraction using double optical probes was done by Stutz (1998). In a series of similar yet different papers the authors report the type of the cavity dynamics and associated void fraction flow field measurements that were obtained

using double optical probes. In another study, the authors also use X-ray densitometry to measure void fraction along a line of detectors.

The experimental measurement setup of the study consisted of using optical probes that are capable of detecting vapour in a liquid flow. Presence of two such probes separated by a constant distance of 2.02 +0.02 mm facilitated the measurement of the gas phase velocity by correlation between the two optical probe signals. The probe signals were sampled at the rate of 67.5 kHz. Using this set up, the authors measured phase averaged void fraction and gas phase velocity profiles. This measurement is one of the few experimental measurements of gas phase velocities in the cavity that is available for geometry similar to the present study.

The presence of a reversed flow region in the phase averaged velocity fields is one of the key finding of this study. This corroborated the presence of a re-entrant or a re-circulating liquid fluid that flows into the cavity to cause shedding. Also, the cavity broke off in the aft portion with no observance of leading edge shedding. This suggests that the cavity reported in this study is similar to a transitory cavity of the present study, mainly when it experiences re-entrant based shedding.

The availability of time resolved void fraction flow fields from X-ray measurements facilitated the computation of a void fraction signal correlation between two points in the domain. However, as the sampling rate was not as high as the previous study by Stutz (1997 a), the exact vapour phase flow velocity could not be determined. Instead, the whole time trace of void fraction signal at two locations separated by a distance 4 mm were compared. Such comparison gives an averaged vapour flow direction in the cavity.

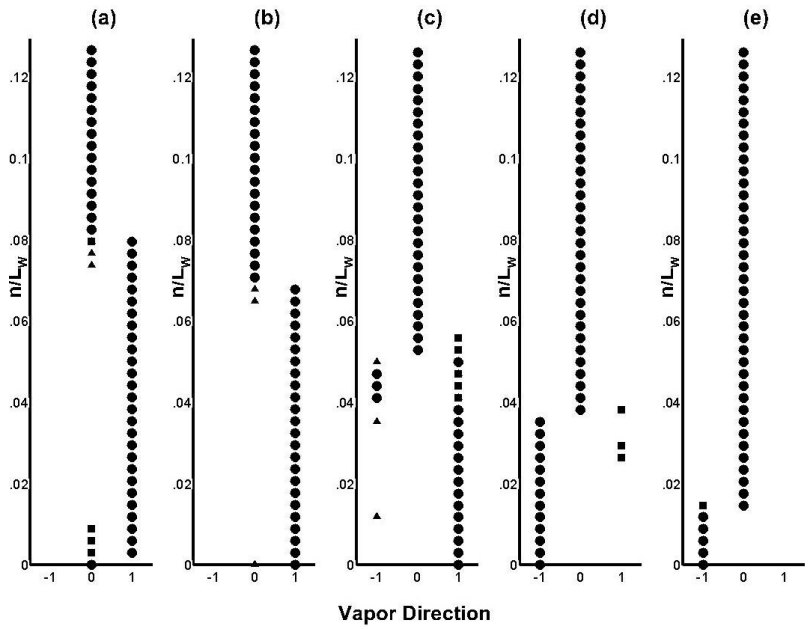

Figure 7.2: Averaged vapour flow direction for a transitory cavity. +1 indicates vapour flow in the flow direction and -1 against the flow direction for a Transitory cavity at σ_0 =2.06

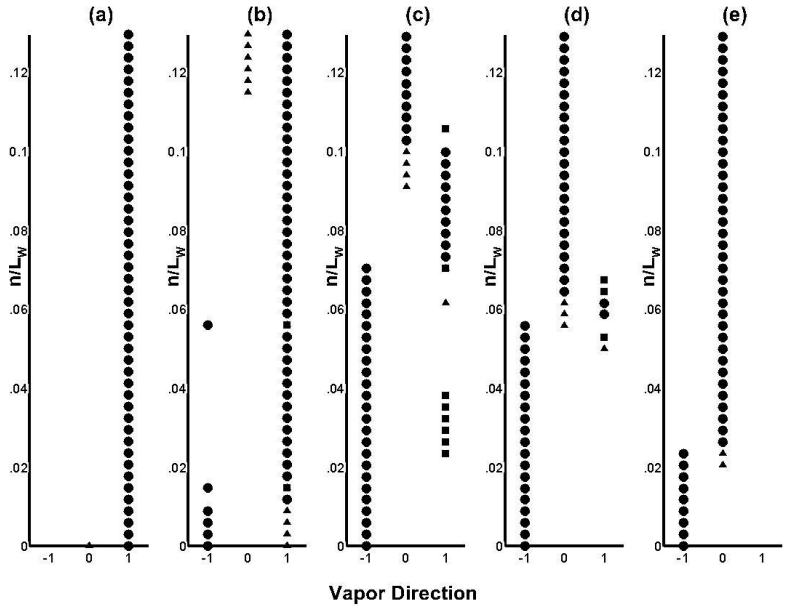

Figure 7.3: Averaged vapour flow direction for a periodic cavity. +1 indicates vapour flow in the flow direction and -1 against the flow direction for a periodic cavity at σ_0 =1.95

As the time sampling was only 1 kHz, the correlation function was interpolated to determine the maximum correlation value from which to estimate the actual time lag or lead. Depending on the sign of the occurrence of the maximum correlation peak, the averaged vapour flow directions set to +1 if it was in the direction of the flow, and -1 if it was in the opposite direction. Averaged vapour flow directions were determined along the same set of points where average and RMS void fraction profiles were reported in Chapter 6. These locations are shown in Figures 5.12 and 5.18 for transitory and periodically shedding cavities respectively. Figures 7.2 and 7.3 show the averaged vapour flow direction for a transitory and periodic cavity.

The average vapour flow directions represented in Figures 7.2 and 7.3 suggest that the determination of velocity from vapour flow could result in the presence of reversed flow within the cavity. The correlation function reaches zero at an ‘n’ co-ordinate that corresponds to a value close to the thickness of the cavity at a given section profile location. Such a region can be clearly seen in Figure 7.3 and 7.4, with the maximum thickness of the reversed region occurring near half the cavity length. It should be noted that this is an average vapour flow direction determined from the whole time signal. Nevertheless, it does suggest that the trend observed is similar to that based on the measurement principles of a double optical probe. It helps us infer the following conclusions:

1. Presence of reversed direction of vapour flow occurs even in the case of periodic shedding where the presence of a shock wave has been observed to cause the shedding.
2. The reversed flow regions obtained from a double optical probe could mean the presence of both a re-entrant flow and a condensation shock wave.

7.3 Presence of an Obstacle in the Cavity

The presence and the importance of a re-entrant jet in causing cloud shedding was also verified by Kawanami (1994) by placing an obstacle in the path of the re-entrant jet. From their study it was found that the presence of the obstacle hampered the propagation of the jet upstream to cause pinch off and hence shedding. The presence of an obstacle in the cavity of the present study should have an effect on the shedding dynamics if it is caused by a re-entrant phenomenon. The interaction of the shock wave with the obstacle will provide further insights about the mechanism.

Figure 7.4 shows the time series of a shedding cycle in the presence of an obstacle. The obstacle was placed at a distance of about $0.35\ L_W$ from the wedge apex in the negative s-direction. The obstacle has a square cross section with a width about 2 mm. The obstacle thickness was around 15% of the height of the shock wave when it crossed the obstacle. Figure 7.3 shows the time series of a shock wave induced shedding in the presence of an obstacle.

The presence of the obstacle does not affect the growth of cavity. At the beginning of the cycle, the cavity fills with vapour, growing longer in length and surpassing the location of the obstacle. This suggests that the alteration of flow time scales near the wedge wall due to the presence of the obstacle is sufficient when compared with the cavity growth rate. Having surpassed the obstacle the cavity continues to grow to achieve maximum length, then the shock process begins aft of the cavity. The bubbly shock jumps across the obstacle to reduce the vapour content in the cavity, and causes leading edge pinch-off of the shocked vapour. In the last frame the presence of a wake in the reversed flow direction behind the obstacle filled with vapour is also clearly visible.

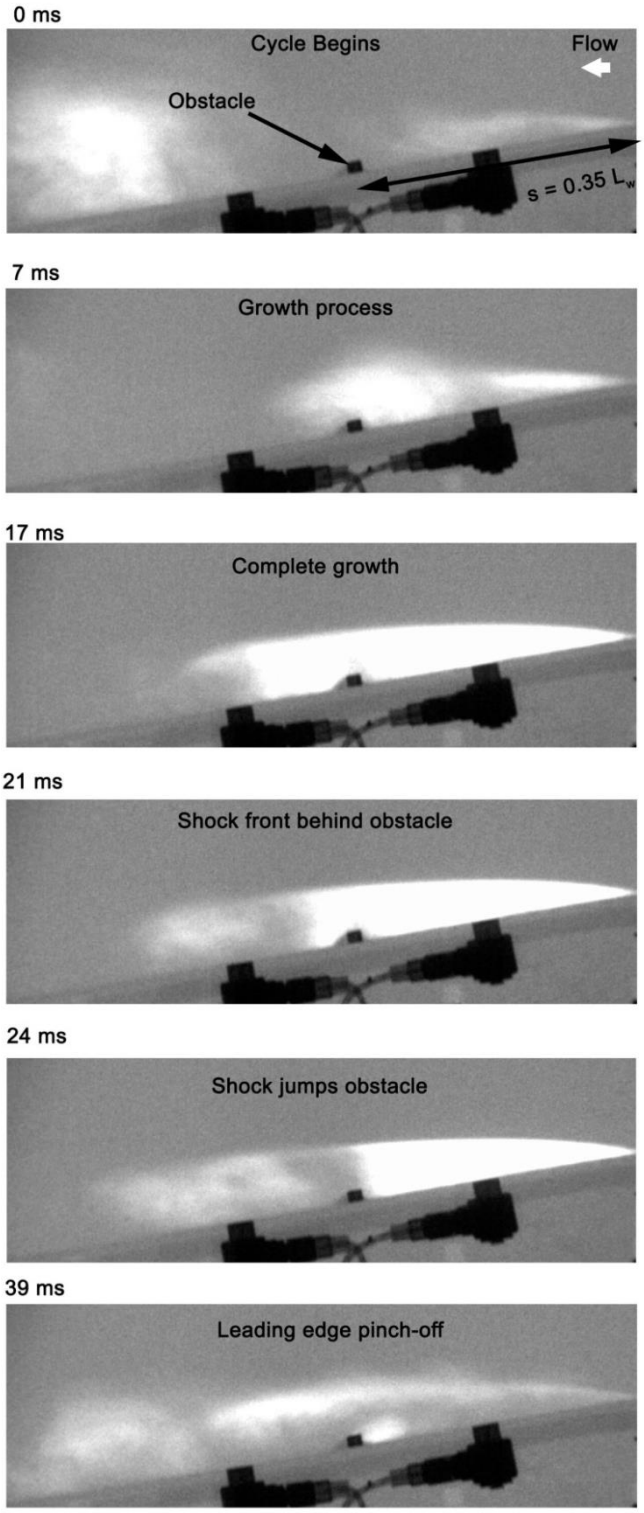

Figure 7.4: Shedding cycle in the presence of an obstacle

7.4 Proposed Mechanism

Primary differences in the shedding mechanisms can be summarised as:

1. Transition from aft shedding to leading edge shedding
2. Presence of a propagation discontinuity which can also be interpreted as thick liquid flow back into the cavity
3. Insensitivity of the shedding due to the propagating discontinuity to presence of obstacles.

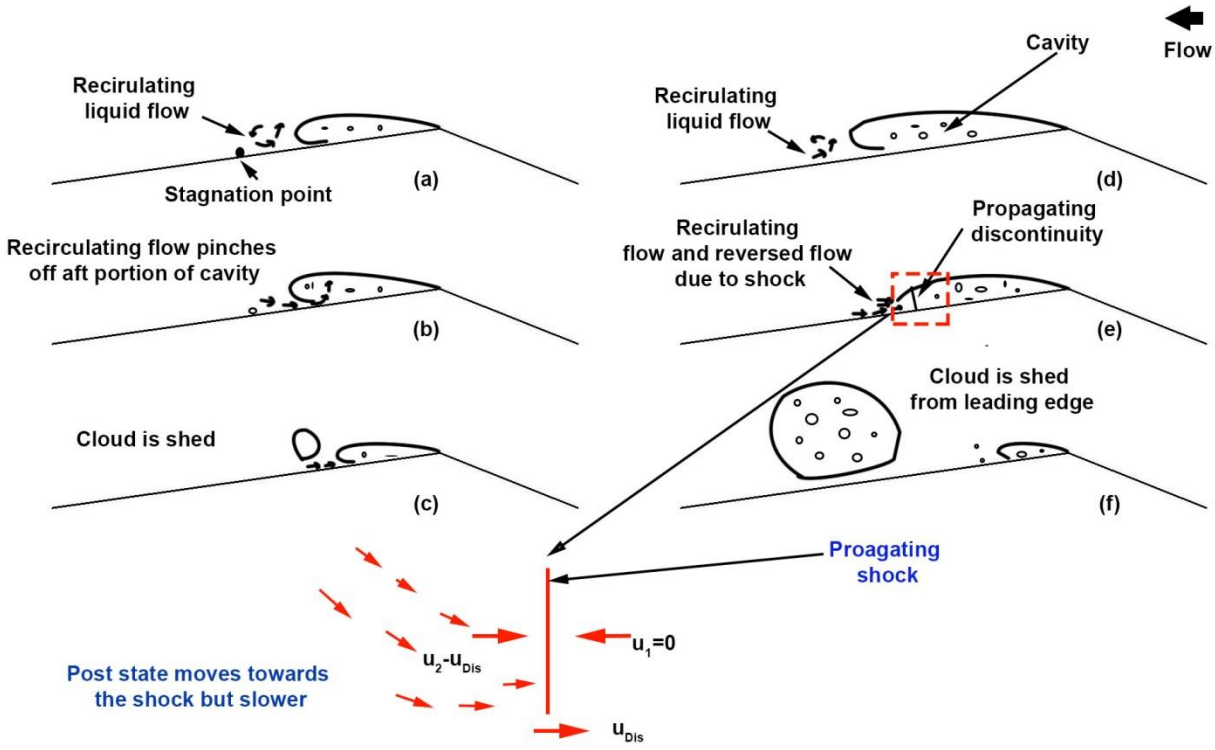

Figure 7.5: Two mechanism of shedding in detail

Figure 7.5 shows the schematic of different types of shedding. Figures 7.5 (a) – (c) represents a re-entrant flow mechanism. Such a mechanism is possible due to kinematics of a separated flow sustaining a constant pressure cavity. From Chapter 4, it is evident that presence of a re-entrant

flow is possible when there is a stagnation point at the aft of the cavity. In such a scenario, the liquid flowing into the cavity can produce a pinch off, and the thickness of the liquid flow is smaller than the cavity thickness. This is due to the virtue of the maximum turning that the interface streamline has to make to re-enter into the cavity. For the re-entrant flow to be as thick as the cavity itself, the interface streamline has to turn around 180 degrees with a radius of curvature of close to zero. This would result in low pressure which would be closer or smaller than the cavity pressure, thereby resulting in cavitation. Also, there has been no report on the presence of a re-entrant flow as thick as the cavity. Thus it is unlikely that the propagation liquid front or a discontinuity is caused by same flow turning mechanism as that produces shedding at the aft of the cavity.

The transition in mechanisms happens abruptly with small changes in pressure and it lies in the asymptotic portion of the cavity length and cavitation number curve, as shown in Figure 5.4. This means that the cavity grows in length instantaneously before being arrested. Such an abrupt change would lead the interfacial liquid flow to slow down abruptly producing an increase in pressure. Such sudden changes in fluid properties can result in the production of a “water hammer” like discontinuity that propagates into the cavity. As illustrated in Figure 7.5 (d) – (e) the propagating discontinuity drags the downstream flow, which could be re-circulating, with itself to be in agreement with the kinematics of a shock wave, as shown in Figure 7.5 (g). This results in leading edge shedding of vapour clouds, as shown in Figure 7.5 (f).

This is a different scenario when compared to stagnation point at the rear of the cavity on the wedge surface which resulted in re-entrant flow induced rear pinch-off. In the case of rear pinch-off the liquid flow is in kinematic equilibrium with a constant pressure cavity that facilitates the existence of a re-circulating flow, while a propagation discontinuity is produced due to lack of

kinematic equilibrium dictated by the cavity growth rate. The presence of an obstacle along the path of the discontinuity will not have an effect because of the nature of the process that produces the discontinuity.

7.5. Shock Wave Properties

From time resolved void fraction flow field measurements, the velocity of the shock wave in the laboratory frame can be determined. The definition of shock speed in the laboratory frame is shown in Figure 7.6. For an observer stationary in the laboratory frame of reference, the shock wave appears to travel in a direction opposite to the mean flow direction outside the cavity. Thus the X-ray videos obtained by a stationary X-ray source and imager in the laboratory frame can be used to estimate the shock propagation speed. By plotting the variation of void fraction as a function of time along the *s* direction at a constant distance *n* from the wedge surface, the velocity of the shock wave can be determined. Figure 7.7 illustrates the calculation of the shock speed from the void fraction flow speed measurements. From Figure 7.7 it can be seen that the an iso-contour line represented by an increasing slope in the *s-t* plane represents the cavity collapse speed. Similarly the cavity growth rate can be estimated by calculating the slope of the line with a decreasing slope in the s-t plane.

The shock speeds thus determined depended upon the cavitation number for a given free stream speed. The number of cycles for a given X-ray recording also increased, as illustrated in Figure 5.21 in Chapter 5. For a given cavity length this meant that a whole cycle of cavity growth and collapse happened faster for a faster speed. Figure 7.8 shows the computed shock speed for different free stream speeds and cavitation number. Figure 7.9 shows the variation of ratio of shock speed to inlet speed U_0. With an increase in speed, the shock speed in the laboratory frame

increased. The pre- and post-shock void fraction can also be determined for a given *s* location as shown in Figure 7.5. Figure 7.10 and 7.11 show the variation of pre- and post-shock void fraction for different cavitation numbers, σ_0.

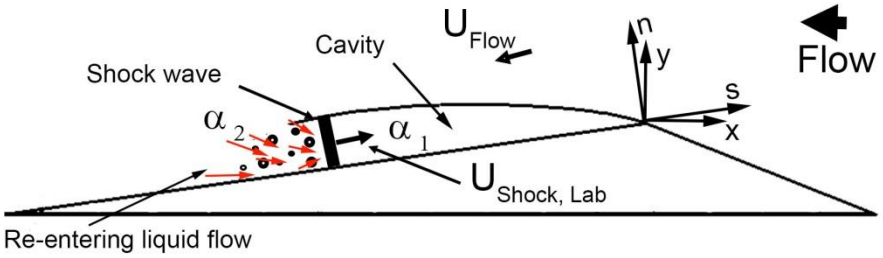

Figure 7.6: Shedding cycle in the presence of an obstacle

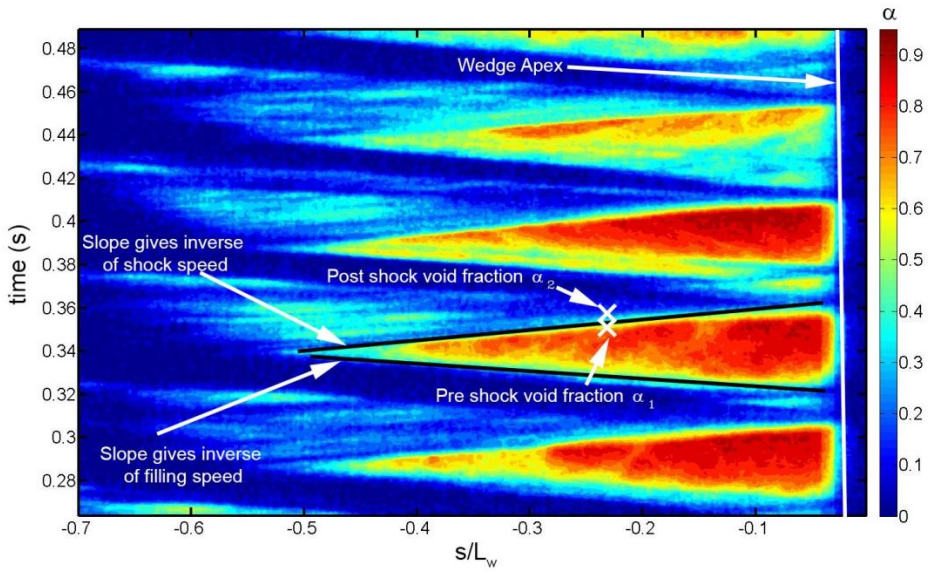

Figure 7.7: Shock speed determination from s-t diagram with illustration of pre and post shock void fraction values.

Lines in Figure 7.8 represent linear fits to the observed trends for shock speeds. The fit is used for illustration purposes to show that the average shock speed increases with an increase in inlet speed, U_0. The trend exhibited by the shock speeds observed for 8 m/s is opposite than those of

6 and 10 m/s. The values are close and the standard deviation from different trials was around 50%.

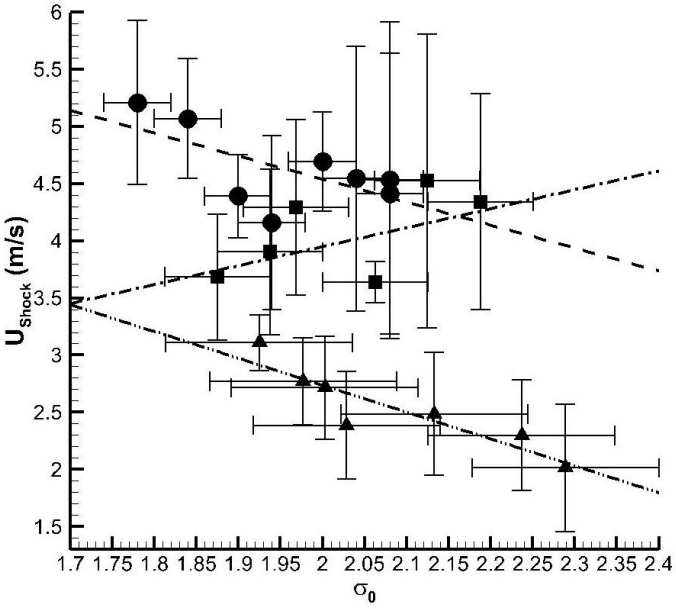

Figure 7.8: Variation of shock speed with cavitation number ▲- 6 m/s, ■ – 8 m/s, ●- 10 m/s with fitted lines double dotted dashed line- 6 m/s, dotted dashed line- 8 m/s, dashed line- 10 m/s

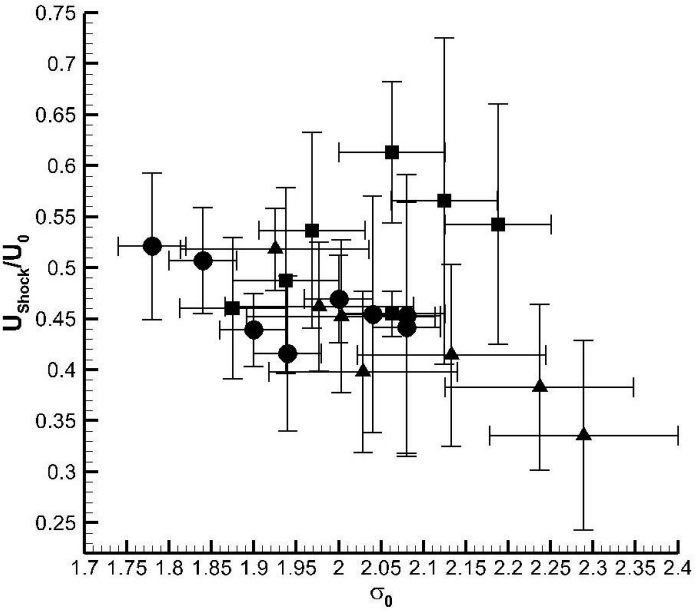

Figure 7.9: Variation of non-dimensional shock speed with cavitation number ▲- 6 m/s, ■ – 8 m/s, ●- 10 m/s

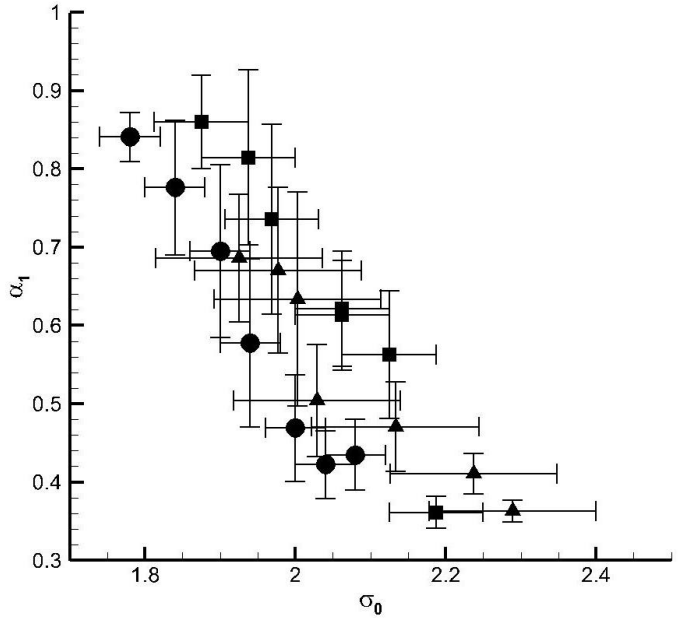

Figure 7.10: Variation of averaged pre-shock void fraction α_1 speed with cavitation number ▲- 6 m/s, ■ – 8 m/s, ●- 10 m/s

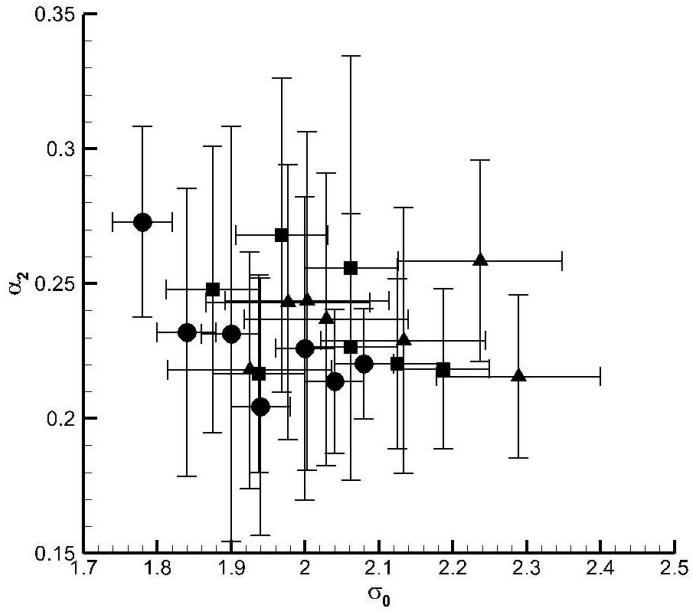

Figure 7.11: Variation of averaged pre-shock void fraction α_2 speed with cavitation number ▲- 6 m/s, ■ – 8 m/s, ●- 10 m/s

Thus the observed trend is not very likely due to the flow physics facilitated by lower inlet speeds. The variation of the pre- and post-shock void fraction, α_1 and α_2, are shown in Figures 7.10 and 7.11 respectively. The pre- and post-void fraction values were averaged for a number of cycles for a given cavitation number. This averaging is similar to the phase averaging, yet only for those cases with pronounced shedding. It can be seen that the pre-shock void fraction α_1 increased with a decrease in cavitation number for all speeds. The free stream speed seems to a have weak effect on the pre shock state void fraction.

Figure 7.11 shows the variation of post-shock void fraction, and it can be clearly inferred that cavitation number does not have an effect, and a constant value of $\alpha_2 = 0.20$ was observed for all speeds and cavitation numbers. There are two reasons for this observed value. The first is the consequence of the averaging or choosing the condition that corresponds the post state. This constant value is partially due to the manner of choosing the post state to calculate the shock speed. Second, condensation shock waves do not have a flat wave front. For a given pre shock state, a post-shock state is realized by series of compressions and this series depends upon the pre-state and post-state bubble sizes and natural frequencies. Thus the observed value of constant void fraction could be due to the condensation process occurring in different stages with the first stage being a constant value irrespective of the speed of cavitation number.

7.6 Chapter Summary

1. Estimation of averaged vapour flow direction by correlation of void fraction signals results in reversed flow regions for both re-entrant shedding and shock shedding. Thus the method does not preclude the nonexistence of condensation shocks.
2. The presence of the obstacle does not have an effect on shock induced shedding

dynamics, suggesting the global nature of the processes involved in the creation of shock waves.

3. Comparison of the details of the mechanisms reveals that for the presence of a re-entrant liquid flow, a stagnation point needs to be located at the aft of the cavity. In such a scenario, a liquid re-entrant flow will produce shedding due to pinch-off at the aft portion of the cavity. This is caused due to kinematics of flow that is in equilibrium with a constant pressure cavity.
4. Thickness of the re-entrant liquid flow cannot attain the thickness of the cavity based on the kinematics of a flow in equilibrium with the cavity. This would require the interfacial streamline to turn 180 degrees with a short radius of curvature. Instead, the observed propagating discontinuity could be produced due to sudden arrest of the cavity growth process. This would result in the production of a water-hammer like discontinuity propagating into the cavity while at the same time dragging the liquid aft of the cavity.
5. Observed shock speeds tend to increase with increase in inlet speeds without substantial differences in the void fraction flow fields.

CHAPTER 8

Bubbly Shocks

Partial cavities in separated flows can experience high values of instantaneous void fractions and hence low speed of sound values as discussed in Section 1.6. In the previous chapter it was seen that the presence of bubbly shock waves is the dominant mechanism of cloud shedding. The physical conditions needed for the existence of these shock waves can reveal more insights into the mechanisms of shock induced shedding. In particular, the relationship of occurrence of shock waves to void fraction distribution, cavity growth rate, inlet pressures and flow speeds would lead towards the holistic understanding of the mechanism in terms of fundamental flow parameters. This chapter aims to understand the observed flow physics in relation to the measured quantities. This is done in the following manner:

1. Using simple one-dimensional bubbly shock flow analysis, a relationship between the void fraction difference across the shock wave, pressure difference across the shock wave, and the shock speed is obtained.
2. Based on the measured void fraction values using X-ray densitometry and the measured shock speed, the pressures before and after the shock are predicted.
3. Predicted values of the pressure from the one-dimensional analysis are compared with the measured pressure.

4. The relationship between cavity growth rate and the occurrence of shock wave induced shedding is then explored by analyzing the time resolved void fraction flow fields for periodic shedding.

8.1 One-Dimensional Bubbly Shock Waves

Simple conservation relations hold good across discontinuities in fluid flows such as shock waves. Conservation of quantities such as mass and momentum before and after shocks can be used to estimate the relationship between pre- and post-shock states. Our goal is to relate the shock speed to measured flow quantities such as void fraction and cavity pressures. The case of a stationary shock wave can be used to estimate the flow speed, u_1, into the shock wave. The schematic of a bubbly mixture entering and leaving a shock is shown in Figure 8.1. Across the shock wave, we have

$$\rho_1 u_1 = \rho_2 u_2 \tag{8.1}$$

$$\rho_1 u_1^2 + p_1 = \rho_2 u_2^2 + p_2 \tag{8.2}$$

$$\rho_i \approx \rho_L (1-\alpha_i) \tag{8.3}$$

Equations (8.1 – 8.3) represent continuity, momentum, and mixture density approximation of a bubbly flow across a shock wave. Using the equations (8.1-8.3), an expression for the incoming flow speed in the reference frame of the shock can be obtained. Equation (8.4) does not take into account the energy conservation across the shock which means that the bubble dynamics of the shocking process is ignored.

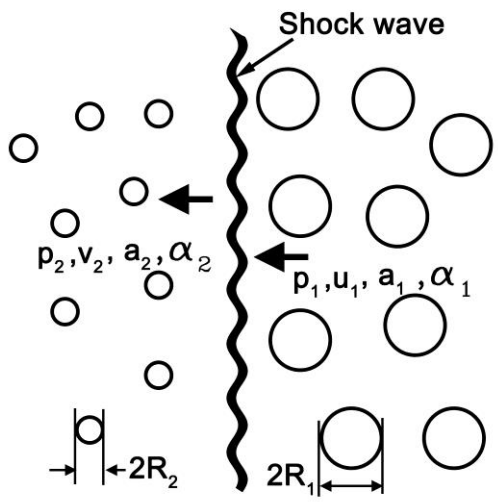

Figure 8.1: Illustration of 1-D bubbly shock wave

$$u_1^2 = \frac{(p_2 - p_1)}{\rho_L}\left[\frac{(1-\alpha_1)}{(1-\alpha_2)(\alpha_1-\alpha_2)}\right] \tag{8.4}$$

The speed expressed in Equation (8.4) is equal to the shock propagation speed into a stationary bubbly mixture. From Equation (8.4) it can be seen that the pressure before and after the shock wave has an important role to play in setting the shock speed. This is an important relation because the shock speeds have to be on the right order to achieve periodic shedding. This relationship also explains the sensitivity of the observed shedding dynamics to the inlet pressure and hence cavity pressure. Based on this relation the following are expected,

1. The difference between pressures $(p_2 - p_1)$ should increase for increasing shock speeds, provided the void fraction flow field remains unchanged. From the previous chapter, it was found that the upstream α_1 and downstream void fraction α_2 did not change drastically with the free stream speed, however the shock speed increased with increase in speed. Thus the quantity $(p_2 - p_1)$ is expected to increase with increase in speed. This qualitative relation is based on 1-D bubbly shock analysis.

2. Using Equation 8.4, the values of shock speed $U_{Shock,Lab}$, and the averaged pre-and post-shock void fractions α_1 and α_2 reported in Chapter 7, the expected values of $(p_2 - p_1)$ can be predicted across the shock. This predicted value can be compared with the measurements made on the underside of the cavity. Table 8.1 displays this estimated value for different speeds.

The findings are presented in Section 8.5.

σ_0	U_0 = 6 m/s		U_0 = 8 m/s		U_0 = 10 m/s	
	$(p_2 - p_1)_{Theo}$(kPa)		$(p_2 - p_1)_{Theo}$(kPa)		$(p_2 - p_1)_{Theo}$(kPa)	
1.88	1.81	+/- 0.01	1.55	+/- 0.03	4.08	+/- 0.04
1.94	1.43	+/- 0.03	2.16	+/- 0.07	3.54	+/- 0.02
1.97	1.39	+/- 0.04	3.11	+/- 0.10	3.43	+/- 0.12
2.06	0.99	+/- 0.04	4.65	+/- 0.06	3.67	+/- 0.03
2.06	1.02	+/- 0.05	2.46	+/- 0.01	3.16	+/- 0.21

Table 8.1: Theoretical values of $(p_2 - p_1)_{Theo}$ for different speeds using Equation 8.4

8.2 Measurement of Averaged Cavity Pressure

The static pressure in the cavity was measured using pressure taps on the wedge surface. The locations of the static pressure taps and flush mounted dynamic pressure transducers are shown in Figure 8.2. Tap 1 was located at the wedge apex, and Tap 2 was located downstream of the apex but still within a stable cavity. The unsteady cavity pressure was also measured using a flush mounted dynamic pressure transducer with a high frequency response on the wedge surface. The static pressure taps were connected to 1/8th inch tubing which was then connected to a Omega PX000005PSIA absolute pressure transducer. To prevent the lines from out gassing, the

tubes were purged with de-aerated water from the tunnel, and the transducer was placed at a height of 2 feet below the tap location in the direction of gravity. This additional head prevented the out gassing of vapour in the lines, and the final pressures were corrected with this head value.

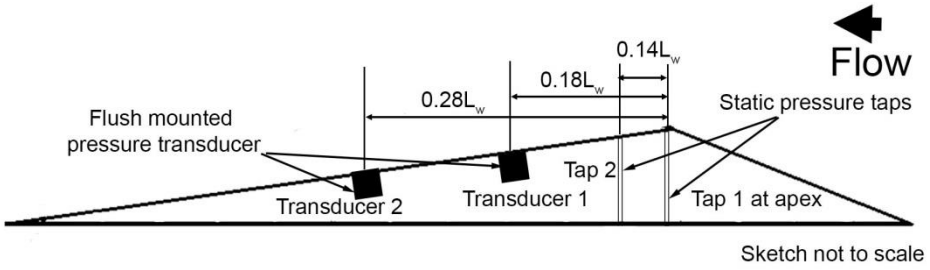

Figure 8.2: Pressure transducer locations.

8.3 Wedge Apex Pressure

Pressure at the apex of the wedge was measured for different cavitation numbers and flow speeds. Beginning at a high cavitation number which resulted in minimal to no cavitation at the wedge apex, the pressure was gradually reduced until a stable cavity remained attached at the wedge apex. The definition of the quantities calculated using the wedge apex pressure are shown in Equations 8.5 through 8.7 The variation of the magnitude of apex pressure p_{Apex}, the coefficient of pressure at the apex $C_{p,Apex}$, and the apex cavitation number cavitation number σ_{Apex} are shown in Figures 8.3, 8.4, and 8.5, respectively.

$$p_{Apex} = \overline{p_{Tap1}} \tag{8.5}$$

$$C_{p,Apex} = \frac{(p_{Tap1} - p_0)}{\frac{1}{2}\rho_L U_0^2} \tag{8.6}$$

$$\sigma_{apex} = \frac{(p_{Tap1} - p_v)}{\frac{1}{2}\rho_L U_0^2} \tag{8.7}$$

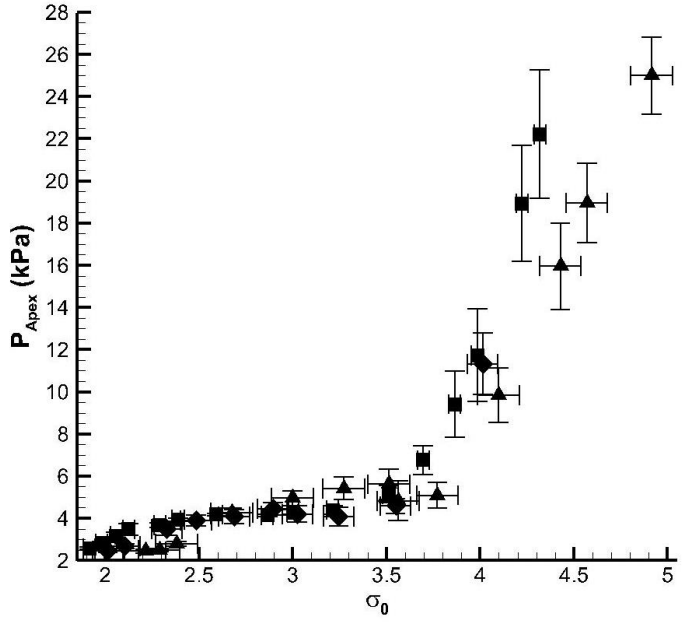

Figure 8.3: Pressure at wedge apex for different cavitation numbers and flow speeds. ▲- 6 m/s, ♦- 7 m/s, ■ – 8 m/s

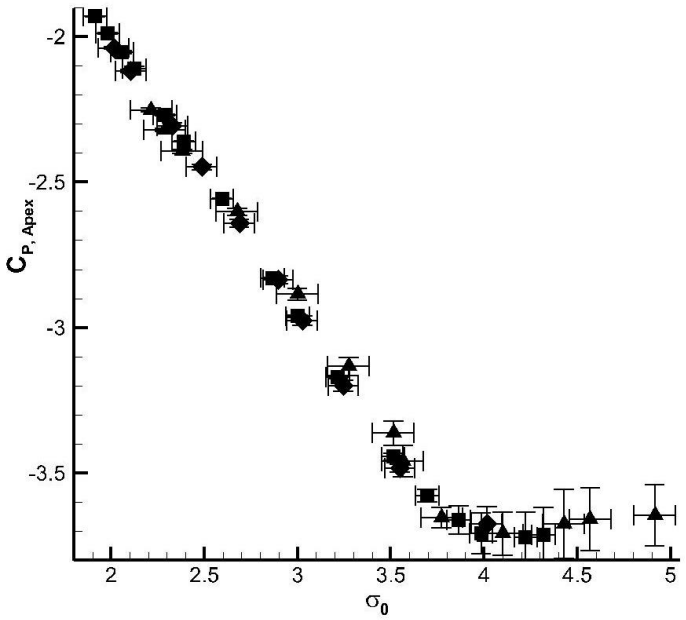

Figure 8.4: $C_{P,Apex}$ for different cavitation numbers. ▲- 6 m/s, ♦- 7 m/s, ■ – 8 m/s

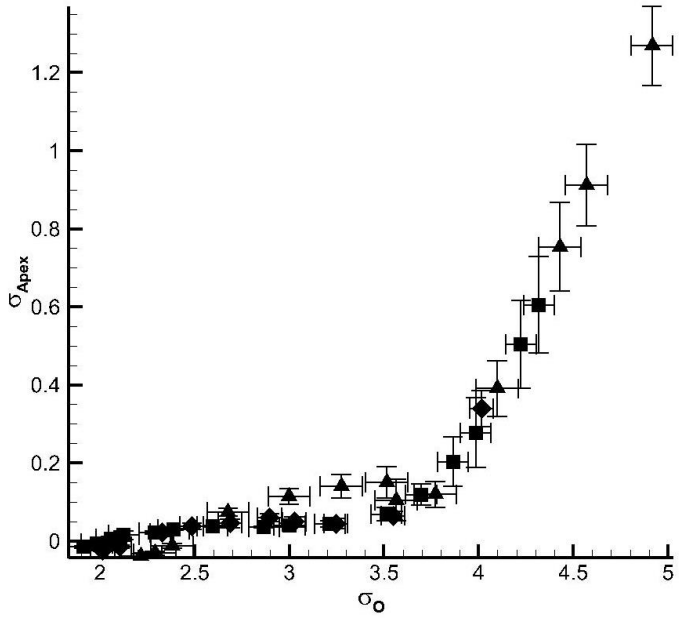

Figure 8.5: Wedge apex cavitation number for different cavitation numbers and flow speeds. ▲- 6 m/s, ♦- 7 m/s, ■ – 8 m/s

Once the apex pressure reached a value closer to vapour pressure (i.e. inception), there was minimal to no change in the apex pressure with decreasing inlet cavitation number σ_0. Figure 8.5 suggests that the cavity apex remains in tension when the cavitation number begins to drop to values under inception cavitation number.

8.4 Averaged Static Pressure Underneath the Cavity

The static pressure on the underside of the cavity was measured at the location Tap 2. The definitions of the measured pressure and derived quantities are shown in Equations 8.8 to 8.10. The variation of the magnitude of cavity pressure p_{Cavity}, the coefficient of pressure at the apex $C_{p,Cavity}$, and the apex cavitation number cavitation number σ_{Cavity} are shown in Figures 8.3, 8.4, and 8.5 respectively.

$$p_{Cavity} = \overline{p_{Tap2}} \tag{8.8}$$

$$C_p = \frac{(p_{Tap2} - p_0)}{\frac{1}{2}\rho_L U_0^2} \tag{8.9}$$

$$\sigma_{Cavity} = \frac{(p_{Tap2} - p_v)}{\frac{1}{2}\rho_L U_0^2} \tag{8.10}$$

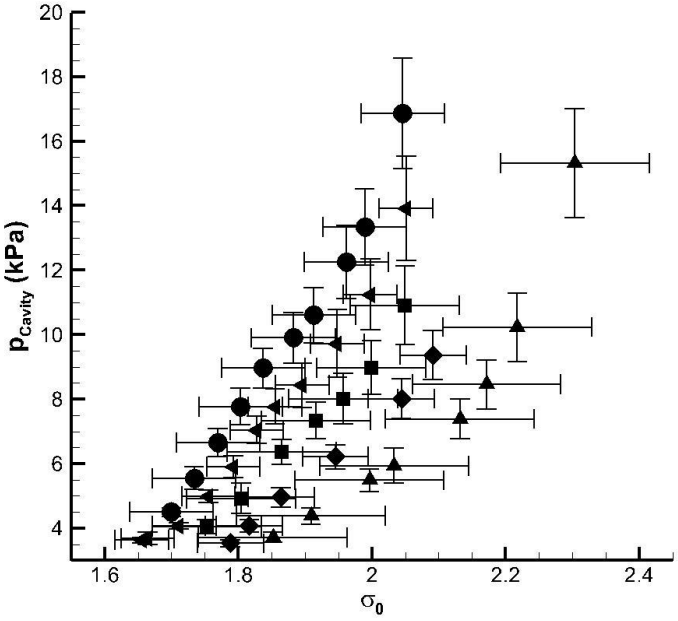

Figure 8.6: Pressure in the cavity for different cavitation numbers and flow speeds. ▲- 6 m/s, ♦- 7 m/s, ■ – 8 m/s, ◄ – 9 m/s, ● – 10 m/s

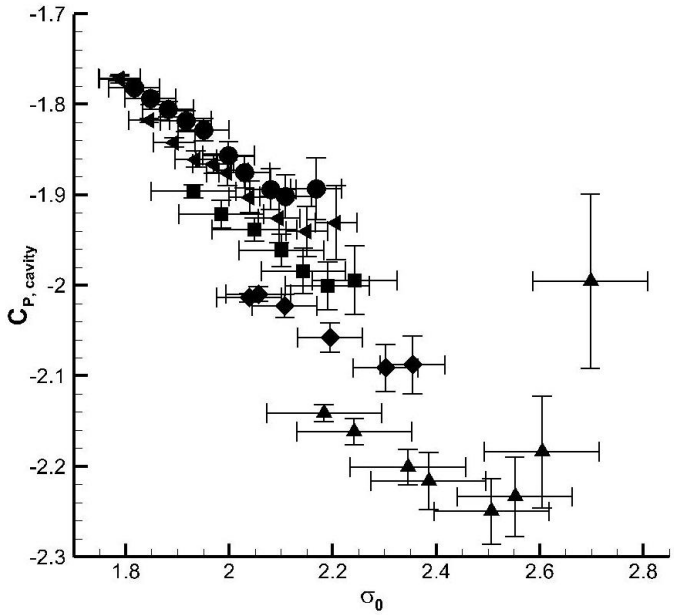

Figure 8.7: Averaged pressure coefficient in the cavity for different cavitation numbers and flow speeds. ▲- 6 m/s, ♦- 7 m/s, ■ – 8 m/s, ◄ – 9 m/s, ● – 10 m/s

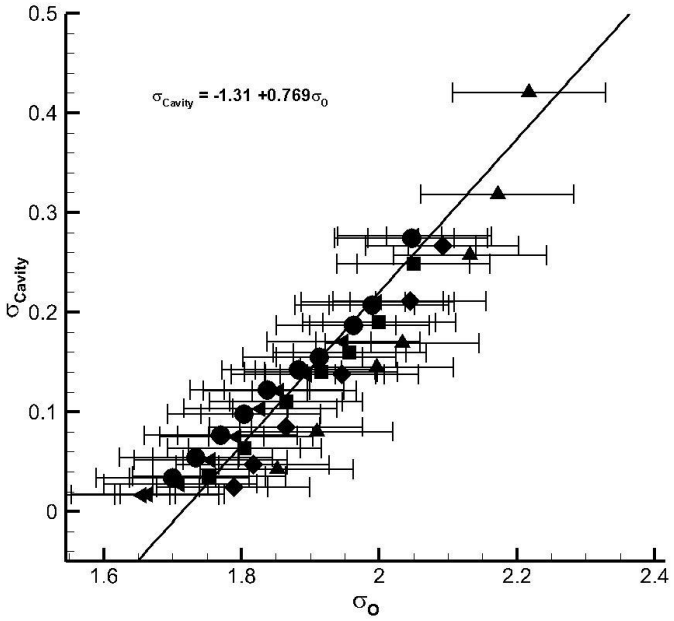

Figure 8.8: Averaged cavitation number in the cavity for different cavitation numbers and flow speeds. ▲- 6 m/s, ♦- 7 m/s, ■ – 8 m/s, ◄ – 9 m/s, ● – 10 m/s

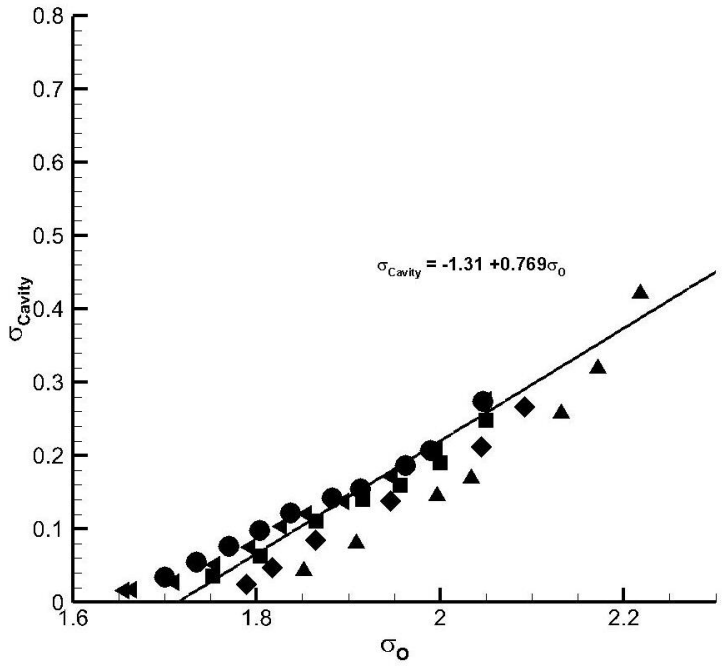

Figure 8.9: Averaged cavity cavitation number with curve fit at low cavitation numbers. Flow speeds. ▲- 6 m/s, ♦- 7 m/s, ■ – 8 m/s, ◄ – 9 m/s, ● – 10 m/s

From the context of measuring the pressures upstream and down-stream of a shock, the cavity pressure shown in Figures 8.6 – 8.9 do not represent the quantities of interest. For the cases exhibiting oscillatory cavity length behaviour and periodic shedding, the value of the pressure measured at Tap 2 represents the average pressure in a given cycle. The fraction of the values represented by pressures close to those in pre- and post-shock states need to be estimated to understand the averaged pressure represented by p_{Tap2}.This is expressed in Equation 8.11.

$$p_{Tap2} = \overline{(ap_1 + (1-a)p_2)} = a(\overline{p_1}) + (1-a)(\overline{p_2}) = p_{Tap2} \tag{8.11}$$

In Equation 8.11, *a*, is a constant that represents the fraction of the time in which the pressure tap was in a pre-shocked state (p_1), and (*1-a*) represents the fraction of the time in which the pressure tap was experiencing the pressure after the shocking process p_2. There are many ways

to estimate the value of the constant '*a*'. For the present study, a void fraction probe was placed at the location of the pressure tap, but at a distance of 5 mm from the wedge surface. A histogram of the void fraction signal was then plotted as shown in Figure 8.10.

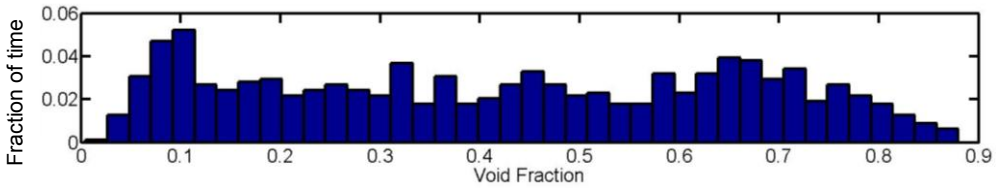

Figure 8.10: Histograms of % of time for different values of void fraction for U_0 *= 8 m/s*

The fraction of the time when the time signal was greater than the post shock void fraction state (α_2*=0.25*) shown in the previous chapter was calculated. This represented the fraction '*a*'. Table 8.2 shows the values of 'a' determined for different speeds using the methodology mentioned above. The trends expressed in Figures 8.7 through 8.9 will be discussed after the next section.

σ_0	U_0 = 6 m/s	U_0 = 8 m/s	U_0 = 10 m/s
1.88	0.65	0.75	0.76
1.94	0.60	0.70	0.70
1.97	0.58	0.63	0.59
2.06	0.32	0.58	0.47
2.13	0.23	0.41	0.46
2.19	0.10	0.033	0.25

Table 8.2: Constant "a" for different cavitation numbers and flow speeds

8.5 Dynamic Pressure Measurement

In addition to the measurement of average pressure in the cavity, the variation of the cavity pressure in relation to the flow processes were also measured using a flush mounted dynamic

pressure transducers.

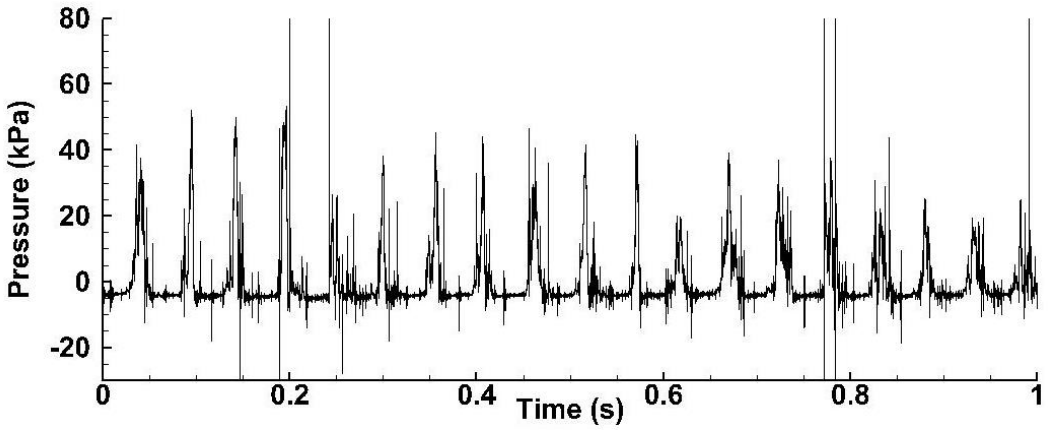

(a)

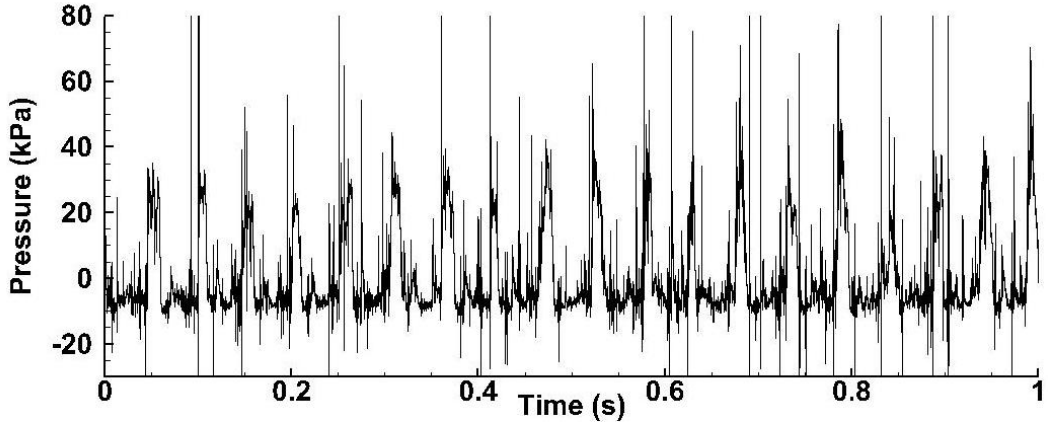

(b)

Figure 8.11: Unsteady pressure transducer signals from Transducers T1 and T2

The location and the nomenclature of the transducers are shown in Figure 8.2. The transducer closer to the wedge apex corresponds to "Transducer 1", and the transducer farther is designated as "Transducer 2". In addition to the transducer configuration shown in Figure 8.2, another

dynamic pressure transducer configuration, with a single transducer was also used. The results from the single dynamic pressure configuration were used in the Strouhal number plots presented in Chapter 6. A sample raw, unfiltered, time synchronized pressure signals from transducers (T1) and (T2) are shown in Figure 8.11 (a) and (b).Time synchronization of the pressure signals with the X-ray videos was also done to facilitate the visualization of the processes that cause the pressure fluctuations. Figure 8.12 shows the various prominent processes and their corresponding pressure signal feature. The features shown in Figure 8.12 are a part of the signal shown in Figure 8.11 from 415 to 475 *ms*. A consequence of having a time synchronized pressure and void fraction measurement is the ability to measure the pressure difference in the transducer when the shock crosses the transducer.

From the X-ray videos, the instant in time when the shock crosses the transducer can be determined. This information can be used to measure the pressure rise registered by the transducer during the shocking process. The pressure signals were digitally filtered using a low pass filter set a pass value of 1 kHz with the roll-off occurring at 2.5 kHz. However, the condensation shock waves do not propagate uniformly in the span wise direction. This was evident from the top view of the high speed videos that were presented in Chapter 6. This results in the presence of many peaks around the shock propagation frame identified in the X-ray videos. Since the transducer has a high frequency response, the pressure signal would have a "pressure wiggle" faster time variations when compared with the frame rates. This enables us to identify multiple instance of shock propagation across the transducer, when the shock front is not uniform in the span wise direction. In such a scenario, the average of all the pressure peaks around the shock crossing frame from the X-ray videos is used to estimate the pressure rise across the shock. This is illustrated in Figure 8.13.

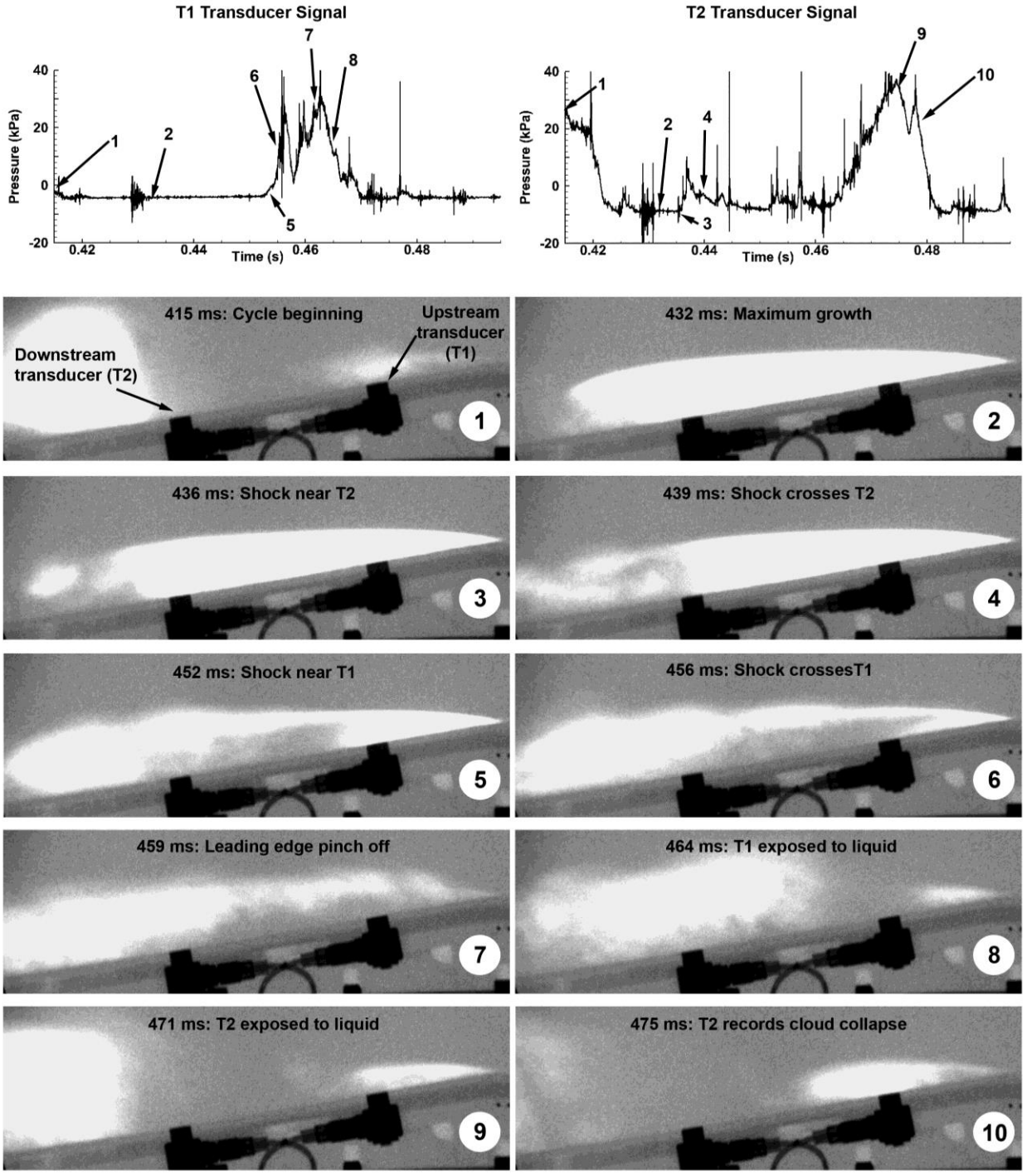

Figure 8.12: Time series of shock dynamics in the vicinity of the pressure transducers. X-ray videos time synchronized with transducer measurements.

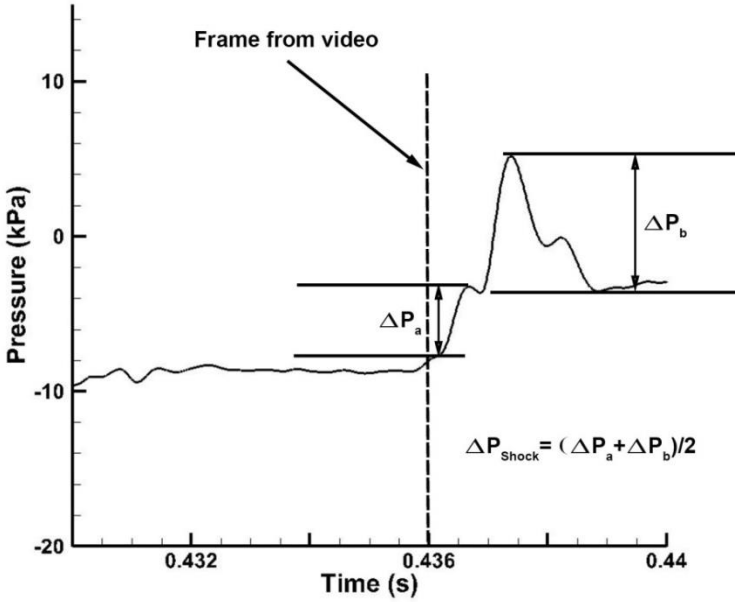

Figure 8.13: Determination of pressure rise across the shock from a filtered unsteady pressure transducer signal.

It should be noted that this value of pressure difference is *not the absolute value.* However, to aid in the analysis, it can be used as a reasonable measure of the pressure rise.

σ_0	U_0 = 6 m/s				U_0 = 8 m/s				U_0 = 10 m/s			
	$(p_2 - p_1)_{Theo}$ *(kPa)*		$(p_2 - p_1)_{Exp}$ *(kPa)*		$(p_2 - p_1)_{Theo}$ *(kPa)*		$(p_2 - p_1)_{Exp}$ *(kPa)*		$(p_2 - p_1)_{Theo}$ *(kPa)*		$(p_2 - p_1)_{Exp}$ *(kPa)*	
	Avg	+/-	*Avg*	+/-	*Avg*	+/-	*Avg*	+/-	*Avg*	+/-	*Avg*	+/-
1.88	1.81	0.01	0.34	0.12	1.47	0.03	3.30	0.69	4.08	0.04	8.20	0.99
1.94	1.43	0.03	2.00	0.20	2.65	0.07	3.70	0.40	4.00	0.02	4.20	0.75
1.97	1.71	0.04	0.79	0.23	3.11	0.10	2.08	0.34	3.43	0.12	9.10	0.64
2.06	1.07	0.04	2.41	0.45	3.61	0.06	2.38	0.22	3.29	0.03	-	-
2.06	1.02	0.05	2.40	0.37	2.78	0.01	4.00	1.04	3.43	0.21	-	-

Table 8.3: Theoretical and experimentally measured values of values of $(p_2 - p_1)$

From Table 8.3 the following information can be inferred.

1. The measured values of $(p_2 - p_1)$ across the shock qualitatively increase with increase in inlet speed and shock speed, consistent with the trend proposed by Equation 8.4
2. The measured values of $(p_2 - p_1)$ are higher in magnitude than those predicted by Equation 8.4 mainly for higher inlet speeds. First, the transducer used in the study is not an absolute pressure transducer. The values of $(p_2 - p_1)$ should be strictly interpreted as an electrical output proportional to the pressure rise across the shock. Nevertheless, the measurement is used for analysis. It should be noted that the shock waves in the case of shedding cavities are propagating into a filling cavity, unlike a steady flow assumed in the 1-D bubbly flow analysis. Thus the trend in the increase in pressure rise resembles a physical conclusion consistent with the global picture.

8.6 Determination of p_1 and p_2 From Static and Dynamic Pressure Measurements

From the measurements of the average cavity pressures using the static pressure taps, and the pressure rise across the shocks, the pre- and post-shock pressures can be estimated. Equations 8.12 through 8.15 illustrate the system that can be solved to obtain the pressures from the measurements. Table 8.4 shows the value of the pre- and post-shock pressures for different speeds and cavitation numbers.

$$p_{Cavity} = a(p_1) + (1-a)(p_2) \tag{8.12}$$

$$\Delta p_{Shock} = p_2 - p_1 \tag{8.13}$$

$$p_2 = p_{cavity} + a(\Delta p_{Shock}) \tag{8.14}$$

$$p_1 = p_{cavity} - (1-a)(\Delta p_{Shock}) \tag{8.15}$$

σ_0	6		8		10	
	p_2	p_1	p_2	p_1	p_2	p_1
1.88	3.93	3.59	8.84	5.54	16.07	7.93
1.94	5.60	3.60	9.93	6.23	13.55	9.33
1.97	5.94	5.15	9.32	7.24	17.99	8.42
2.06	6.71	4.30	10.36	7.98	X	X
2.13	7.93	5.53	X	X	X	X

Table 8.4: Obtained values of pre- and post-shock pressures from averaged static and dynamic pressure measurements for different cavitation numbers and flow speeds

It should be noted that p_1 represents the averaged pressure in the cavity before shocking, hence a proxy for averaged cavity pressure in general. Looking at the trends in Table 8.4, one can infer the following:

1. The average cavity pressure is higher for higher flow speeds. It should be noted that the average inlet pressure is also higher for higher flow speeds to achieve the same cavitation number.
2. Comparison of the experimental cavity shapes with the free-streamline solutions shown in Chapter 5 suggests that the cavity tends to attain a shape represented by a constant pressure boundary until the point of maximum thickness. The measurements of pressure at wedge apex show that the pressure in the cavity is very close to the vapour pressure. This means that the cavity tries to achieve vapour pressure for any given speed, but is

somehow prevented before being shed.

3. The reason for the cavity to sustain pressures higher than the vapour pressure before being shed needs to be explored. The cavity growth process plays and important role in understanding the reason and is explored next.

8.7 Shock Formation Process and Cavity Growth Rate

The rate of change of the vapor present in the cavity can be caluculated by taking a control volume (area) around the cavity. This volume depends upon the cavity length and hence the cavitation number. To estimate the averaged void fraction in the control volume, the sum on individual pixel void fraction A_i is summed and then divided by half the actual area of the control volume. Uniformity along the spanwise direction is assumed.

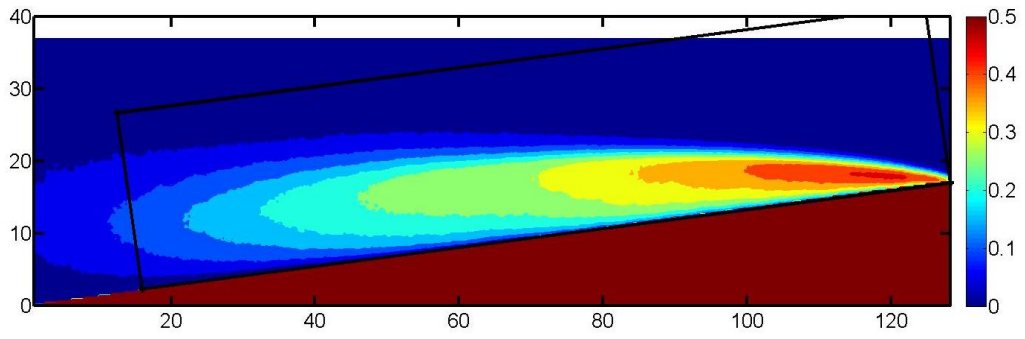

Figure 8.14: Control volume around the cavity for growth rate studies shown in solid black line.

Averaged density of the control volume is determined by using the approximation shown in Equation 4.3. Normalizing by the liquid density ρ_L, we get $\tilde{\rho}_{cavity}$

$$\tilde{\rho}_{Cavity}(t) = \left(1 - \frac{\sum_{i=1}^{n} \alpha_i A_i}{\sum_{i=1}^{n} A_i} \right) \tag{8.16}$$

The resulting number is an averaged void fraction or the density fraction of vapor in the control volume. The rate of change of this quatity in time can be determined from the measurements to give the rate of change of averaged the normalized density $\tilde{\rho}_{cavity}$.

$$\frac{(\tilde{\rho}_{cavity}(t) - \tilde{\rho}_{cavity}(t-1))}{\Delta t} = \frac{d\tilde{\rho}_{cavity}(t)}{dt} \tag{8.17}$$

As discussed earlier, the void fraction in these partial cavities can attain low enough values to change the speed of sound. This is equivalent to the pushing the speed of sound values from high liquid sound speed values to low mixture sound speed values as illustrated in Figure 2.5. The rate of change of normalized density signifies the change in the acoustic properties of the mixture. Since we are interested in what sets the pressure in the cavity, a comparison of the convective time scales of the cavity defined by $\frac{L_{Area}}{U_{Throat}}$, where L_{Area} is the length of the control volume in s-direction and U_{Throat} is the velocity at the wedge apex based on continuity, with the density change time scales $\frac{d(\tilde{\rho}_{cavity}(t))}{dt}$ can yield the information about the relative magnitudes of convective and vapour generation processes. To compare different speeds, we need to incorporate the cavitation number , σ_{Cavity}. This leads to the definition of following terms,

$$\frac{d(\tilde{\rho}_{cavity}(t))}{dt} t_{conv} = \frac{d(\tilde{\rho}_{cavity}(t))}{dt} \frac{L_{Area}}{U_{Throat}} \tag{8.18}$$

The quantities mentioned in Equations in 8.16 through 8.18 were calculated for all cavities. Figure 8.15 shows the variation of these quantities for a periodically shedding cavity at an inlet speed of U_0 = 8 m/s. Figure 8.15 (a) show the variation of the cavity density. The density attains a maximum value when the control volume is entirely filled with liquid and the least value when it is entirely filled with vapour. From Figure 8.15 (a) it can be seen that the average density begins to decrease as the cavity grows until the onset of cavity collapse initiated by the shock wave. Figure 8.15 (b) shows the magnitude of the variation in average density with time. From Figure 8.15 (c) it can be seen that for the case of shedding, the quantity $\frac{d(\tilde{\rho}_{cavity}(t))}{dt} t_{conv}$ attains a negative peak value before the onset of shock waves.

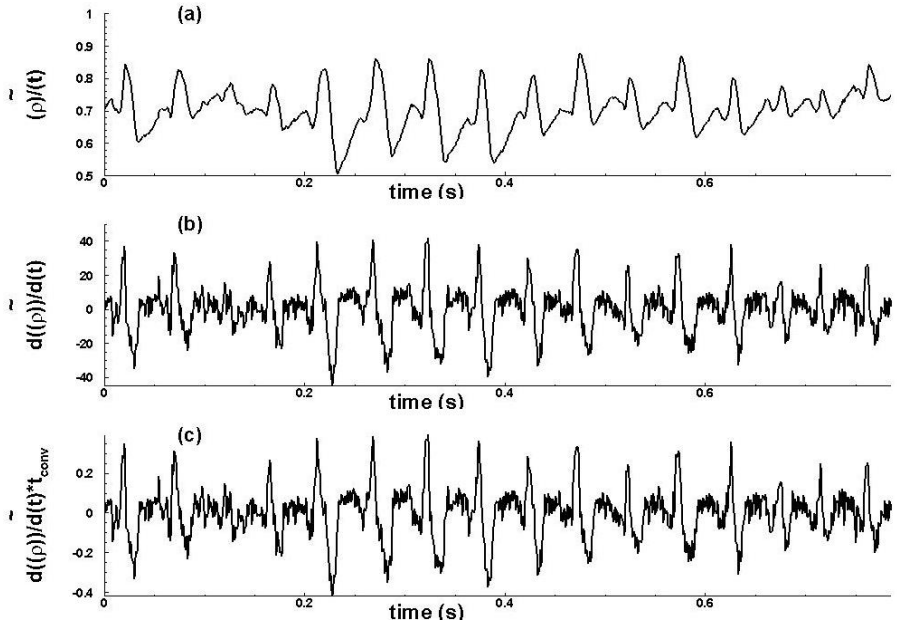

Figure 8.15: Variation of average cavity density (a), rate of change of cavity density (b) and ratio of density change time scale with the convection time scale (c) for a regularly shedding cavity.

This suggests the role of vapour generation process, which causes a rapid change in the cavity

density, is comparable to the convective time scale of the flow. This results in the production of shock waves at the rear of the cavity. Figure 8.16 shows the variation of the same quantities for a transitory cavity.

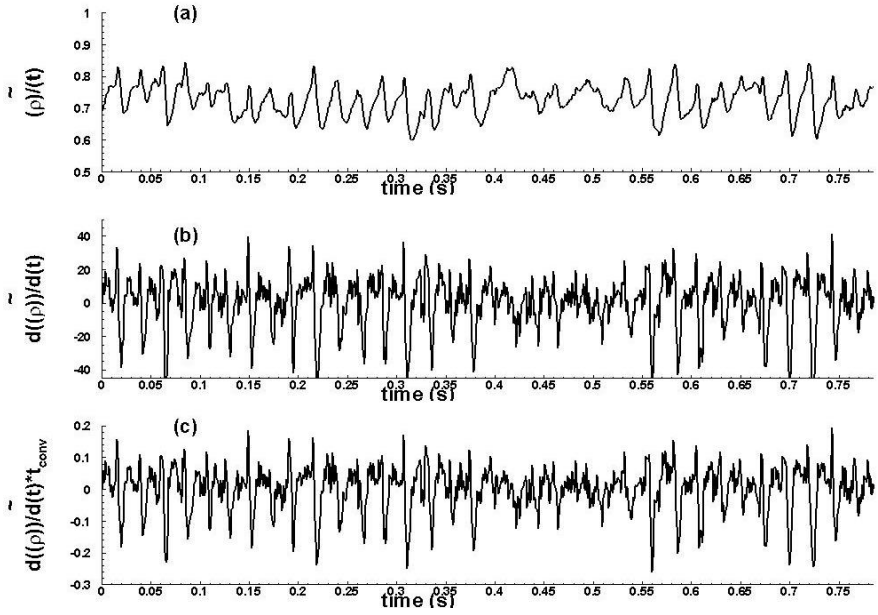

Figure 8.16: Variation of average cavity density (a), rate of change of cavity density (b) and ratio of density change time scale with the convection time scale (c) for a transitory cavity.

It can be seen that for certain cycles, the values of $\frac{d(\tilde{\rho}_{cavity}(t))}{dt}t_{conv}$ for transitory cavities shown in Figure 8.16 (c), are much lower than other cycles, due to slower growth rate. A time of series instantaneous void fraction images for the signal represented during the period from *0.4 -0.7s* is shown in Figure 8.17. For re-entrant flow induced shedding it can be clearly seen that the cavity growth rate is not as high. In this case the time scales set by vapour production processes are much slower than the re-entrant time scale which is evident in low values of $\frac{d(\tilde{\rho}_{cavity}(t))}{dt}t_{conv}$. In the time series it is evident that a shock wave occurs at the rear of the cavity when the cavity

growth rate (density drop rate) is higher and comparable to the convective time scale, as shown in points 5-8 in Figure 8.17.

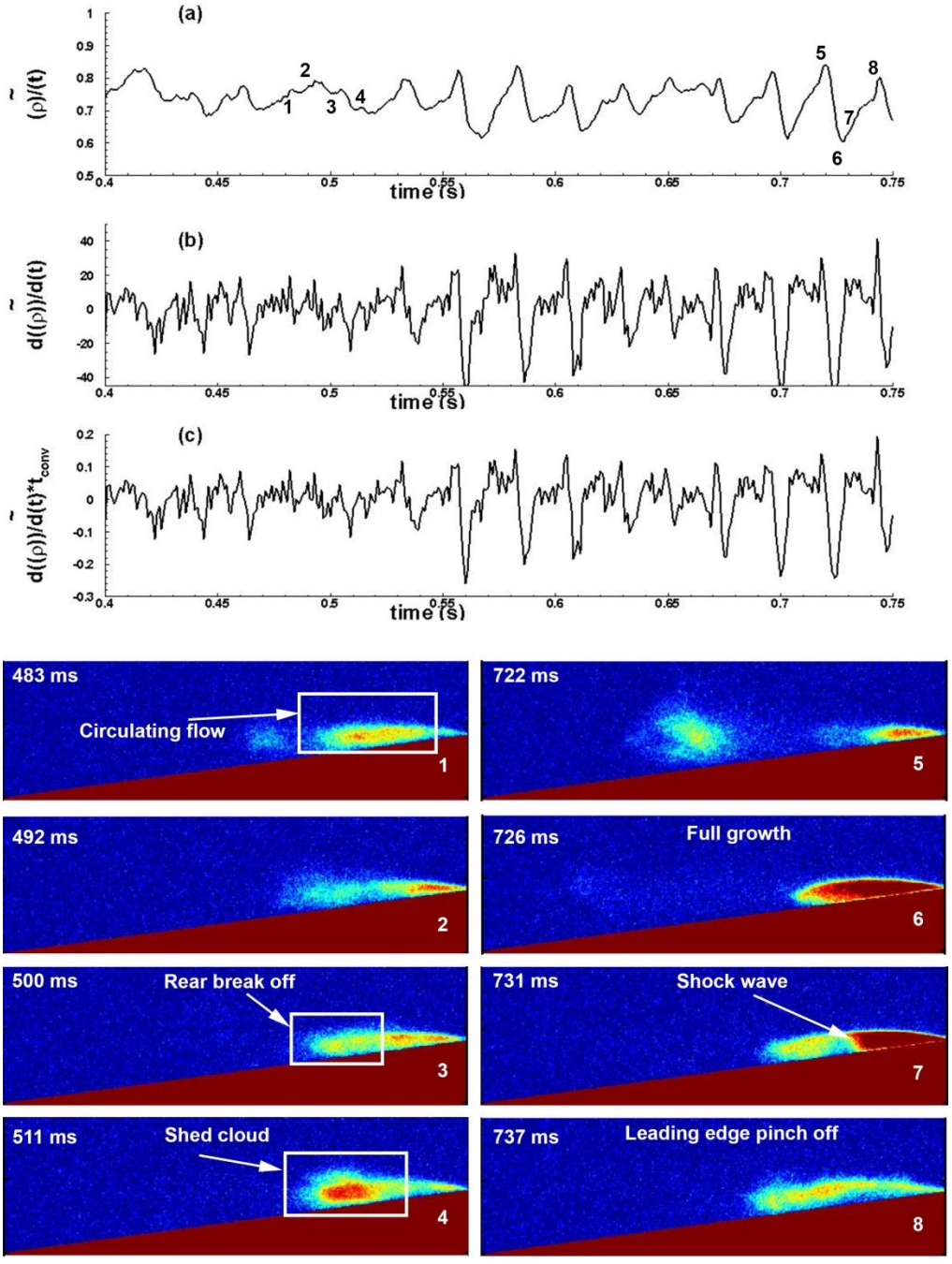

Figure 8.17: Time series of a transitory cavity illustrating the importance of rate of cavity growth to the onset of shock waves.

8.8 Variation of $\frac{d(\tilde{\rho}_{cavity}(t)/\sigma_{cavity})}{dt}t_{conv}$ with σ_0

Thus the quantity $\frac{d(\tilde{\rho}_{cavity}(t))}{dt}t_{conv}$ plays a critical role in the onset of the shock wave induced shedding of vapour clouds. To compare different cavitation numbers, and flow speeds, we can introduce the quantity $\frac{d(\tilde{\rho}_{cavity}(t)/\sigma_{cavity})}{dt}t_{conv}$ which is resembles an averaged speed of sound. Figure 8.18 shows a histogram of the fraction of the time spent in a given measurement and the corresponding $\frac{d(\tilde{\rho}_{cavity}(t)/\sigma_{cavity})}{dt}t_{conv}$ value for three different types of cavities. It can be clearly seen that as the cavitation number increases $\frac{d(\tilde{\rho}_{cavity}(t)/\sigma_{cavity})}{dt}t_{conv}$ value decreases. This is largely due to decrease in convection time scale since higher cavitation numbers are characterised with smaller convective time scales resulting from smaller cavity lengths for the same incoming speed. Having determined the role of $\frac{d(\tilde{\rho}_{cavity}(t)/\sigma_{cavity})}{dt}t_{conv}$ in cavity dynamics, the averaged value of $\left|\frac{d(\tilde{\rho}_{cavity}(t)/\sigma_{cavity})}{dt}t_{conv}\right| > 0$ for all cavities as function of cavitation number and speed is shown in Figure 8.19. The figure shows an increase in the values of $\left|\frac{d(\tilde{\rho}_{cavity}(t)/\sigma_{cavity})}{dt}t_{conv}\right|$ with decrease in cavitation number across different speeds signifying the importance of vapour production processes that makes the cavity vulnerable to shock.

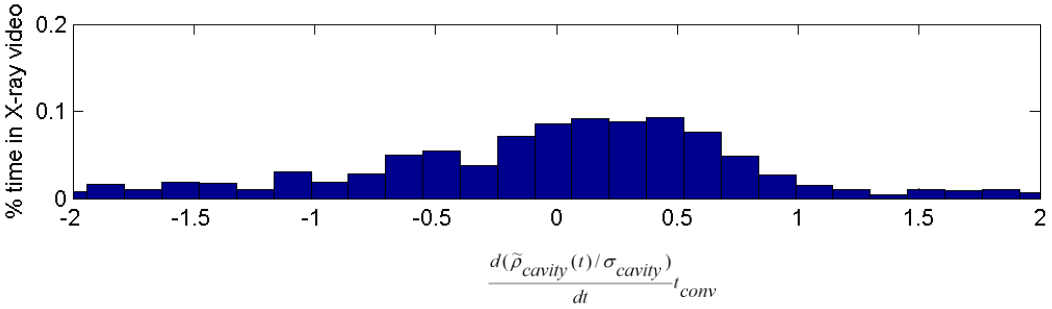

(a)

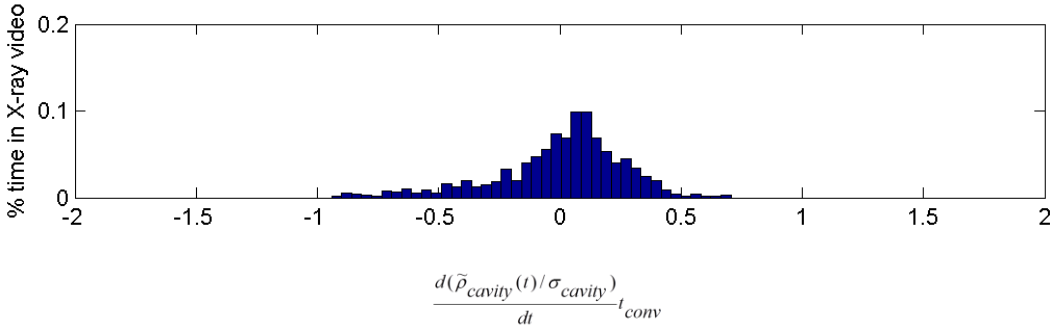

(b)

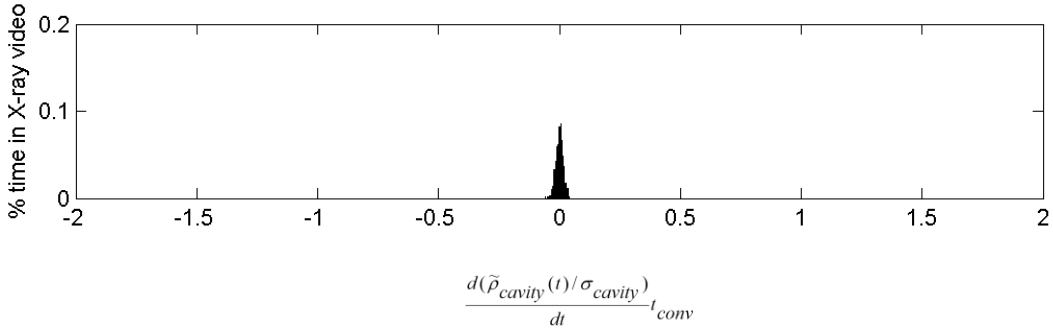

(c)

Figure 8.18: Histogram of observed magnitude of . $\frac{d(\tilde{\rho}_{cavity}(t)/\sigma_{cavity})}{dt} t_{conv}$ *for different types of cavities. (a) Periodic cavity (b) Transitory cavity (c) Incipient cavity*

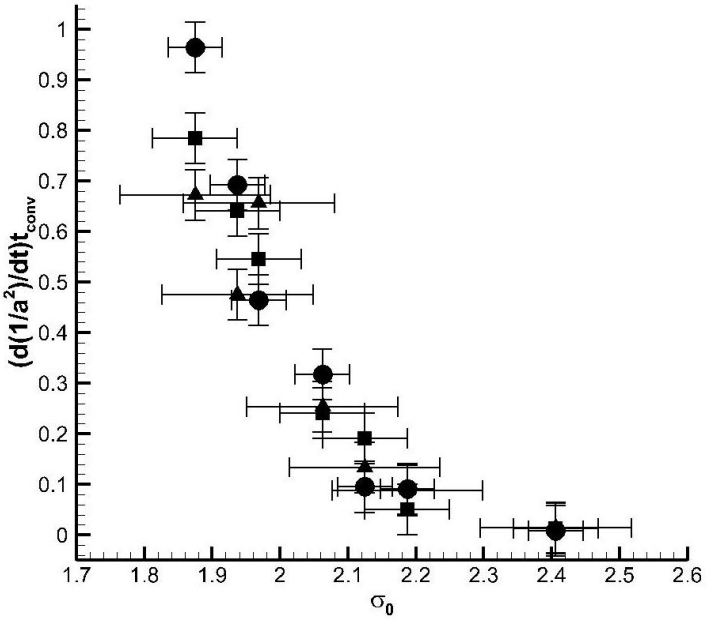

Figure 8.19: Variation of ratio of convective to density change time scales for different inlet cavitation numbers.

8.9 Role of Adverse Pressure Gradient in Cavity Closure

The analysis in the previous section suggests that time scales involved with reduction in density is comparable with the flow time scales for periodically shedding cavities. This is an important finding because this explains why the cavity pressure is higher for higher speeds. For the case of higher flow speeds, the average inlet pressure is also higher to achieve a given cavitation number for a higher speed. With the finding from the previous section, it can be inferred than the density drop rate is on the same order of the convective time scale for periodically shedding cavities. This means that a cavity at higher pressure and incoming flow speed has lesser time to achieve vapour pressure than the pressure change due to convection. This explains the observance of higher cavity pressures at higher speeds. For an incipient cavity which is closer to the wedge apex, the convection time scales are small enough that any change in density is not big enough to

interfere with flow processes by changing the speed of sound, which is characterised by low values of $\frac{d(\tilde{\rho}_{cavity}(t)/\sigma_{cavity})}{dt} t_{conv}$. This means that the pressure in such a scenario would be more likely closer to the vapour pressure as it was observed in Figures 8.3 -8.5. The above analysis also explains the trends observed in cavity pressures.

Upon identification of the role of rate of production of vapour, we can also identify the importance of pressure gradients. From the time series of a transitory case shown in Figure 8.17, we can see that there are two time scales associated with shedding. If the growth rate is smaller than the re-circulating flow time scale, the cavity at the aft portion would be pinched off. If the growth rate is closer to the advection time scale, a bubbly shock wave induced shedding would result.

In the case of re-entrant flow, the adverse pressure gradient sets the time scale of the re-entrant flow mainly due to the virtue of the geometry. In the case of a shock induced shedding, the adverse pressure gradient plays a role in setting up the downstream pressure that drives the condensation shock wave into the cavity. It should be noted that for this geometry the pressure variation in the *'s'* direction was quadratic. From a cavitation standpoint, any changes in pressure will affect the cavity length variations by $1/s^2$ which dictates the cavity growth rate process. This way, the adverse pressure gradient plays a role in setting the vapour production process too. Thus, it plays a crucial role in causing periodic shedding of vapour clouds.

8.10 Chapter Summary

1. Simple 1-D bubbly shock wave analysis was done to further understand the conditions necessary for the existence of condensation shocks in context of periodic shedding of

vapour clouds.

2. The analysis revealed the importance of cavity pressure and void fraction distribution on the shock speed and hence shedding. Based on the analysis and the measured values of the shock speed and void fraction flow fields, an estimate of the pressure rise across the shock wave was made for comparison with experimental measurements.
3. Experimental measurements of averaged static pressure revealed that the wedge apex pressure is close to vapour pressure for all speeds upon inception. The averaged cavity pressure increased with increase in flow speed and inlet pressure.
4. Experimental measurements of dynamic pressure using flush mounted transducers revealed that the pressure increase across shock waves followed the trend suggested by bubbly flow analysis. The values of the measured pressure did not match values predicted by the analysis.
5. Estimated values of cavity pressures for shedding cavities were found to be much higher than the vapour pressure. Upon looking at the cavity growth rate it was found that the time scales involved in vapour production was in the same order as the convective time scale suggesting lesser time for the cavity to reach vapour pressure.
6. Analysis of cavity growth rate revealed the importance of vapour generating rates in the initiation of shocking process. It was found that shock induced shedding was a result of rapid growth in cavity vapour content, hence void fraction and reduced speed of sound. This is resulting in the production of shock waves at the aft of the cavity that produced shedding. For the case of re-entrant flow induced shedding the cavity growth rates were not as high as that observed for shock wave induced shedding of vapour clouds.
7. The role of adverse pressure gradient at cavity closure is immense for both re-entrant

induced shedding and shock induced shedding.

CHAPTER 9

Conclusions on Bubbly Shock Propagation as a Cause of Sheet to Cloud Transition of Partial Cavitation

Partial cavitation and its transition to cloud cavitation is an important source of performance deterioration and surface erosion in marine propellers. Understanding of the mechanisms of transition and shedding can aid in the better design of marine propellers. Dynamics of partial cavitation on a wedge was studied to understand the mechanisms of transition from stable to shedding cavities. The nature of the type of cavities observed in the geometry was studied experimentally using time resolved X-ray densitometry and synchronized surface pressure measurements. In addition, cavity shapes for the present geometry using Free-streamline theory was predicted to aid in the understanding of observed dynamics and its resemblance to simplified flow physics. It was found that experimentally observed variation of cavity length and thickness with inlet cavitation number matched the analytically predicted trend overall. This suggested the dependence on governing physics of integral conservations of mass and momentum with a constant pressure cavity. The experimentally observed cavity length for stable and transitory cavitation matched the cavity length predicted by free-streamline theory until the point of maximum thickness. The cavity begins to break up in the adverse pressure region resulting in

smaller length than the analytical solution. For shedding cavities, the maximum length at a given cycle matched the cavity length predicted by free-streamline theory, suggesting the closeness to a shape resembled by a constant pressure boundary. This observation suggests the tendency of the cavity to attain the shape that is warranted by constant pressure boundary which is in equilibrium with the underlying flow, until the point of maximum thickness.

Further investigation of the void fraction flow fields was done using X-ray densitometry and high-speed videos for different cavitation numbers and flow speeds. The resulted revealed the presence of stable, intermittently shedding and periodically shedding cavity. Variation of inlet speed did not have an appreciable effect on the void fraction flow fields. Examination of shedding mechanisms of transitory cavity reveals two mechanisms of shedding: Re-entrant flow induced mechanism and condensation shock wave induced shedding. For periodically shedding cavities, the dominant mechanism of shedding was the propagation of condensation shock waves.

Comparison of the finding from previous studies confirmed the presence of a propagation of bubbly shocks as a physical mechanism. Shock speeds measured from void fraction flow field measurements show a trend of increasing shock speed for increasing inlet speeds. Based on pressure measurement in the cavity and the void fraction flow fields, the observed condensation shock satisfied simple one dimensional bubbly shock relations on a qualitative level.

The reason for the formation of shock process was identified to the growth rate of cavity in relation with the convective time scale. For a transitory cavity it was found that re-entrant induced shedding existing for lower values of cavity growth rate while shock wave induced shedding existed for higher growth rate. The time scales of vapour production processes play a

crucial role in type of shedding dynamics observed. Adverse pressure gradient at the aft of the cavity plays an important role is setting up both the vapour production time scales and the re-entrant flow time scales. The identified mechanism can be tested by injecting non condensable gas into the cavity, which will alter the vapour production mechanism and hence the observed shock dynamics.

CHAPTER 10

Stationary Cavitation Bubbles Incepting in Delta Wing Vortices

10.1 Background

This chapter provides a background on the scientific framework of vortex cavitation on lifting surfaces. The fluid dynamics of the delta wings at high attack angles in general is reviewed including the phenomena of vortex breakdown. With the necessary background, the problem is the then described to fully understand the uniqueness, and the impact of studying vortex cavitation on delta wings. Cavitation occurs in liquids when the local pressure is close to or less than the vapour pressure of the dissolved gases is realized in certain parts of the flow. Dissolved gas could include the vapour of the liquid in which case the vapour pressure dictates the phenomena. There are many instances of flow situation when the local pressure is close to or less than the vapour pressure. If a site capable of inception, *i.e* a nuclei (pockets of dissolved gas/vapour), is available, cavitation may result characterised by the presence of a gas bubble/pocket/region in a liquid flow.

Vortex cavitation is characterised by the presence of cavitation bubbles in the low pressure cores of vortices. Such vortices can occur in separated regions of shear flow, trailing vortices from lifting surfaces, propeller tip vortices, and wakes. Trailing vortices shed from lifting surfaces such as hydrofoils can experience vortex cavitation when the core pressure is sufficiently low

provided a nucleation site capable of inception is available. Once incepted, these bubbles grow in volume, before finally collapsing when flown into a region of high pressure. A good review of vortex cavitation in general can be found in Arndt (2002). Figure 1 shows vortex cavitation on a tip vortex. The presence of a cavitation bubble that fills the vortex core can be clearly seen. Such bubbles are one of the several types of cavitation bubbles that can occur in a trailing edge vortex.

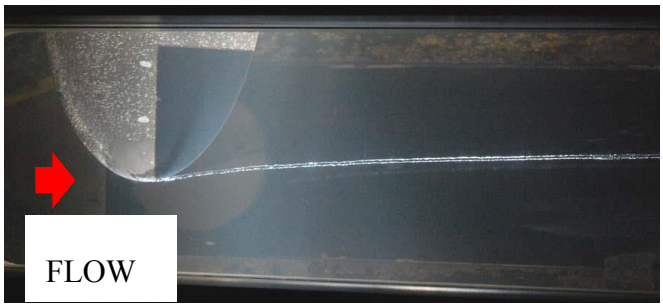

Figure 10.1: Tip vortex cavitation on a hydrofoil

10.1.1 Importance of vortex cavitation

Vortex cavitation phenomenon is important for several reasons. From an engineering perspective, it plays a crucial role in the design of turbo machineries such as propellers, and also underwater vehicle configurations such as submarines. In the former case, the onset of tip vortex cavitation on propeller tips is accompanied by performance breakdown and noise generation, which is detrimental to effective usage. In the case of submarines, the presence of the cavitation bubbles in the vortices shed from lifting and control surfaces leads to noise generation which makes detection possible. Thus vortex cavitation provides many adverse effects that a good understanding of its onset, behaviour, and control is necessary for effective design.

From a scientific perspective, vortex cavitation provides unique conditions to study cavitation bubble dynamics in a varying pressure field. Observations of the bubble dynamics can reveal

important information about the underlying vortical flow field, and if understood properly can be used to a tool to measure or quantify the vortical flow field. Finally, the interaction between the bubble and the vortex can also aid in the understanding necessary to achieve control.

10.1.2 Role of average vortex properties

Since vortex cavitation depends on the value of the pressure in the vortex core, many studies have been done to understand the effects of individual vortex properties such as circulation, tangential velocity distribution on vortex cavitiation, mainly cavitation inception. Cavitation inception is defined as the first occurrence of a cavitation bubble in a previously non cavitating flow field. The occurrence of vortex cavitation on trailing vortices from hydrofoils has been extensively studied by researchers such as McCormack (1954), Green (1991), and Fruman *et al*. (1995)

Arndt *et al.*(1991) observed cavitation events on an elliptic hydrofoil using photography and visual detection. In their study, it was found that cavitation bubbles incepted at a location further downstream of the wing tip, before convecting into the region of high pressure to collapse. They found that free stream cavitation inception number ($\sigma_{\infty,i}$) did not match the minimum pressure ($-C_{p,\min}$) estimated from measured velocity profiles using LDV ($\sigma_{\infty,i} \neq -C_{p,\min}$), and other factors such as water quality should be taken into account. Fruman *et al.* (1992) studied the effect of Reynolds number on cavitation inception on trailing vortex from a hydrofoil, and conducted valuable measurements on the structure of the tip vortex in the vicinity of the tip. They found that desinence cavitation number matched the estimated minimum pressure obtained using the tangential velocity profiles. Thus, the vortex properties play a very important role in the estimation of both the occurrence and type of vortex cavitation.

10.1.3 Vortex cavitation bubble dynamics

Once incepted, the dynamics of cavitation bubbles is dictated by the surrounding flow field. Dynamics of vortex cavitation bubbles has also been studied previously. Vortex cavitation bubbles are non-spherical, elongated, and subjected to the disturbances from the underlying vortical flow. Choi and Ceccio (2007) studied the bubble inception, growth, and collapse of laser induced bubbles in a tip vortex core for different attack angles, and surface roughness. They compared the observed shapes and bubble dynamics to non cavitating vortex properties measured using Stereo Particle Image velocimetry. They found that even though the single phase pressure field is uniquely scaled by the vortex core radius and circulation, they are insufficient to scale the bubble dynamics and the radius. A numerical study by Choi *et al.* (2009) revealed that the final bubble shape depends upon the details of the bubble formation process, such as the bubble growth rate which depends upon the size of the nuclei. As far the understanding the bubble dynamics is concerned, there is much more scope to answer specific questions as to what sets the dimension of the bubble radius.

10.1.4 Vortex cavitation bubble acoustics

Vortex cavitation bubbles are susceptible to changes imposed by the underlying vortical flow, and this makes them emit acoustic pressure tones. They have been observed to emit tones at particular frequencies, referred to as *chirps* by Chang and Ceccio (2011), based on the audible noise they produced as a result of transient vortex bubble inception. This sound is in contrast to the impulsive *popping* noise created upon bubble growth and, especially, collapse, which is a noise emission characterised with a sharp broadband peak. Chirps are much longer in duration than a pop, and it contains a well-defined tone when compared to the broadband pop. The

physical origin of the chirping sound has been discussed by Choi *et al.* (2009) and experimentally examined for bubbles produced by the unsteady vortex stretching by Chang and Ceccio (2011). Vortex cavitation bubbles present in the vortex core can undergo radial volume oscillations that occur with a period that is related to the vortex time scale $\tau_V = 2\pi r_C / V_\theta$ where r_C and V_θ are the (non-cavitating) vortex core radius and maximum tangential velocity. Numerical study by Choi and Chahine (2004) discusses the different scenarios of bubble collapse by deformation depending upon the proximity to the inception cavitation number, and its significance on the noise generated.

10.1.5 End of section note

All the studies that have been reported so far have been on trailing tip vortices, which are different from the delta wing vortices. The present study examines the inception, dynamics, and noise emission of individual vortex cavitation bubbles in the leading edge vortices produced by a delta wing at finite attack angle.

10.2. Delta Wing Vortex

Delta wing is a lift generation device, producing a significant portion of the lift due to leading edge vortices. Delta wings with sweep have been employed at high attack angles to facilitate the design of high manoeuvrable fighter aircrafts. There are many distinct features of a delta wing leading edge which are described below. The strength of the leading edge delta wing vortex continues to grow as vorticity is shed from the delta wing is rolled up, producing strong *axial gradients* in the vortex core size, core axial velocity, and circulation. The circulation gradient due to roll up and pressure gradients in the outer flow produces an axial jetting in the vortex core that continues to increase in magnitude along the axial direction. When the ratio of the maximum

tangential velocity to the axial jetting velocity (swirl number) exceeds a critical value, vortex breakdown occurs, and the breakdown location depends on the attack angle (Figure 2). A very informative review about the aerodynamics of delta wings can be found in Nelson and Pelletier (2003).

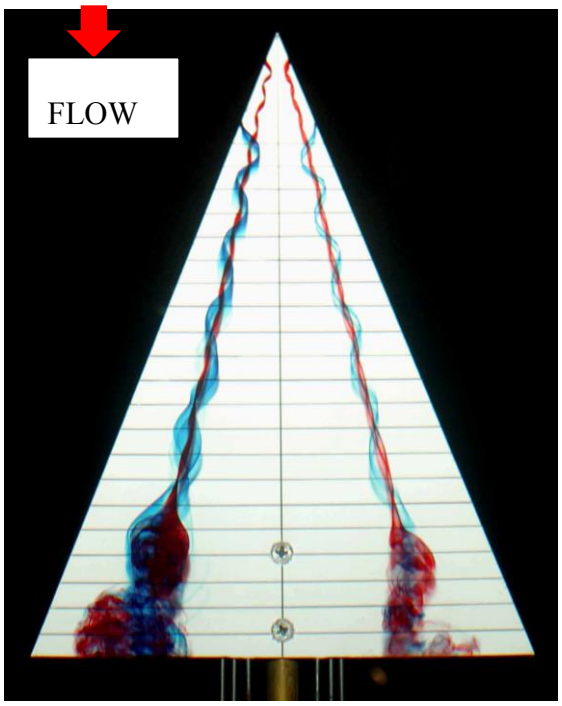

Figure 10.2: A delta wing vortex experiencing vortex breakdown (Source: serve.me.nus.edu.sg)

10.2.1 Delta wing vortex breakdown

A delta wing vortex breakdown can be of spiral type or bubble type. For delta wings with sharp leading edge, the breakdown phenomenon is independent of Reynolds number. Delery (1994) discusses the different aspects of vortex breakdown in general, with a chronological study on vortex breakdown in delta wings. The theory of vortex breakdown is also well developed and a good flavour can be obtained from Wang and Ruzak (1997), Keller *et al.* (1992), Darmofal *et al.* (2001), and Delery (1992). Rusak and Lamb (1999) computed the location of breakdown predicted on a delta wing by their theory using experimentally measured velocity profiles, and

found it to match very well with observed locations. Experimental observations of vortex breakdown location by other researchers revealed an oscillatory behaviour about a mean position with a maximum magnitude of about 0.25 C (Payne *et al.* (1986, 1988) & Mitchell *et al.* (2000)).

10.2.2 Delta wing flow field

Experimental measurements of axial and tangential velocity profiles at different axial locations on delta wing vortex with a 70 degree sweep back have been performed by Visser and Nelson (1993). They also propose a scaling of vortex properties with attack angle. Payne *et al.* (1986, 88) with the aid of flow visualization using smoke injection identified the presence of secondary vortex structures in a delta wing flow.

10.2.3 Similarities and differences with wing tip vortices

From a vortex cavitation perspective, the vortical flow in a delta wing is similar, yet different from that of a tip vortex. Experiments by various researchers, like Francis and Katz (1988), Green and Accosta (1991), Fruman *et al.* (1992), show that a tip vortex is considered rolled up, i.e. there are no appreciable changes in the flow properties along the axial direction due to roll up processes, with a few chords downstream of the tip. Green (1995) discusses the process of roll up in a tip vortex and its associated flow field. However, a delta wing vortex is never completely rolled up. Thus, vortex cavitation on a delta wing vortex may be similar to tip vortex cavitation *only within the region of rollup*. The role of flow unsteadiness in the roll up process of a delta wing is as substantial as it is for a tip vortex.

The axial gradients of flow properties in a rolled-up tip vortex are much lesser in magnitude, and of opposite sign than that of delta wing vortices, whose strength increase along the downstream direction. For tip vortices, the axial location of the point of minimum pressure can be located

very close to the leading edge, as close as 0.20 C measured by Fruman *et al.*(1992) , where is C is wing chord, with the pressure gradually increasing or remaining the same along the axial direction. Thus, any nucleation site that incepts in the rolled up region would be convected downstream to a region of higher pressure, with its growth rate depending upon a nearly constant or a *monotonically increasing* core pressure along the axis. However, in a delta wing experiencing vortex breakdown, the axial pressure keeps dropping from the leading edge along the axis to reach a minimum value before the breakdown location. This provides a different condition for the cavitation dynamics, for, a nuclei incepting in the vortex core would be subject to a monotonically decreasing pressure along the axis, until the breakdown location, where the pressure increases abruptly. Oscillation of the breakdown location can also have an effect on the bubble dynamics of cavitation bubbles.

Thus, the flow field in the present study has many interesting flow features for studying vortex cavitation bubble dynamics in a setting that has not been studied before.

CHAPTER 11

Experimental Setup

11.1 Flow Loop

The experiments were conducted in the University of Michigan, mini Large Cavitation Channel (MLCC), a 1:14th scale model of the Large Cavitation Channel at Memphis, Tennessee. A complete description of the MLCC is provided by Shen *et al.*[25]. The MLCC has a 6:1 contraction section, followed by a 1.18 m (length) x 0.22 m x 0.22 m (width and height) square test section with 45° corner fairings, and a 1.85 m long diffuser section. The tunnel test section pressure can be varied to produce different test section cavitation numbers, σ_∞ where

$$\sigma_\infty = \frac{(P_\infty - P_V)}{(1/2\rho V_\infty^2)} \qquad (11.1)$$

Here P_∞ is the free stream static pressure, P_V is the vapour pressure of water, ρ is water density, and V_∞ is the free stream velocity. The tunnel was equipped with a de-aeration system, and the dissolved oxygen content was kept constant for all tests and it was around 15% of saturation at atmospheric pressure. The flow speed V_∞ was fixed at 4.0 +/- 0.2 m/s by setting the propeller r.p.m to a value that corresponded to the flow velocity without the model. The free-stream pressure was measured at pressure taps at the entrance of the test section. A Solar Metrix

pressure gauge was employed to measure the static pressure in the test section with an uncertainty of +/- 1%. The test section static pressure was varied between 70 kPa < P_∞ < 180 kPa, and the water temperature was maintained at 20 +/- 2 C. The free-stream cavitation number therefore varied between 10.0 < σ_∞ < 19.0 with a nominal uncertainty of +/- 0.2.

11.2 Delta Wing Model

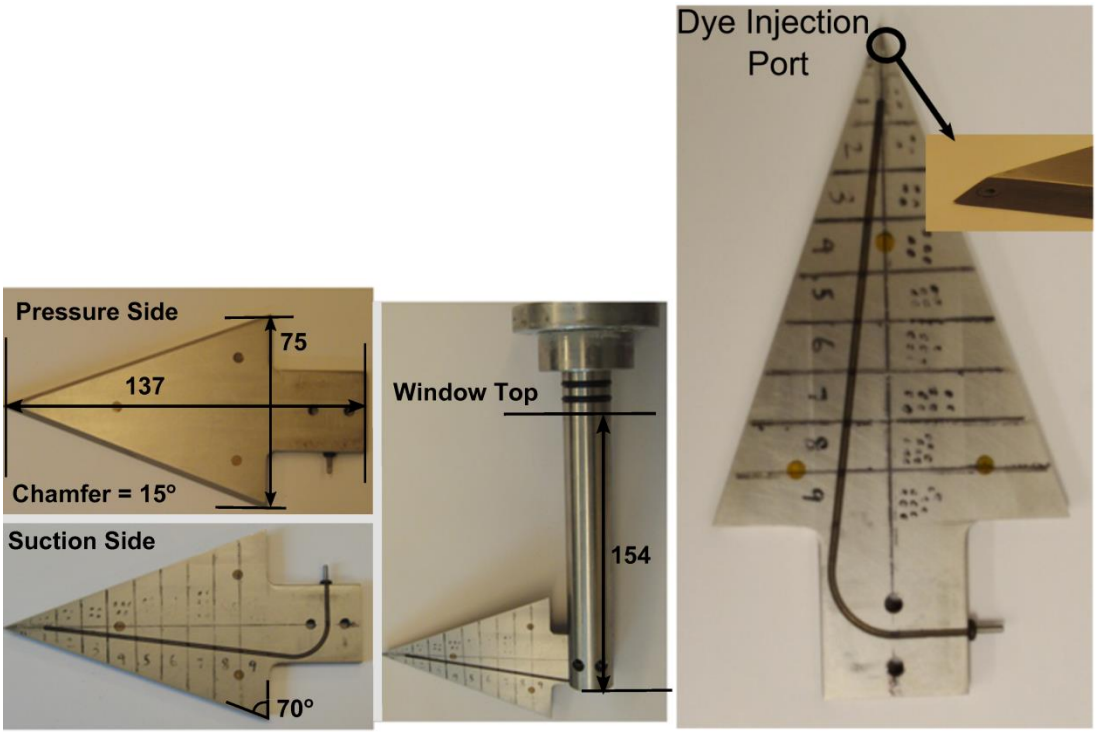

Figure 11.1: Delta wing model

Two delta wing models were used that each had a sweep back angle Λ = 70 degrees with a 15-degree chamfer on the pressure side leading edge. Figure 11.1 shows test model, dimensions and the mounting mechanism. The model used for cavitation dynamics, and observation study had a dye injection port, and was mounted from the top window. The mounting sting was aft of the top half of the model when viewed from the side. The model used for acoustic studies did not have a

dye injection port, and was mounted from the bottom window. For this case, the mounting sting was aft of the lower side of the model. The reason for using a different model for the acoustic study was the need to have the hydrophone mounted on the top window.

The model chord, C, was 100 mm, and the span at the model base was 73 mm. The test models were 6 mm thick. The models were mounted at the base with a sting support that permitted variation of the attack angle, α. The first delta wing and the sting mounting mechanism are shown in Figure 1. Ten markings spaced 10 mm, beginning from the leading edge were made on the suction side of the delta wing to help in the localization of the bubble inception, life events, and collapse. The data was collected for attack angles of α = 30, 37, and 45 degrees, which corresponds to area blockages of 8, 9, and 11%. However, a fixed free-stream velocity of 4 m/s is used to scale the results below.

The bubble dynamics model was instrumented with a dye injection port to permit visualization of a single leading edge vortex and the location of vortex breakdown. The embedded tube had an inner diameter of 1.6 mm, and it was placed near the expected location of vortex detachment. Injected dye was a mixture of milk, alcohol, and fluorescein. Dye was delivered to the model via a syringe pump at a flow rate 10 mL/min.

11.3 Imaging System

A Phantom high-speed video camera (Vision Research), model number V710 was used to observe the vortex cavitation events with Nikon optical lenses of 105 mm focal length. Two 200 Watt Arrilux lamps were used to record time-series images of cavitation events at a frame rate of 7000 frames per second for the top vortex cavitation studies, and 23000 frames per second for the acoustic study. The camera was mounted such that the markings made on the model, mounted

at an attack angle, was clearly visible with minimal to no distortion. This enabled the estimation of the physical dimension of every pixel to be 0.104 mm.

11.4 Acoustic Measurements

The noise emitted by the vortex cavitation bubbles was measured with a Bruel and Kjaer hydrophone model 8103. The hydrophones were mounted on the Lucite windows of the water tunnel test section. The Lucite window had a pocket of quiescent water where the transducers were placed separate from the main flow by a 12 mm thick Lucite plate. The approximate distance from the visualized vortex cavitation to the hydrophone was 120 mm. The hydrophone signal was amplified and filtered using a Bruel and Kjaer charge amplifier Model 2635. The signals were further filtered using Krohn-Hite filter model number 3944, set to high pass with a cutoff frequency of 750Hz. A Stanford DG535 delay generator was used to trigger a data acquisition system, and the video camera, based on the filtered signal to enable time synchronization. The time series of the hydrophone output were recorded at 500 kilo-samples per second over a period of one second in single acquisition mode *via* a National Instruments analog to digital converter (model PCI-MIO-16E-4) and LabVIEW. Note that the delta wing produced two similar (but not identical) leading edge vortices, and both were capable of producing vortex cavitation noise. For the acoustic study, the cameras were focused on the lower vortex (*i.e.* the one farther to the hydrophone), and acoustic events that occurred on the upper vortex were excluded.

11.5 Vortical Flow Characterization

The vortical flow of the delta wing used in the present study has been well documented. An objective of the present study was to ensure that the flow was similar to previously reported

results. A parameter chosen to verify dynamic matching was the rather sensitive parameter of the vortex breakdown location, which changes with attack angle, moving upstream with increasing the attack angle, α. Dye visualization was used to determine the trajectory of the core of the leading edge vortices and to determine the location of breakdown in the present setup. Figure 11.2 shows the breakdown location using dye injection for a speed of 4 m/s at an attack angle of 37 degrees. Figure 11.3 presents the observed location of vortex breakdown, X_{BD}, measured from the trailing edge. The data compared well to those of several studies summarized by Delery (1994) measured for geometrically similar delta wings, despite small difference in setups, detailed model geometry, and test section blockage ratios.

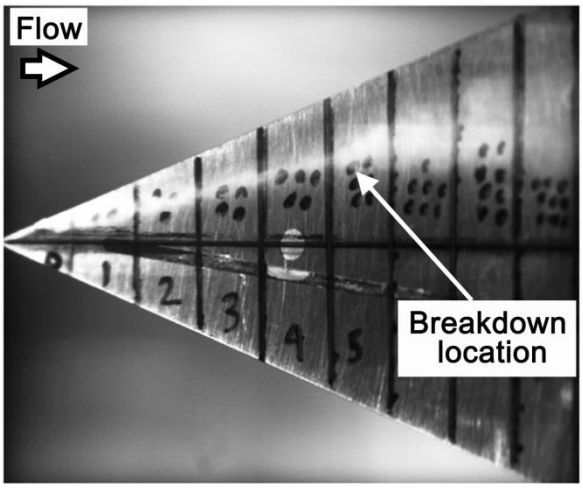

Figure 11.2: Image of a vortex forming on the suction of the delta wing that is visualized with dye injection. The core of the vortex is well defined until the position of vortex breakdown at roughly 40% chord

The flow field data reported by Delery (1994), Payne *et al. (*1986, 1988), Rusak and Lamb (1999), and Visser and Nelson (1993) were used to aid in the understanding of the vortical flow field and resulting cavitation. They examined flows over a geometrically similar delta wing with Λ = 70 degrees, and the data for α = 28 and 30 degrees show that, as the leading edge vortex develops on the delta wing, the circulation grows along the axis of the vortex, with maximum

circumferential velocities on the order of 1.5 to 2.0 times V_∞. They also found that the axial jet had a maximum velocity on the order of $3V_\infty$, and the vortex core radius, r_C, scaled with the downstream location along the vortex axis, *X*, as roughly $r_C / X \approx 0.15$.

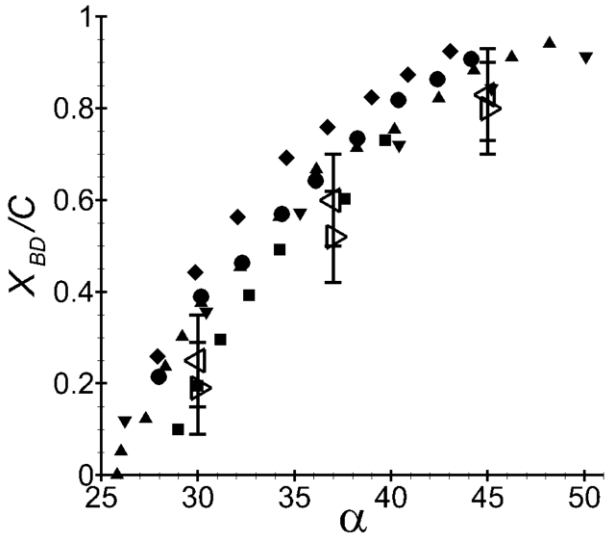

Figure 11.3: The observed average location of vortex breakdown, X_{BD}, with a nominal uncertainty in X_{BD} /C of +/- 20%, as a function of attack angle, α, for the current experiments top vortex (▷), bottom vortex (◁). These data compared well to those of several studies summarized by Delery (1994) and measured for a geometrically similar delta wings, despite small difference in setups, detailed model geometry, and test section blockage ratios. Earnshaw (1964) (■), Payne et al. (1988) (●), Ericksen (1980) (▲), McKernan (1983) (▼), Molton (1992) (♦).

Payne *et al. (*1986, 1988) used flow visualization to show that that the roll-up of the shear layer into the leading edge vortex is accompanied by the formation of secondary vorticity forming in the layer itself. They also showed that there are substantial fluctuations of the axial and tangential velocity components in the vicinity of the leading edge vortex core both prior to and after breakdown (which peaks at around 25% of the free-stream speed). These observations imply that it is meaningful to consider both the average and time varying pressures that can be

generated near the vortex axis.

CHAPTER 12

Cavitation in Delta Wings

Cavitation inception can occur when a nucleus is captured by the vortex and convects into a region of sufficient tension to promote explosive volume growth. The location of cavitation inception in vortex core of the delta wing depends upon the pressure distribution in the vortex core, the free stream pressure magnitude and the nuclei distribution. The attack angle dictates the pressure distribution while the dissolved oxygen content measures the available nuclei size distribution. Thus the third parameter, free stream cavitation number, was varied to observe different type of cavitation events on the delta wing.

The free stream pressure was fixed to a value that resulted in no observable cavitation on either of the delta wing vortex cores. With a gradual reduction in free stream cavitation number, more cavitation events were observed in the vortex core. It should be mentioned that in the experiments, inception did not occur simultaneously on both leading edge vortices, because the two vortices were not of the same strength.

Figure 12.1 (a) – (d) shows an image of the two developed cavitating vortices for α = 37 degrees and σ_∞=15. The raw photographic images, Figure 12.1 (a) and 12.1 (b), were post processed using Adobe Photoshop to facilitate a better visualization of the cavitation bubble. The cavitation bubble shape was traced using a simple lasso tool on a WACOM tablet to isolate the bubble from

the background. The opacity of the isolated background was then changed to 40% to aid the visualization of the vortex cavitation bubble. Figures 12.1 (c) and 12.1 (d) represent such processed images.

Note that bubble leading edge position is different on both the vortices, with the bottom vortex bursting before the top vortex, suggesting that the bottom vortex is stronger than the top. However, it should be noted that vortex breakdown location is unsteady, with maximum variations of about +/- 0.2 C, meaning that burst location from a still picture cannot be used to infer any information about the vortex strength. A better indicator of the strength is the inception pressure and it was found that the top vortex incepted at slightly higher pressures that the bottom, showing it to be of higher strength.

12.1 Cavitation Inception and Vortex Properties

Under ideal conditions with no nuclei dependence, cavitation inception is expected to occur when $-C_{P,\min} = \sigma_\infty$. The pressure in the vortex core $P_C(X)$ and pressure coefficient $C_{PV}(X)$, of the non-cavitating vortex can be estimated with the following expression:

$$C_{PV}(X) = \frac{P_C(X) - P_\infty}{1/2\rho V_\infty^2} \approx -k_V \left[\frac{V_\theta(X)}{V_\infty} \right]^2 \tag{12.1}$$

where k_V is a constant. For an axisymmetric Gaussian vortex $k_V = 2\eta/\beta^2 = 3.4$ with $\eta = 0.870$ and $\beta = 0.715$ (Choi and Ceccio[7]), and for a Rankine vortex, $k_V = 2$.

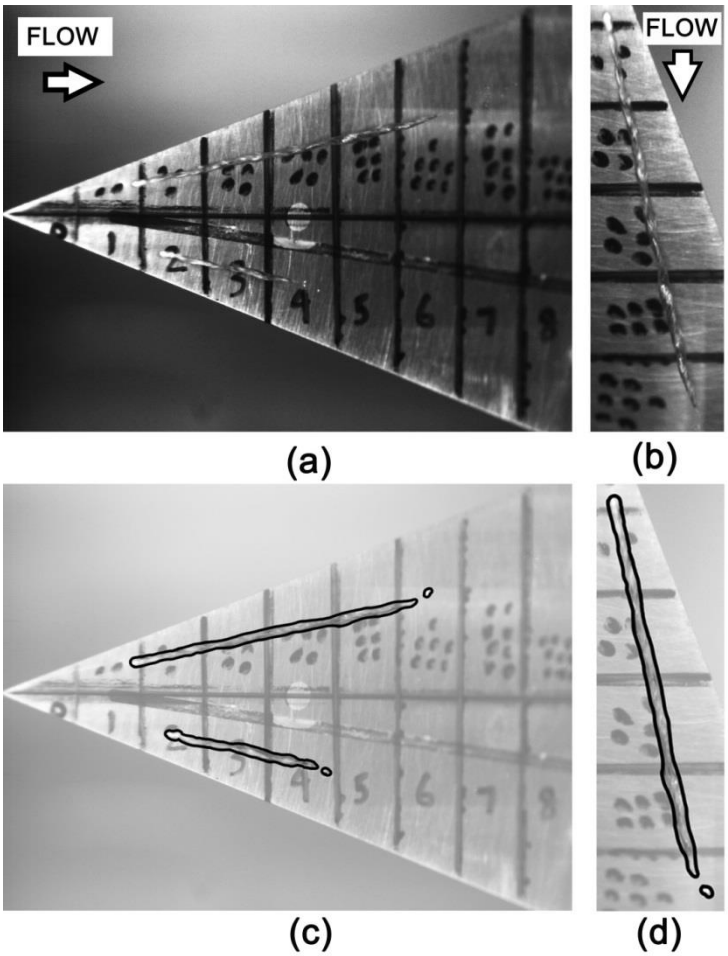

Figure 12.1: Images of the "top" and "bottom" cavitating vortices for α *= 37 and* σ_∞ *=15. 4 (a) represent unprocessed full image and 4 (b) represents unprocessed, zoomed, and rotated top vortex bubble image. Figure 12.1 (c) and 12.1 (d) are processed images of 12.1(a) and 12.1(b).*

The constants η and β combination ensures that maximum tangential velocity is attained at the core radius. This expression is for axisymmetric line vortices with slowly varying properties in the axial direction; however, the leading edge vortex of the delta wing is non-axisymmetric, is present in the separated flow on the leeward side of the wing, and evolving in the downstream direction. Nevertheless, this analysis can be used to estimate the order of magnitude of the pressure drop produced in the vortex core. Setting $V_\theta / V_\infty \approx 2$ (based on the previous flow field

observations explained in Chapter 2) and $k_V \approx 3$, one would expect $C_{PV} \approx -12$. This implies that the average core pressure would reach vapour pressure when $-C_{PV} = \sigma_i \approx 12$ at the lowest attack angle of 30 degrees, at a location near the foil mid-chord, before vortex breakdown location

Flow field data for higher attack angles have not been reported for the present geometry. But, a scaling has been proposed by Visser and Nelson (1993), suggest that the vortex strength increases as $\cos(\alpha)\tan^{1.2}(\alpha) \approx \alpha$ for the range of attack angles here. If it is assumed that the maximum tangential velocity scales with the vortex strength, it is possible to predict the time averaged mid-chord core pressures to be on the order of $C_{PV} \approx -12$, -15, and -18 for $\alpha = 30$, 37, and 45 degrees. These values give an estimate for the observance of cavitation for a given attack angle.

Yet, the *observed* values of the inception cavitation number in the experiments were much *higher* than those predicted above, even though based on rudimentary assumptions and scaling. Inception in the top vortex was observed for free-stream cavitation numbers that were typically higher than the predicted cavitation number by $\Delta\sigma_\infty = -\Delta C_P \approx 2$. Moreover, it should be noted that the nuclei content of the tunnel was altered by de-aeration process, and most of the free-stream nuclei had critical tensions on the order of at least 20 kPa (*i.e.* they were on the order of 4 microns or less, Chang *et al.* (2012)). This would mean that the minimum pressure in the vortex would need to be lower than the vapour pressure provided by $-C_{PV} = \sigma_i$. Therefore, the observed cavitation events show that the minimum pressure in the core is depressed by $\Delta C_P \approx -4$, making the observed inception pressure coefficients more like $C_{PO} = C_{PV} + \Delta C_P \approx$=-16, -20, and -22 for $\alpha = 30$, 37, and 45 degrees. This implies that the minimum average pressure

in the vortex core for given free stream pressure is *lower* than predicted by the scaling, and this reduced pressure makes the vortex more susceptible to cavitation. This is consistent with the observations of previous researchers who have observed cavitation inception to occur at pressures greater than that predicted by time averaged velocity measurements, such as Arndt *et al*. (1991) and Chang *et al*. (2012, 2011)

The difference in C_P can be partly explained by taking into account the effect of tunnel blockage, non-axisymmetric nature of the vortex, and sensitivity of a delta wing flow to scaling between models. There is no reason to conclude that the presence of cavitation inception at a higher pressure than expected in the case of a rapidly rolling up delta wing vortex, would be just due to effects such as blockage, non-axisymmetric assumptions, scaling or other discrepancies. The role of flow unsteadiness to induce instantaneous low pressures to cause cavitation inception during the roll up process, and the presence of a sting downstream of wing cannot be overruled.

After inception, with a further reduction in the cavitation number (until $\sigma_\infty \approx 15.25$ for $\alpha = 37$), more cavitation events were observed. Most of the cavitation bubbles were of "travelling" bubble nature, lasting for a very short period of time. The bubbles incepted at a given axial location, grew violently along the axis, filling the vortex core with vapour, with the growth rate being arrested at the breakdown location. The vapour within the vortex bubble often fed into the breaking vortex core following the path-lines enclosing the core into the breakdown bubble, thereby aiding in the visualization of the twisting vortex. The bubble then collapsed along the axis with the leading edge being convected into the breakdown location. Figure 12.2 depicts the life of one such bubble, from inception to collapse in a time series of processed images. Unprocessed close-up images of these bubbles is shown in Figure 12.3. Lifetime of these bubbles from inception to collapse (t_{life}) can be used to define t_b, a measure of the bubble lifetime relative

to the flow residence time based on the free stream speed, and the wing chord.

$$t_B = (V_\infty / C) t_{life} \tag{12.2}$$

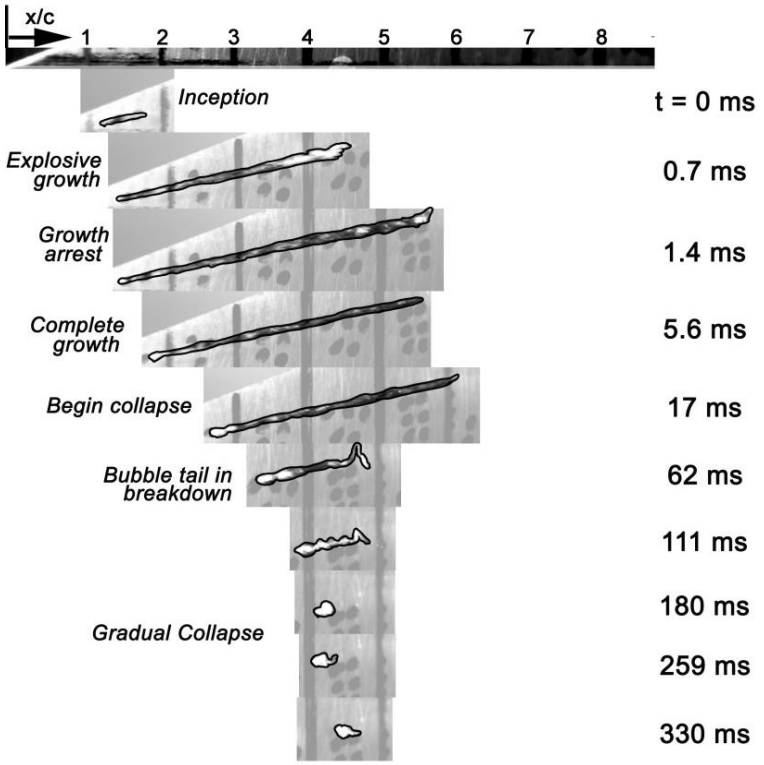

Figure 12.2: A time-series of processed images showing the inception of a single vortex cavitation bubbles forming on a travelling bubble α *= 37 and* σ_∞ *= 14.6.*

12.2 Bubble Lifetime and Type

With a further reduction in cavitation number ($\sigma_\infty \approx 14.0$ for $\alpha = 37$), a different kind of bubble dynamics, and bubble events was observed. After inception, vortex bubbles grew rapidly along the axis of the primary vortex, just like travelling bubbles. However, unlike the travelling bubbles, the leading edge of the bubbles could convect upstream or downstream from the position of inception, and continue to occupy a location for times larger than the residence time

based on the free stream speed and wing chord (t_b >>1). Bubbles that exhibit this behavior are called "stationary" bubbles. Figure 12.4 depicts the life of one such bubble, incepting at a location downstream of the point of vapour pressure along the axis, and travelling upstream to attain equilibrium. Unprocessed close up images of these bubbles is shown in Figure 12.5.

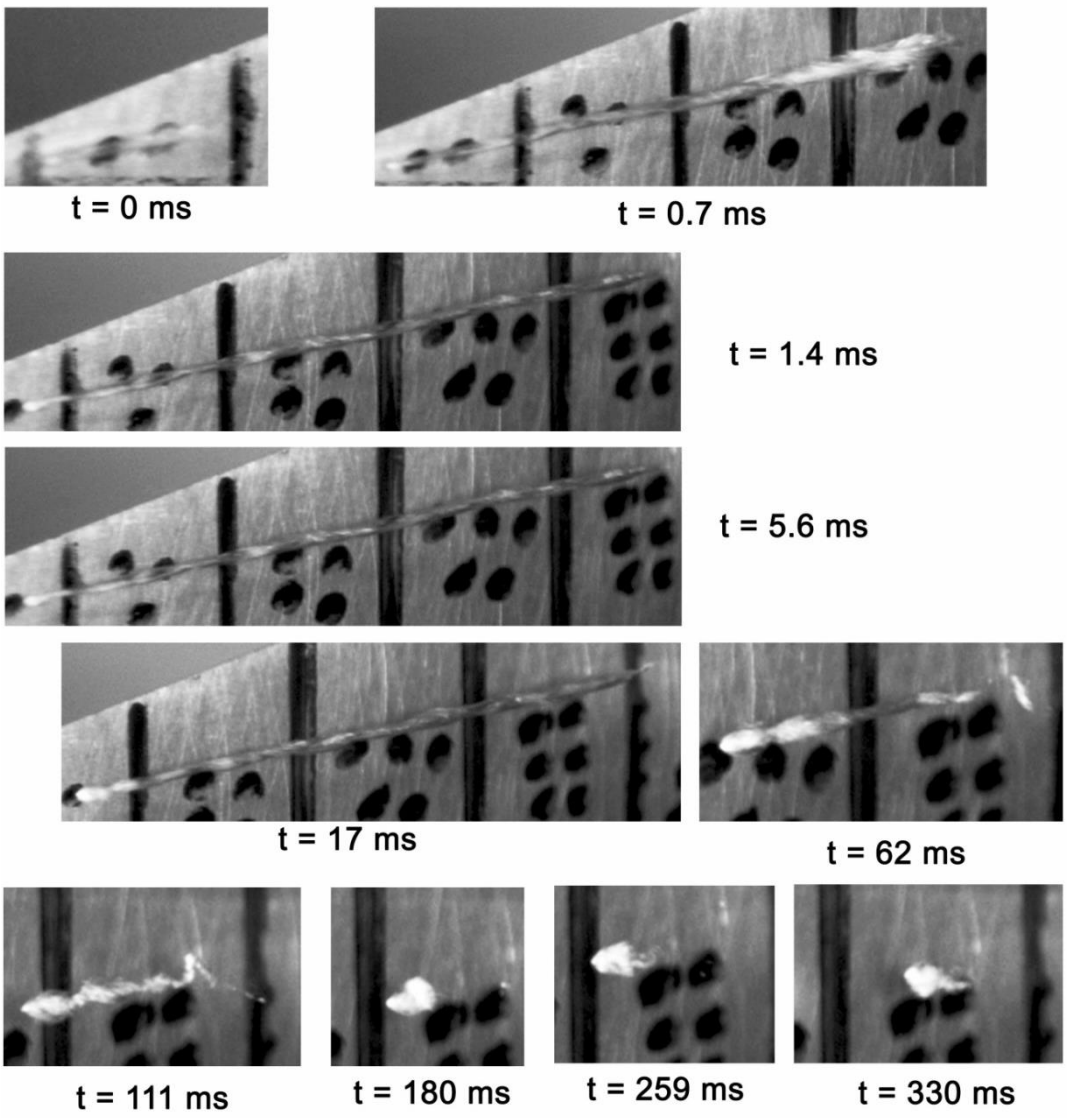

Figure 12.3: A time-series of unprocessed images corresponding to Figure 12.3, for α *= 37 and* σ_∞ *= 14.6.*

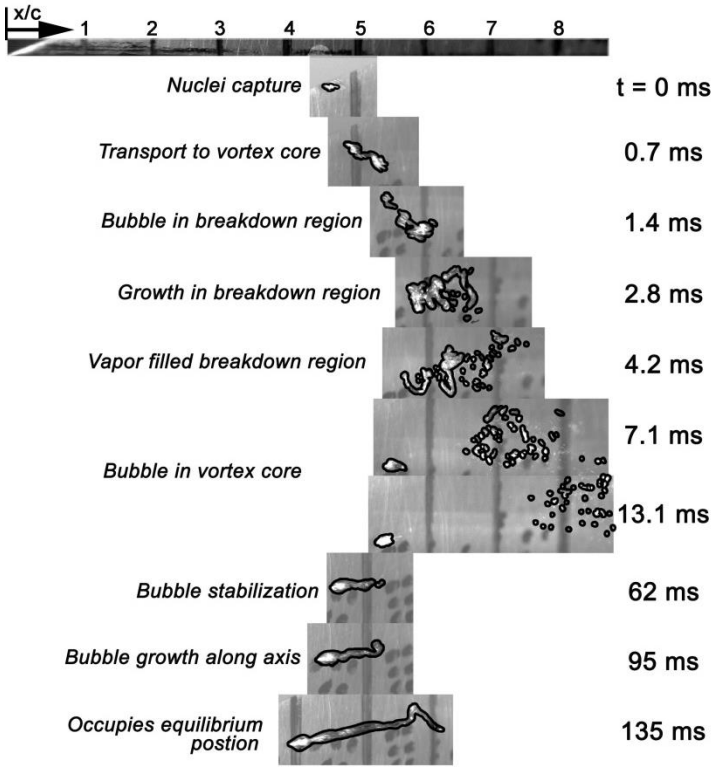

Figure 12.4: A time-series of processed images showing the inception of a single vortex cavitation bubbles forming on a stationary bubble α *= 37 and* σ_∞ *= 13.6.*

Figure 12.6 shows the plot of t_b versus cavitation number for different attack angles. Stationary bubbles lived longer than the maximum t_b, indicated by the dashed line in Figure 12.6. The bubble lives were recorded for a duration corresponding to the dashed lines which a consequence of memory constraints of the camera, except for a few cases which cross the dashed lines. Thus, the t_b cut-off in Figure 12.6 is a consequence of record length, rather than the physics. Once stationary bubbles form, they can last almost up to $t_b \sim 1000$.

From Figure 12.6, inception of short-lived bubbles is evident at the higher pressures, as explained before. With a reduction in cavitation number, a sharp rise in the bubble lifetime is observed at $\sigma_\infty \approx -12$, -15, and -18 for $\alpha = 30$, 37, and 45 degrees. Not only does this mean that the minimum pressure in the vortex core is very close to that of the vapour pressure, but also that

the minimum pressure remains close to that value for a *longer durations*. Furthermore, these values are very close to the value predicted based on the scaling using the average vortex properties of $C_{PV} \approx -12$, -15, and -18 for $\alpha = 30$, 37, and 45 degrees.

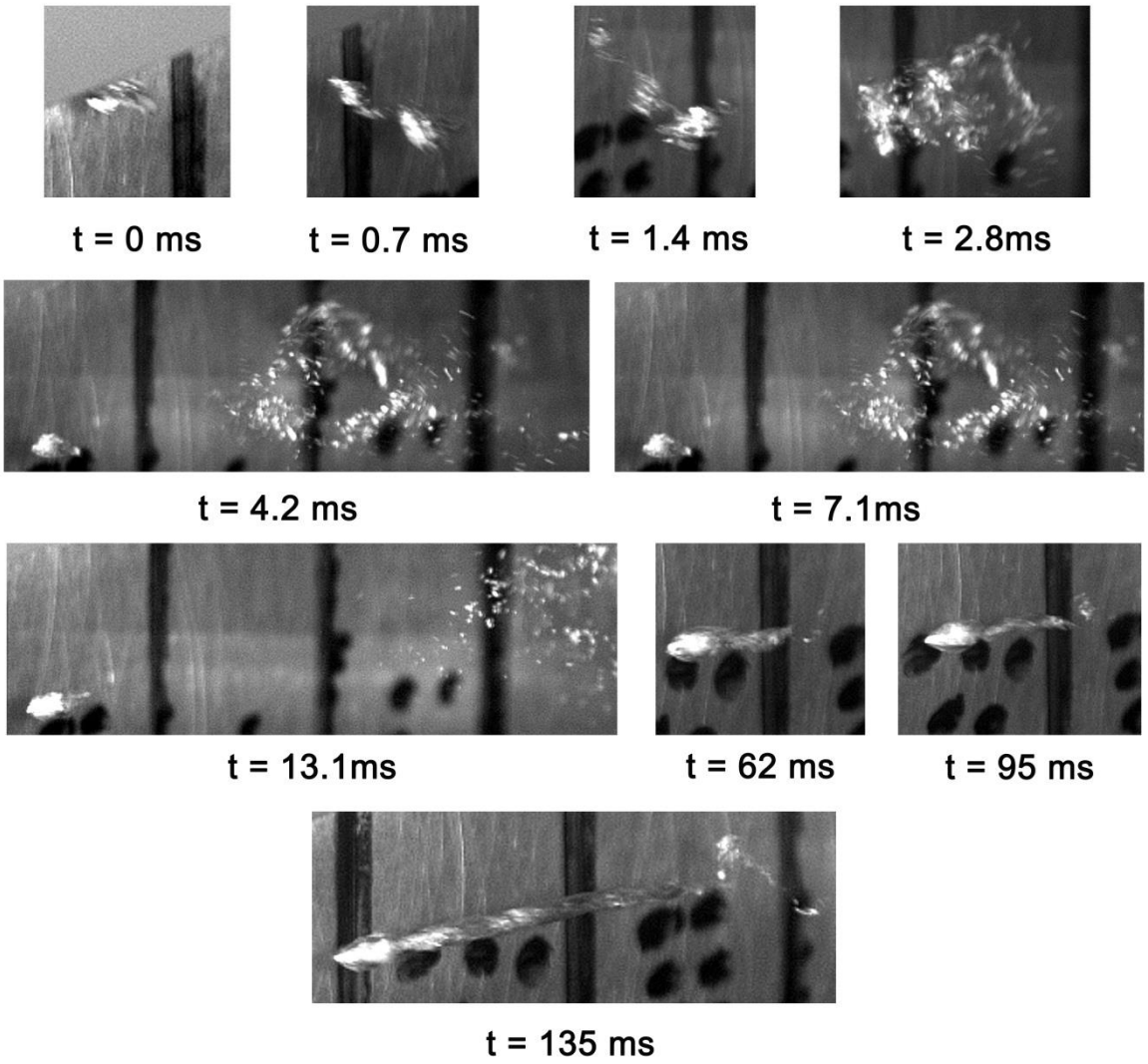

Figure 12.5: A time-series of unprocessed images corresponding to Figure 12.4, α = 37 and σ_∞ = 13.6.

These experimental observations reveal that the initially transient (*i.e.* short lived) cavitation bubbles occur as a result of transient pressure fluctuations around the vortex axis. As the free-stream pressure is further reduced, the average core pressure of the *primary* vortex falls below vapour pressure. Once this transition takes place, longer-lived bubbles can be sustained in the

primary vortex core alone. This would account for the rapid increase in the bubble lifetimes shown in Figure 12.6 as the average core pressure drops below vapour pressure for the first time.

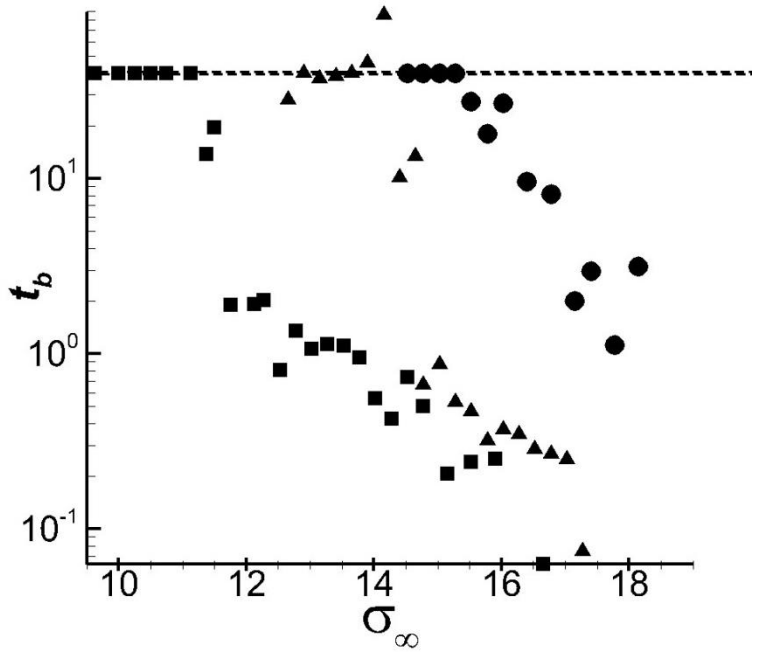

Figure 12.6: The bubble lifetime, t_B, versus cavitation number, σ_∞ , for α =30 (■), 37 (▲), and 45 degrees (●). Dashed line represent the cut off record length of the camera.

12.3 Stationary Bubbles

The leading edges of stationary bubbles after inception can occupy different positions, until they reach their equilibrium location along the axis. Sometimes, they travel upstream or downstream to a given axial location that sustains the mechanical equilibrium of these bubbles with the underlying vortex dynamics. The farthest upstream location of these bubbles for a given cavitation number correspond to the location where vapour pressure is first achieved along the vortex axis. Unlike the travelling bubble convecting into the region of vortex breakdown, there is no observable mechanism of collapse of stationary bubbles.

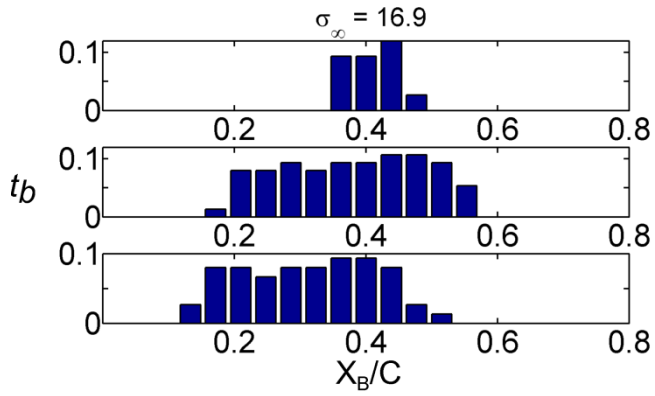

(a)

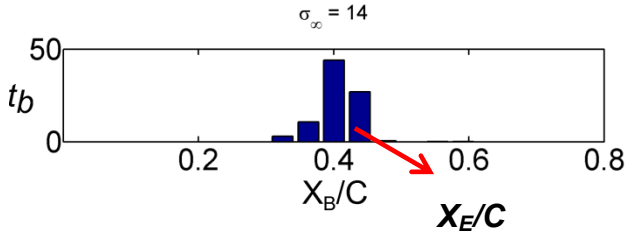

(b)

Figure 12.7: Histograms of the bubble lifetime, t_B, versus the bubble leading tip location, X_B/C, for two cavitation numbers illustrating the nature of (a) travelling vortex bubbles (σ_∞ =16.9) and (b) stationary cavitation bubble (σ_∞ =14) for α = 37 degrees.

Sometimes, the breakdown location oscillations which span +/- 0.25C produce a pressure increase that causes the collapse. The leading edges of stationary bubbles are susceptible to the changes in the rapidly rolling up vortical flow. This makes it difficult to attribute one particular position as the equilibrium bubble position from a given high speed video. Thus, the leading edge of the both the travelling and stationary bubbles, ($\boldsymbol{X_B}$), were tracked using image processing to attribute the amount of time spent along different axial locations. This result was used to plot the bubble leading edge histogram as shown in Figure 12.7 (a) and 12.7 (b). A travelling bubble

would spend nearly equal amount of time along every axial location as evident in Figure 12.7 (a). A stationary bubble would spend a maximum time around the equilibrium location ($\boldsymbol{X_E}$), as seen in Figure 12.7 (b).

Since the equilibrium bubbles seem to be related to the average vortex properties, and since the average pressure along the vortex core decreases along the axis, the location of mechanical equilibrium of stationary bubbles (X_E/C) is dictated by the vortex properties and the cavitation number. The tip location of the stationary bubbles along the vortex axis, X_E/C, moves upstream with decreasing cavitation number. Figure 12.8 presents X_E/C for different values of free stream cavitation numbers, σ_∞, showing an approximately linear relationship. The data for different attack angles collapse if σ_∞ is scaled with the cavitation number, σ_S, and the attack angle, such that $X_E/C = f((\sigma_S - \sigma_\infty)/\alpha)$. It is expected that the mean vortex circulation will increase with increasing attack angle, lowering the mean pressure in the vortex core. Hence, division by α scales this phenomenon. The scaled data is plotted as $(\sigma_S - \sigma_\infty)/\alpha = f(X_E/C)$ with $\sigma_S = 12.0$, 15.8, and 20.0 for $\alpha = 30$, 37, and 45 degrees, as shown in Figure 12.9. The values of σ_S were chosen to produce the best collapse of the data, but the values are close to the cavitation number when there is a sharp increase in bubble lifetime, discussed in the previous section. This can also be interpreted as $\sigma_i = -C_{PV} \approx \sigma_S$ corresponds to the pressure when the average pressure in the primary vortex first reaches vapour pressure. Between $0 < X_E/C < 0.1$, the scaled slope is higher for the highest attack angle. It should be noted here for higher attack angles the breakdown location was also very close to leading edge, and oscillating. This resulted in many stationary bubbles occupying an equilibrium position that were not very far apart when compared to lower attack angles.

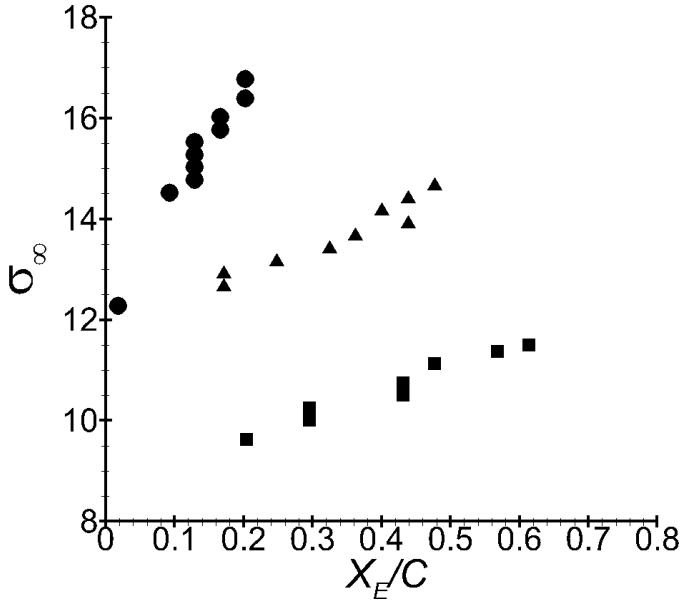

Figure 12.8: The equilibrium bubble location X_E/C as a function of σ_∞ for α =30 (■), 37 (▲) and 45 degrees (●)

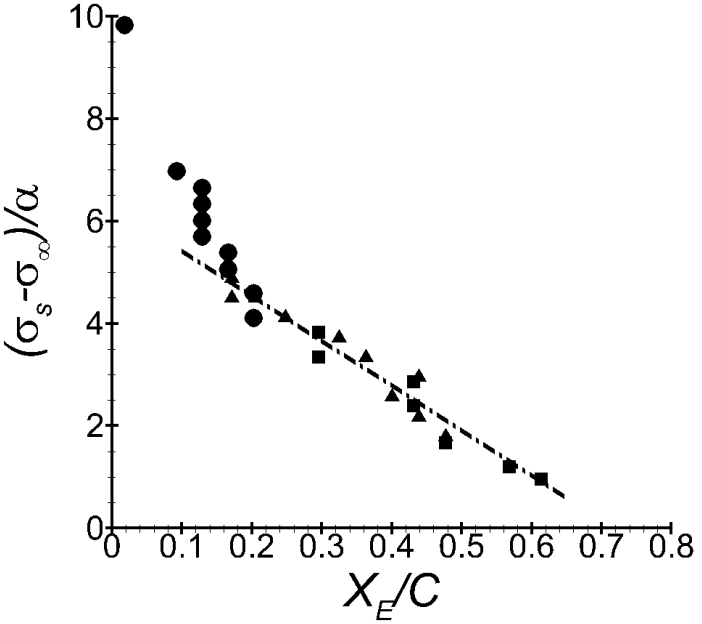

Figure12.9: Figure 12.8 data plotted as $(\sigma_S - \sigma_\infty)/\alpha$ versus X_E/C , where σ_S is the best-fit inception cavitation number given $\sigma_S \approx 12.0$, 15.8, and 20.0 for $\alpha = 30$, 37, and 45 degrees. The dashed line plots $(\sigma_S - \sigma_\infty)/\alpha = S_1(X_E/C) + S_2$, with S_1 = -8.8 and S_2 = 6.3.

12.4 Equilibrium Location of Stationary Bubbles

The presence of stationary bubbles is an interesting observation, and an explanation for their formation can be found by considering the force balance around the elongating bubble in a manner discussed by Arndt and Maines (2000) and Choi and Ceccio (2007). A work-energy analysis is conducted to relate the rate of change of kinetic energy of the elongating bubble to the bubble added mass. The bubble added mass is assumed to be related directly to the volume of the bubble and the work done by the spherical end caps of the cylindrical bubble is estimated from the bubble tension and growth rate. It should be noted that such assumptions might not hold very good for long bubbles. A simple relationship is then derived for the bubble elongation speed, $\dot{L}$, based on the tension around the tip of the bubble:

$$\frac{\dot{L}}{V_\infty} \approx k_E \sqrt{-(C_{PV}(X) + \sigma_\infty)} \tag{12.3}$$

where $C_{PV}(X)$ is the average core pressure near the bubble tip as a function of the distance along the vortex axis, and $k_E = 2/\sqrt{c_M}$ is a constant related to the added mass of the bubble, c_M. Arndt and Maines (2000) reported a value of $k_E \approx 2$ based on experimental observations of vortex cavitation in the trailing vortex of a hydrofoil, and Choi and Ceccio (2007) reported values of $k_E \approx 1$ for growing and collapsing cavitation bubble in a line vortex passing through a Venturi, although a range of values was observed, suggesting that the added mass coefficient of the bubbles was not a constant.

Fluid tension must be present upstream of the bubbles tip for the bubble to elongate. So, for the bubbles to be stationary, the elongation velocity should be equal and opposite the core axial

velocity. Then bubble tip will be stationary in the laboratory frame when

$$\frac{\dot{L}}{V_\infty} \approx k_E \sqrt{-(C_{PV}(X_E) + \sigma_\infty(X_E))} = \frac{V_C(X_E)}{V_\infty} \tag{12.4}$$

The core axial velocity is approximately related to the core pressure in an expression proposed by Batchelor (1964):

$$\left(\frac{V_C(X_E)}{V_\infty}\right)^2 \approx 1 + k_V\left(\frac{V_\theta(X_E)}{V_\infty}\right)^2 = 1 - C_{PV}(X_E) \tag{12.5}$$

Then,

$$\sigma_\infty(X_E) = [C_{PV}(X_E)(1 - k_E{}^2) - 1]/k_E^2 \tag{12.6}$$

The vortex core pressure will reduce with increasing circulation, which increases linearly in the downstream extent along the vortex axis and with attack angle:

$$C_{PV}(X) = C_{PE}\left(\frac{\alpha}{\alpha_O}\right)\left(\frac{X/C}{X_O/C}\right) = m\alpha(X/C) \tag{12.7}$$

Data for α_O = 30 degrees (0.52 radians) from Figure 9 can be used to set C_{PE} = -12 at X_O/C = 0.8, making *m* = -29, where C_{PE} is the coefficient of pressure at equilibrium location. Equations 7 and 8 yield the linear relationship between the bubble equilibrium position and the cavitation number:

$$\sigma_\infty(X_E/C) = [(m\alpha X_E/C)(1-k_E{}^2)-1]/k_E^2 \tag{12.8}$$

The best fit line of the scaled data in Figure 9(b) between $0.1 < X_E/C < 0.6$ is given by

$$(\sigma_S - \sigma_\infty)/\alpha = S_1(X_E/C) + S_2 \tag{12.9}$$

where S_1 = -8.8 and S_2 = 6.3. The predicted and measured slopes $d\sigma_\infty / d(X_E/C)$ can then be used to compute k_E necessary for bubble equilibrium:

$$\frac{d\sigma_\infty}{d(X_E/C)} = \frac{m\alpha(1-k_E{}^2)}{k_E^2} = -S_1\alpha \tag{12.10}$$

Solving for k_E yields a value of 1.2, which is close to the value observed by Choi and Ceccio (2007) of $k_E \approx 1$. Hence, the observations of position of the stationary bubbles and the change in the stationary tip location with cavitation number are broadly consistent with the simplified analysis presented here. This shows that the scaling the core pressure with an axisymmetric vortex profile is adequate to capture the most general features of the *developed* cavitating vortical flow of the delta wing vortex, even though measured vortex profiles are clearly non-axisymmetic and evolving in the chord-wise direction. However, this scaling will not capture the flow pressure fluctuations responsible for inception.

12.5 Vortex Breakdown Location and Bubble Shapes

One of the goals of the study was to find out the effect of vortex cavitation on the breakdown location. The breakdown location of a non-cavitating vortex at a given attack angle was found by dye injection. From the videos, it was found that the breakdown location of a non-cavitating flow had an r.m.s of about 0.25 C. The effect of vortex cavitation on breakdown location was studied

by injecting dye into a cavitating vortex. This showed that cavitation bubbles can be used as reliable trackers to estimate the breakdown location. Videos from cavitating vortices revealed that cavitation did not alter the breakdown location within the variation limits of the breakdown location change in a non-cavitating vortex.

Presence of a cavitation bubble in the vortex core displaces the axial flow, at the same time keeping the pressure constant along the length of the bubble. Since the bubble presence is unlikely to alter the rollup process or the wake pressure behind the wing, there is little reason for the axial flow to significantly change in magnitude along the axial direction (Batchelor (1964)). The presence of the bubble increases the core radius, thus reducing the maximum value of the tangential velocity. Since the bubble is a constant pressure surface along the vortex axis, the outer tangential flow adjusts itself to produce the pressure drop that results in vapour pressure near the bubble interface (radial equilibrium). However, as there is not significant change in the vortex breakdown location, these changes to the flow field within the vortex core do not appear to modify the vortex swirl ratio (*e.g.* the ratio of the maximum liquid tangential velocity to liquid axial velocity along the vortex core).

Figure 12.10 (a) – 10 (f) presents close-up images of both travelling and stationary cavitation bubbles, unprocessed Figures12. 10 (a) through 12.10 (c), processed 12.10 (d) through 12.10 (f). At the leading edge, the bubbles exhibit a bulbous shape. Then, the elongated bubble equilibrates to a narrower cylindrical shape. The bubble collapses at the location of vortex breakdown, which is sometimes visualized with remnants of the bubble. Keller *et al.* (1985) and Wang and Rusak (1997) show that vortex breakdown can represent a flow state transition between two states. The observations here suggest that the presence of the bubble in a delta wing vortex core could be an additional permissible flow configuration of the vortex, with bubble shape being dictated by the

process of flow state transition.

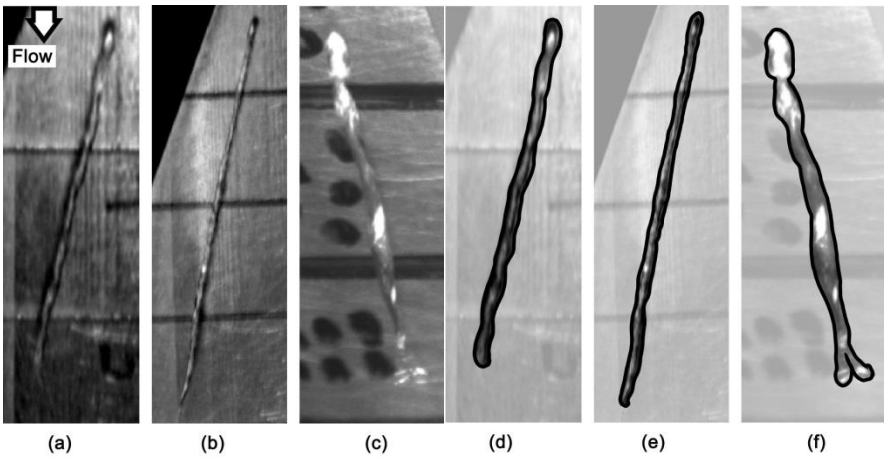

Figure 12.10: Bubble shapes (a) bottom vortex unprocessed, σ_∞ = 16.3, (b) bottom vortex unprocessed σ_∞ = 15.5, and (c) top vortex unprocessed, σ_∞ = 14.0;(d) bottom vortex processed, σ_∞ = 16.3, (e) bottom vortex processed σ_∞ = 15.5, and (f) top vortex processed, σ_∞ = 14.0;all cases are for α = 37 degrees.

CHAPTER 13

Bubble Acoustics

The vortex cavitation bubbles emit a distinct noise signal during their inception, growth along the vortex axis, impact with the region of vortex breakdown, and their steady-state volume oscillations. Stationary bubbles characterized by long lifetimes make it possible to record extended time series of their emitted sound and relate it the observed bubble dynamics. Presented below are results for $\alpha = 37$ degrees.

The acoustic measurements presented in this study are for bubbles forming on different delta wing model with same dimensions as the cavitation dynamics model. The reason for using a different model is explained in the experimental setup section. It was found that for the acoustic model, the bottom vortex was stronger than the top. The reason for the bottom vortex in the acoustic model to be stronger than the dye injection model is not known, but could be due to the presence of dye injection port on the top-side for the previous model or the mounting sting, which contributed to increased strength. For the acoustic study, cavitation on the bottom vortex was chosen since this increased the likelihood that the noise produced by incepting bubbles would not be coincident with noise from bubbles forming on the top vortex. The general behaviors of the top and bottom vortices were quite similar as the cavitation developed.

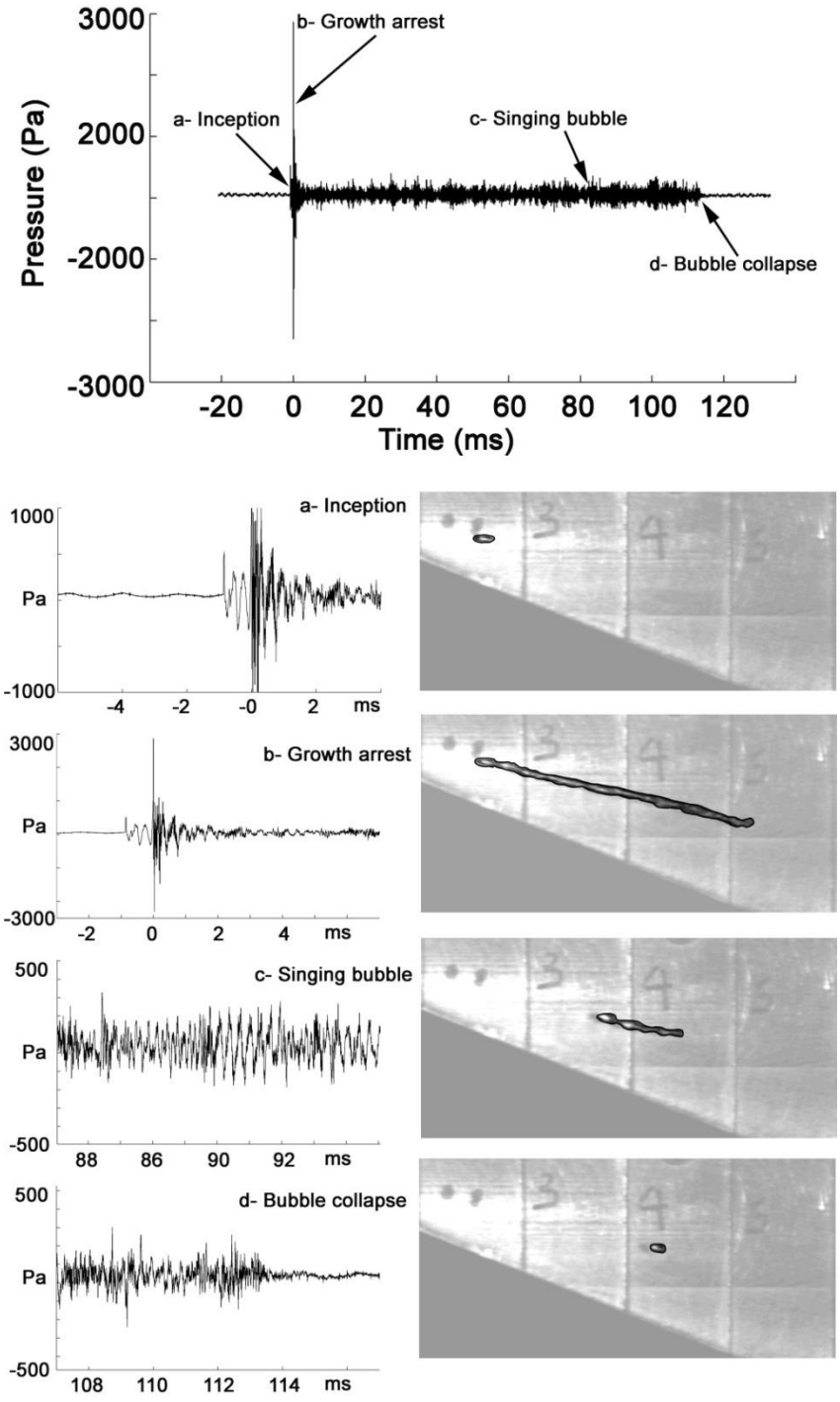

Figure 13.1: The time record of the acoustic emission of a stationary cavitation bubble for σ_∞ = 16.75 and α = 37 degrees. The bubble incepts at time less than "0" and grows along the vortex axis until the tail of the bubble reaches the position of vortex breakdown, when time is "0", creating a strong pressure pulse.

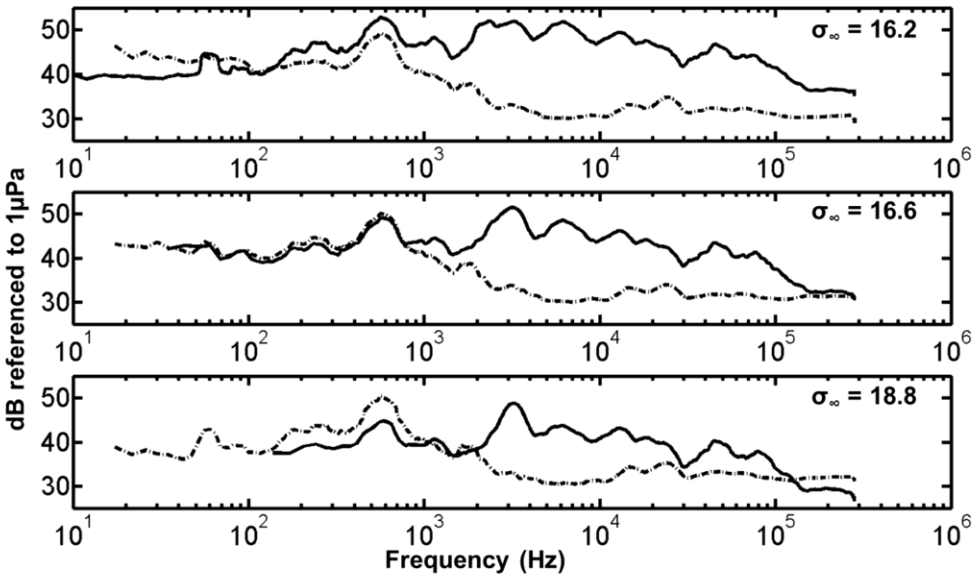

Figure 13.2: The average FFT of the acoustic signals. Solid lines represent cavitation bubble noise, while dashed lines represent non-cavitating vortex.

Figure 13.1 presents a typical whole time record of the acoustic emission, and time records in the vicinity of important cavitation events and their corresponding processed bubble images. A nucleus is captured by the vortex and leads to cavitation bubble inception, which is characterized by the impulsive pressure rise, denoted by (a). The bubble grows along the bubble axis, producing noise emission as well, which is similar to that reported by Chang and Ceccio (2011) for short-lived vortex bubbles in stretched vortices. Once the bubble impinges on the region of vortex breakdown, it experiences a sharp rise in static pressure, and the growth is suddenly arrested, leading to a second sharp impulse denoted by (b). Once formed, the long, stationary bubble reaches a nominally constant length, and it emits a distinct tonal sound (c) until the point of bubble desinence (d).

The spectrum of the *impulsive* bubble noise during explosive growth, impingement and

deceleration in the region of vortex breakdown, and (sometimes) desinence is broadband, as discussed by Choi and Ceccio (2007) and Choi *et al.*(2009). But, the tonal noise produced by the stationary bubble in equilibrium is similar to that reported by Choi *et al.* (2009) and Chang and Ceccio (2011). Figure 13.2 presents the spectra of acoustic signature (with 1/10 decade filtering) for the tonal noise signal, in the region between points (b) and (d) shown in Figure 13.1, excluding the spike at point (b). The signals were averaged over 13 bubbles with an average $\boldsymbol{t_b}$ = 32 for σ_∞ = 16.2, 13 bubbles with an average $\boldsymbol{t_b}$ = 4.41 for σ_∞ = 16.6, 11 bubbles with an average $\boldsymbol{t_b}$ = 0.93 for σ_∞ = 18.8. The background spectrum for the non-cavitating flow for all cavitation numbers is represented by dashed lines. It can be seen that the non-cavitating vortex noise has a distinct peak apparent at a frequency of ~600 Hz. The origin of this peak is not known. Solid lines in Figure 13.2 represent the spectral content of the acoustic tones emitted by both travelling and stationary cavitation bubbles. There is a definite difference in the acoustic signature with and without cavitation. It can be seen that frequencies greater than 1 kHz begin to grow, increasing with decreasing cavitation number. Strong tones are found at ~3kHz, ~6 kHz, ~13 kHz when the stationary bubble is present.

Choi *et al.*(2009) discusses the scaling of vortex cavitation noise based on the vortex timescale τ_V, as discussed in the introduction. τ_V can be estimated based on $V_\theta \approx 2.5V_\infty$ = 10 m/s, and $r_C = 0.15X$ reported by Rusak and Lamb (1999). This yields 1.5 mm < r_C < 9 mm for 0.1 < X/C < 0.6, which is an over estimate of the core size of the vortex in the present study. But, these values can be used to give an estimate of the timescales, since the actual core size is somewhere in between the above range, with the lowest core radius having the smallest timescale. The vortex timescales for above mentioned vortex properties correspond roughly to 1000 Hz

$> 1/\tau_V >$ 100 Hz. This range is consistent with the tonal peak around 600 Hz for both the cavitating and non-cavitating spectra. However, the non-cavitating vortex is not expected to be a strong acoustic source and the presence of other non-flow related sources cannot be overruled.

The tonal peaks associated with cavitating bubbles are of significantly higher frequency than that calculated from average vortex properties. Figure 13.2 reveals that the lifetime of the bubble does not influence the frequency content of the bubbles. The underlying flow is thus likely to have disturbances to be comprised of high frequency components that are faster than smallest bubble lifetime. Also, previous studies that matched the vortex timescale with the measured acoustic emission examined transient bubbles with lengths that were of order 10 times the bubble diameter. The stationary bubbles in the present study were much longer, with lengths that were on the order of 50 times the bubble diameter. Moreover, the bubbles here had relatively constant average volumes, unlike the transient bubbles of the previous studies. It should be noted that the images in Figure 3.4, 3.6, and 3.10.(a) – (f) show that elongated bubbles do not have smooth interface. Instead, the surfaces are characterized by non-axisymmetric "braids" patterns that wrap around the bubble. High-speed videos of the images show that the bubbles are not undergoing purely radial volume oscillations. The above mentioned differences from previous studies, and high speed video observations suggests that the bubble is likely exhibits volume oscillations with higher order modes, and this puts forward an explanation for the higher frequency tones.

CHAPTER 14

Conclusions on Stationary Cavitation Bubbles Inception in a Delta Wing Vortex

The present work discusses how vortex cavitation bubbles can be formed with vortices of the delta wing. In particular, we have observed elongated vortex cavitation bubbles that are stationary in the laboratory frame. These bubbles can persist for relatively long time periods, and produce a tonal noise. Such bubbles are possible since the delta wing vortex has increasing circulation along its axial extent, creating a gradient in core pressure, axial velocity, and core radius. A stationary bubble can form when there is balance between the growth-rate of the bubble tip along the vortex axis with the opposing axial jet flow. It was observed that the presence of vortex cavitation did not appear to alter the process or location of vortex breakdown.

As the vortex cavitation bubbles incepted, grew, and became stable, they emitted particular sounds related to each process. In particular, the stationary bubbles emitted a tonal noise pulse with distinct frequency peaks. The sound produced was reminiscent to that reported by Choi *et al.* (2009) and Chang and Ceccio (2011), but the noise created by these bubbles was multi-tonal and did not readily scale with the non-cavitating vortex timescale, τ_V. The cavitating flow exhibited near harmonic tones that were of much higher frequency than the frequency based on

the vortex timescale, which suggests the possibility of higher-order modes of volume oscillation producing strongest bubble noise.

REFERENCES

1. Bark, G., "Development of distortions in sheet cavitation on hydrofoils", *Proc. Jets and Cavities-Intl Symp., Miami Beach, Florida, USA*, pp. 215-225. ASME, 1985
2. Bark, G., "Development of violent collapses in propeller cavitation", *Proc. Intl Symp. on Cavitation and Multiphase Flow Noise, Anaheim, CA, USA.* ASME-FED, vol. 45, pp. 65-75, 1986
3. Brennen, C, E., "Fundamentals of multiphase flows", *Cambridge University Press*, 2005
4. Brennen, C, E.,"Cavitation and Bubble Dynamics", *Cambridge University Press*, 2003
5. Callenaere, M., Franc, J-P., Michel, J-M. & Riondet, M., "The cavitation instability induced by the development of a re-entrant jet", *J. Fluid Mech.* **444**, 223-256, 2001
6. Coutier-Delgosha, O., Stutz, B., Vabre, V. & Legoupil, S., "Analysis of cavitating flow structure by experimental and numerical investigations", *J. Fluid Mech.* **578**, 171-222, 2007
7. Crimi, P., "Experimental study of the effects of sweep on hydrofoil loading and cavitation", *J. Hydraulic*. **4**, 3-9, 1970
8. Franc, J-P., Michal, J-M.,"Fundamentals of Cavitation", Springer-Verlag, 26, 2005
9. Foeth, E-J., van Terwisga, T., van Doorne, C. & Wieneke, B., "Time resolved PIV and

flow visualization of 3D sheet cavitation", *Expt in Fluids,* **40**, 503-513, 2006

10. Foeth, E-J., van Terwisga, T. & van Doorne, C., "On the collapse structure of an attached cavity on a three-dimensional hydrofoil", *Trans. ASME: J. Fluids Engng.* **130**, 071303-1-9, 2008
11. Furness, R. A. & Hutton, S. P., "Experimental and theoretical studies of two-dimensional fixed-type cavities", *Trans. ASME: J. Fluids Engng* **97**, 515-522, 1975
12. George, D. L., Iyer, C. O. & Ceccio, S. L., "Measurement of the bubbly flow beneath partial attached cavities using electrical impedance probes", *Trans. ASME: J. Fluids Engng* **122**, 151-155, 2000
13. Glauert, H., "The elements of Aerofoil and Airscrew theory", *Cambridge Science Classics*, 1983
14. Gopalan, S. & Katz, J., "Flow structure and modelling issues in the closure region of attached cavitation", *Physics of Fluids.* **12-4**, 895-911, 2001
15. Ihara, A., Watanabe, H. & Shizukuishi, S., "Experimental research of the e ects of sweep on unsteady hydrofoil loadings in cavitation", *Trans. ASME: J. Fluids Engng,* **111**, 263-270, 1989
16. Kawanami, Y., Kato, H., Yamaguchi, H., Tanimura, M. & Tagaya, Y., "Mechanism and control of cloud cavitation", *Trans. ASME: J. Fluids Engng*. **119**, 788-795, 1997
17. Kawanami, Y., Kato, H., Yamaguchi, H., Maeda, M. & Nakasumi, S, "Inner structure of cloud cavity on a foil section", *JSME. Internation Journal.* **45**, 3, 655-661, 2002
18. Kirchhoff, G. "Zur Theorie freier Flüssigkeitsstrahlen", *Z. reine Angew. Math.*, **70**, 289-298, 1869.
19. Knapp, R. T., "Recent investigations of the mechanics of cavitation and cavitation

damage", *Trans. ASME* **77**, 1045-1054, 1955

20. Kubota, A., Kato, H., Yamaguchi, H. & Maeda, M., "Unsteady structure measurement of cloud cavitation on a foil section using conditional sampling technique", *Trans. ASME: J. Fluids. Engng* **111**, 204-210, 1989
21. Laberteaux, K., R & Ceccio, S. L.," Partial Cavity flows. Part 1: Cavities forming on models without spanwise variation", *J. Fluid Mech.* **431**, 1-42, 2001a
22. Laberteaux, K., R & Ceccio, S. L., "Partial Cavity flows. Part 2: Cavities forming on models with spanwise variation", *J. Fluid Mech.* **431**, 43-63, 2001b
23. Lange, D. F. de, "Observation and modelling of cloud formation behind a sheet cavity", *PhD thesis, University of Twente,* The Netherlands, 1996
24. Le, Q., Franc, J. P. & Michel, J. M., "Partial cavities: global behaviour and mean pressure distribution", *Trans. ASME: J. Fluids Engng* **115**, 243-248, 1993
25. Lush, P. A. & Skipp, S. R., "High speed cine observations of cavitating flow in a duct", *Intl J. Heat Fluid Flow* **7**, 283-290, 1986
26. Mäkiharju, S.A**.**, Chang, N., Gabillet, C., Paik, B.-G., Perlin, M. & Ceccio, S.L., "Time Resolved Two Dimensional X-Ray Densitometry of a Two Phase Flow Downstream of a Ventilated Cavity", *Experiments in Fluids*, **54**, 2013
27. Mäkiharju, S.A., "The Dynamics of Ventilated Partial Cavities over a Wide Range of Reynolds Numbers and Quantitative 2D X-ray Densitometry for Multiphase Flow", *Ph.D Thesis, University of Michigan*, 2012
28. Milne-Thomson, L. M., "Theoretical Hydrodynamics", *Dover Publications*, 2011
29. Pham, T. M., Larrarte, F. & Fruman, D. H., "Investigation of unstable cloud cavitation", *In Proc. Third Intl Symp. on Cavitation, April 1998, Grenoble, France,*

215-22, 1998

30. Prandtl, L., and Tietjens, O., G., “Fundamentals of Hydro- and Aero-mechanics”, *Dover Publications*, 2011
31. Reisman, G. E. & Brennen, C. E., “Observations of shock waves in cloud cavitation”, *J. Fluid Mech.* **355**, 255-283, 1998
32. Shamsboran, H., Coutier-Delgosha, O., Caignaert, G. & Nour, F. A., “Experimental determination of speed of sound in cavitating flow” *Expt in Fluids*. **49**, 1359-1373, 2010
33. Stutz, B & Reboud, J. L., “Experiements on unsteady cavitation”, *Expt in Fluids*. **22**, 191-198, 1997a
34. Stutz, B & Reboud, J. L., “Two-phase flow structure of sheet cavitation”, *Physics of fluids*. **9**, 12, 3678-3686, 1997b
35. Stutz, B & Legoupil, S., “X-ray measurements within unsteady cavitation”, *Expt in Fluids*. **35**, 130-138, 2003
36. Wu, Y.-T. T., “Cavity and Wake Flows”, *Annual Rev. of Fluid Mech*. **4**, 243-284, 1972
37. Wu, Y.-T. T., Whitney, A. K., & Brennen, C., “Cavity Flow Wall Effects and Correction Rules”, *J. of Fluid Mech,* **49**, 2, 223-256, 1971
38. E. A. Arndt, V. H. Arakeri, and H. Higuchi, “Some observations on tip vortex cavitation ”, *J. of Fluid Mech.* **229**, 269–289, 1991
39. R. E. A. Arndt, and B. H. Maines, “Nucleation and Bubble Dynamics in Vortical Flows”, *J. Fluids Eng.*, **122**, 488-493, 2000
40. R. E. A. Arndt, “Cavitation in vortical flow”, *Annual. Rev. Fluid Mech.* **34**, 143–175, 2002

41. G. K. Batchelor, “Axial flow in trailing vortices”, *J. Fluid Mech.* **20**(4), 645-658, 1964

42. N. Chang, H. Ganesh, R. Yakushiji, and S. L. Ceccio, “Tip Vortex Cavitation Suppression by Active Mass Injection”, *J. Fluids Eng.*, **133** (11), 111301, 1-11, 2011

43. N. Chang, J. Choi, R. Yakushuji, and S. L. Ceccio, “Cavitation inception during the interaction of a pair of counter-rotating vortices”, *Physics of Fluids*, **24**, 014017, 1- 15 2012

44. N. Chang, and S. L. Ceccio, “The acoustic emissions of cavitation bubbles in stretched vortices”, *J. Acoustical Society of America*, **130**(5), 3209-3219, 2011

45. J-K. Choi, and G. L. Chahine, “Noise due to extreme bubble deformation near inception of tip vortex cavitation”, *Physics of Fluids.*, **16**, 4, 2411-2418, 2004

46. J. Choi, and S. L. Ceccio, “Dynamics and noise emission of vortex cavitation bubbles”, *J. Fluid Mech.* **575**, 1-26, 2007

47. J. Choi, C-T. Hsiao, G. L. Chahine, and Ceccio, S. L., “Growth, oscillation, and collapse of vortex cavitation bubbles,” *J. Fluid Mech.*, **624**, 255-279, 2009

48. D. L. Darmofal, R. Khan, E. M. Greitzer, and C. S. Tan, “Vortex core behavior in confined and unconfined geometries”, *J. Fluid Mech.* **449**, 61-84, 2001

49. J. M. Delery, “ Physics of Vortical flows”, *J. of Aircraft*, **29**, 5, 856-876, 1992

50. J. M. Delery, “ Aspects of vortex breakdown”, *Progress in Aerospace Science*, **30**(1), 1-59, 1994

51. P. B. Earnshaw, and J. A. Lawford, “Low-speed wind-tunnel experiments on a series of sharp-edged delta wings**”,** *ARC R & M*. **3424,** 1964

52. G. E. Erickson, “Flow studies of slender wing vortices**”,** *AIAA Paper No*. **80** 1423,

1980

53. T. B. Francis, and J. Katz, "Observation on the development of a tip vortex on a rectangular foil", *J. Fluids Eng.*, **110**, 208-215, 1988

54. D. Fruman, C. Dugue, A. Pauchet, P. Cerruti, and L. Briancon-Marjolet, "Tip vortex roll-up and cavitation", *Proceedings of the 19th International Symposium on Hydrodynamics Seoul, Korea,* 633-654, 1992

55. D. Fruman, A. Pauchet, P. Cerruti, T. Pichon, and P. Dupont, "Effect of hydrofoil planform on Tip vortex roll-up and cavitation", *J. Fluids Eng.*, **117**, 162-169, 1995

56. S. I. Green, "Correlating single phase flow measurements with observations of trailing vortex cavitation", *J. Fluids Eng.*, **113**, 125-129, 1991

57. S. I. Green, and A. J. Accosta, "Unsteady flow in trailing vortices", *J. Fluid Mech.* **227**, 107-134, 1991

58. S. I. Green, "Fluid Vortices", *Kluwer Academic Publishers,* 1995

59. J. J. Keller, W. Egli, and J. Exley,"Force and loss-free transitions between flow states", Z. Angew. Math. Phys. **36**, 854-889, 1992

60. P. Molton, "Etude expérimentale de l'éclatement tourbillonnaire sur aile delta en écoulement incompressible**",** *Caractérisation du champ externe., ONERA Rapport Technique* **53/1147,** 1992

61. B. W. McComick, "On vortex produced by a vortex trailing from a lifting surface", *Journal of Basic Engineering,* **Sept**, 369-379, 1954

62. J. F. McKernan, and R. C. Nelson, "An investigation of the breakdown of the leading edge vortices on a delta wing at high angles of attack", *AIAA Paper* **83-2114,** 1983

63. A. M. Mitchell, D. Barberis, P. Molton, and J. Delery, "Oscillation of vortex

breakdown location and blowing control of time averaged location", *AIAA Journal*, **38**, 5, 793-803, 2000

64. R. C. Nelson, and A. Pelletier, "The unsteady aerodynamics of slender wings and aircraft undergoing large amplitude maneuvers", *Progress in Aerospace Sciences* **39**, 185–248, 2003
65. F. M. Payne, T.T. Ng, R. C. Nelson, and L. B. Schiff, "Visualization and flow surveys of the leading edge vortex structure on delta wing planforms", *AIAA Paper* **86-0330,** 1986
66. F. M. Payne, T.T. Ng, R. C. Nelson, and L. B. Schiff, "Visualization and Wake Surveys of Vortical Flow over a Delta Wing", *AIAA J.*, **26**(2), 137-143, 1988
67. Z. Rusak, and D. Lamb, "Prediction of Vortex Breakdown in Leading-Edge Vortices Above Slender Delta Wings", *J. of Aircraft*, **36**(4), 659-667, 1999
68. X. Shen, S. L. Ceccio, and M. Perlin, "Influence of bubble size on micro-bubble drag reduction", *Experiments in Fluids*, **41**(3), 415-424, 2006
69. K. D. Visser, and R. C. Nelson, "Measurements of circulation and vorticity in the leading-edge vortex of a delta wing", *AIAA Journal*, **31**(1), 104-111, 1993
70. S. Wang, and Z. Rusak, "The dynamics of a swirling flow in a pipe and transition to axisymmetric vortex breakdown", *J. Fluid Mechanics*, **340**, 177-223, 1997